

**SHEAR ALFVÉN CONTINUA AND DISCRETE MODES IN THE PRESENCE OF A
MAGNETIC ISLAND**

by

Carson Raymond Cook

A dissertation submitted in partial fulfillment of
the requirements for the degree of

Doctor of Philosophy
(Physics)

at the

UNIVERSITY OF WISCONSIN–MADISON

2015

Date of final oral examination: 6/26/2015

The dissertation is approved by the following members of the Final Oral Committee:

Chris Hegna, Professor, Engineering Physics

David Anderson, Professor, Electrical and Computer Engineering

Carl Sovinec, Professor, Engineering Physics

John Sarff, Professor, Physics

Deniz Yavuz, Professor, Physics

© Copyright by Carson Raymond Cook 2015

All Rights Reserved

ABSTRACT

Shear Alfvén instabilities are of considerable interest to plasma confinement and will become even more important in ITER and future devices containing strong energetic particle drive. In this dissertation, we investigate the effects of a magnetic island on the shear Alfvén continuum both analytically and numerically. Using an island coordinate system and a WKB approximation of the linearized ideal MHD equations, a shear Alfvén dispersion relation for the continuum is found globally in the presence of an island; the first time this has been obtained analytically. The island is shown to cause an upshift in the continuum accumulation point frequency. The minimum of the frequency spectrum is shifted from the rational surface to the island separatrix. This analytic result confirms previous numerical work. The new theory also identifies additional parity constraints for the continuum not captured by the previous numerical work in the field. The structure of the continuum modes is also presented.

The theory is used to explain some previously uncategorized Alfvénic activity observed on the Madison Symmetric Torus (MST) reversed-field pinch during neutral beam injection. A sizable $n = 5$ island exists in the plasma core that has not been included in past simulations of the Alfvén spectrum in MST. The theoretical Alfvén continua in the core of the island provide a gap in which the observed $n = 4$ Alfvénic bursts reside, suggesting that these modes may arise from a coupling due to the island. A novel code for computing Alfvén eigenmodes called SIESTAAlfvén is described. SIESTAAlfvén utilizes 3D MHD equilibria with an island obtained using the SIESTA code. The Alfvén modes are computed by solving the generalized eigenvalue problem obtained from the Hessian matrix of the potential energy along with the inertia matrix of the SIESTA equilibrium. Numerical simulations using the STELLGAP/AE3D codes, as well as SIESTAAlfvén, are used to identify the Alfvén bursts on MST as the first observation of an Island-induced Alfvén

Eigenmode (IAE). The IAE arises from a helical coupling of mode numbers similar to the helicity-induced Alfvén eigenmode, but occurs in the core of an island. Additional $n = -1$ activity on MST is shown to be consistent with a second type of island-induced mode residing below the lowest continuum branch, named here the Island-induced Global Alfvén Eigenmode (IGAE). The continuum theory also helps to explain the Beta-induced Alfvén Eigenmode (BAE) frequencies observed during tearing mode activity on tokamaks including EAST and FTU.

ACKNOWLEDGMENTS

First of all, I would like to sincerely thank everyone at the University of Wisconsin who has made it possible for me to get to this point. Chris Hegna and David Anderson both served as great research advisors throughout graduate school, challenging me and supporting me every step of the way. David Anderson sparked my interest in plasma physics back as an undergrad and is one of the main reasons I chose this field of study. During an undergrad electromagnetics course, David took me on a tour of HSX, and I thought it was amazing. David opened a lot of doors for me both at UW and through collaborations at Oak Ridge National Lab. Chris graciously picked up the advisor role when my research branched onto a more theoretical and computational path, deviating from the core HSX mission. Time spent bouncing ideas off of Chris and getting intimidated with his mathematical knowledge certainly pushed me to improve and hone my analytical skills. Chris gave me a great deal of freedom to work at my own pace through calculations, and I am very thankful for all of the help he provided along the way to reaching those “Aha!” moments.

Carl Sovinec has been very kind and helpful to me throughout my time at UW both as an undergrad and grad student. As a junior undergraduate, I was admittedly not quite ready for Physics 525 when I took it. I remember trying to correct Carl one day when he had written a vector next to another vector on the board; I had never seen a tensor product and my mathematical world was temporarily rocked. Carl was always patient and put up with my endless strings of questions, particularly as an undergrad and in MHD as a grad student. Carl also served as an academic advisor during my transition to Physics in grad school.

Steve Hirshman and Don Spong of Oak Ridge National Lab both served as remote advisors of sorts, and were always available to help me with computational work. Their willingness to teach me their codes is truly appreciated. Steve, Don, and Raul Sanchez were all invaluable in helping

me get through my research. During trips to Oak Ridge, John Canik, Jeremy Lore, and David Green all provided a great deal of fun and friendship to me, making me feel right at home.

The HSX group has provided a lot of lasting friendships. Having so many fun people in an office helps when working on a dissertation for endless hours. The crew at HSX always included me in all their activities, despite doing my own research thing. Shenanigans and time spent with Enrico Chlechowicz, Bob Wilcox, Gavin Weir, and Jason Smoniewski will especially be cherished. In addition, it was always nice to hang out with John Garrett, Danny Crow, and Tom Perry and gain back some sanity (or lose some) when needed.

The entire MST group has been fantastic to work with. Everyone at MST has been more than happy to give me endless amounts of data, plots, and anything else that I ask for. Jay Anderson, John Boguski, and Karsten McCollam have been particularly helpful with grounding my theory in the experimental world. They also have had to deal with my often stupid questions about MST, and for their patience I am thankful. Jon Koliner was selfless in giving his time, data, and insights in helping me get my theory off the ground. His willingness to meet in the evenings after his full-time job is greatly appreciated.

I have been extremely lucky to hold a DOE Office of Science fellowship during some of my time in graduate school. For this I am indebted to the Department of Energy and in turn, the American taxpayers. This fellowship allowed for a great deal of research textbooks, conference travel, and networking, and I am grateful for the opportunity.

Finally and most importantly, I want to thank my family. My parents Joe and Nola are the best parents anyone could ask for. They have always driven and challenged me without putting too much pressure on me, and they are always there for me no matter what. My sister Lona is the same and would do anything for me. My dog Penny has stayed up until 3 am with me on many late nights, watching me while I write or run simulations. Finally, my beautiful fiancée and soon-to-be-wife Nikki has put up with a lot as I write this thesis and work endless hours without giving her much attention. Throughout it all she has remained loving, supportive, and understanding. It's probably time I take her on a nice date...

TABLE OF CONTENTS

	Page
ABSTRACT	i
LIST OF TABLES	viii
LIST OF FIGURES	ix
1 Introduction and background	1
1.1 Outline	2
1.2 Background on shear Alfvén waves	4
1.2.1 Continuum modes	8
1.2.2 Coupling of continua to form gaps	10
1.2.3 Discrete Alfvén eigenmodes (AEs)	15
2 Analytical theory of the shear Alfvén continuum in the presence of a magnetic island	17
2.1 Island coordinate system	17
2.2 Ideal MHD in the presence of an island	20
2.3 WKB analysis of continuum equation	24
2.4 Alfvén continuum and eigenmode structure	27
2.5 Exact continuum solution at the O-point	30
2.6 Summary	35
3 Comparison of theoretical continua to experimental observations	36
3.1 Background on the Madison Symmetric Torus (MST)	36
3.1.1 Geometry and equilibrium features	37
3.1.2 Neutral beam injection	37
3.1.3 Alfvénic activity during NBI	39
3.2 Investigation of $n = 4$ Alfvén bursting modes on MST	42
3.3 Effects of $n_0 = 5$ island on MST continuum	44
3.4 Island-modified BAE modes in MST vs. tokamaks	52
3.4.1 BAE frequency upshift on MST	54
3.4.2 BAEs on the EAST tokamak	54
3.4.3 BAEs on the FTU tokamak	57
3.5 Summary	57

	Page
4 Numerical investigation of Alfvén eigenmodes on MST	60
4.1 Modeling MST with an island as a SHAx state	60
4.2 The Variational Moments Equilibrium Code (VMEC)	61
4.3 The STELLGAP continuum code	65
4.3.1 Model equations	65
4.3.2 Computing the MST Alfvén continuum	66
4.4 The AE3D code for calculating Alfvén modes	71
4.4.1 Model equations	71
4.4.2 Computing Alfvén eigenmodes in MST	73
4.5 Summary	78
5 Computing MHD modes with the SIESTA_{Alfvén} code	79
5.1 The Scalable Iterative Equilibrium Solver for Toroidal Applications (SIESTA)	80
5.1.1 MHD equilibrium energy principle	80
5.1.2 Fourier representation and boundary conditions	82
5.1.3 Preconditioning with the Hessian	83
5.1.4 Opening magnetic islands	86
5.2 Including inertia with the SIESTA _{Alfvén} code	90
5.2.1 MHD eigenmode equations with inertia	91
5.2.2 Constructing the inertia matrix	92
5.2.3 Solving for the MHD eigenmodes	95
5.2.4 Constructing the shear Alfvén displacement	96
5.3 Benchmarking SIESTA _{Alfvén} against AE3D for a TAE case	99
5.4 Summary	101
6 Identification of the Island-induced Alfvén Eigenmode (IAE)	102
6.1 MST SIESTA equilibrium	103
6.2 The Island-induced Alfvén Eigenmode (IAE)	103
6.2.1 Discovery of the IAE with SIESTA _{Alfvén}	106
6.2.2 Mode structure of the IAE	107
6.3 Unexplained $n = -1$ activity on MST	110
6.3.1 $n = -1$ mode as a Fourier component of the IAE	114
6.3.2 $n = -1$ mode as an island-upshifted BAE	114
6.3.3 $n = -1$ mode as an Island-induced Global Alfvén Eigenmode (IGAE)	115
6.4 Summary	118

Appendix

Page

7 Conclusions and future work 121

APPENDICES

Appendix A: C, D, E, and F matrix operators 128

Appendix B: Island rotational transform inside separatrix 129

Appendix C: Island coordinates 131

Appendix D: Translation to Biancalani's notation 132

Appendix E: Boozer-Xform modifications for RFPs 134

BIBLIOGRAPHY 138

LIST OF TABLES

Table	Page
3.1 MST parameters	37
3.2 A comparison of the continuum upshifts for MST and EAST	55
5.1 Scan of helical perturbation size in SIESTA	90
5.2 Comparison of STELLGAP, AE3D, and SIESTAAlfvén	98

LIST OF FIGURES

Figure	Page
1.1 Shear Alfvén wave diagram	7
1.2 Coupling of poloidal harmonics to form TAE gap	14
1.3 $m, m + 1$ coupling for Toroidicity-induced Alfvén Eigenmode (TAE)	15
2.1 Magnetic island coordinate system	19
2.2 Island rotational transform	21
2.3 Shear Alfvén continuum frequencies in the presence of an island (global)	29
2.4 Shear Alfvén continuum frequencies near the separatrix	29
2.5 Continuum mode structure outside the island	31
2.6 Continuum mode structure inside the island	32
3.1 Canonical non-reversed MST safety factor profile and magnetic field	38
3.2 MST neutral beam injector (NBI) view schematic	40
3.3 Fast ion density distribution in MST	41
3.4 MST burst frequency scaling with Alfvén speed	43
3.5 MST q -profile and Alfvén continuum from VMEC/STELLGAP	45
3.6 MST STELLGAP simulation including slow-sound approximation	46
3.7 Continuum in core of island from theory with MST AE burst data	51
3.8 Continuum in core of island from theory with and without BAE frequency upshift	51

Figure	Page
3.9 Continuum in core of island from theory with three different values of island width . . .	52
3.10 Schematic of island-induced BAE frequency upshift	53
3.11 Experimental q -profile and BAE frequencies for EAST tokamak	56
3.12 Observed BAE frequencies vs. tearing mode amplitude on the FTU tokamak	58
4.1 Flux surfaces of VMEC equilibrium for MST SHAx state	64
4.2 Alfvén continuum frequencies in MST from STELLGAP with dominant n	67
4.3 Alfvén continuum frequencies in MST from STELLGAP with dominant m	68
4.4 200, 250, and 300 kA MST Alfvén continuum frequencies from STELLGAP	70
4.5 AE3D representation of a continuum mode	74
4.6 Helicity-induced Alfvén Eigenmode in MST computed using AE3D	75
4.7 Alfvén eigenmode from AE3D for 200 kA MST configuration	77
4.8 Theory and STELLGAP continuum and AE3D mode frequencies for MST	77
5.1 SIESTA iterative scheme	89
5.2 Toroidicity-induced Alfvén Eigenmode test case computed with AE3D and SIESTA	100
6.1 SIESTA pressure contours for MST in a poloidal plane displaying the $m_0 = 1$ island .	104
6.2 MST Poincaré puncture plot from SIESTA for a constant- θ plane displaying the $n_0 =$ 5 island	105
6.3 MST ion density profile used in SIESTA	106
6.4 Poloidal component of Island-induced Alfvén Eigenmode (IAE) in MST computed using SIESTA	108
6.5 Binormal surface component of Island-induced Alfvén Eigenmode (IAE) in MST computed using SIESTA	109
6.6 $n, n + \delta n$ coupling for Island-induced Alfvén Eigenmode (IAE)	111

Appendix Figure	Page
6.7 Temporal evolution of $n = 5$, $n = 4$, and $n = -1$ modes in MST	113
6.8 Spatial and temporal activity for $n = 5$, $n = -1$, and $n = 4$ density fluctuation activity on MST	113
6.9 Island-induced global Alfvén eigenmode (IGAE) on MST computed with AE3D . . .	117
6.10 Schematic of island-modified Alfvén eigenmodes in continuum gaps	120
E.1 Boozer coordinates Jacobian in toroidal flux	135
E.2 Boozer coordinates Jacobian in poloidal flux	136
E.3 STELLGAP results with a reversal surface before modifications	136
E.4 STELLGAP results with a reversal surface after modifications	137

Chapter 1

Introduction and background

The spectrum of shear Alfvén waves in a magnetically-confined plasma is a crucial topic for understanding the stability properties of the configuration. Frequency gaps in the continuous spectrum (continuum) can lead to Alfvén modes that can couple to and be destabilized by energetic particles such as those driven by neutral beam injection (NBI) or the copious fast α -particles present in a fusion reaction. Alfvén instabilities are a general feature of plasma equilibria that can occur in tokamaks, stellarators, and RFPs.

The shear Alfvén spectrum will become increasingly important as the fusion community pushes ahead towards ITER and eventually DEMO. In particular, the presence of continuum gaps must be understood, as they can point to locations in the plasma where discrete Alfvén eigenmodes (AEs) could exist. These modes cannot couple to the Alfvén waves of the continuous spectrum and thus do not experience continuum damping. In high temperature fusion-relevant plasmas, these modes could potentially be driven unstable through a coupling to energetic α -particles. The speed of α -particles in ITER is predicted to be approximately $v_A < v_\alpha < 2v_A$, where v_A is the Alfvén velocity in ITER [1].

The most commonly studied AEs in toroidal geometry include the Toroidicity-induced Alfvén Eigenmode (TAE) and the Beta-induced Alfvén Eigenmode (BAE). These modes lie in gaps that arise from a coupling of poloidal mode numbers and due to finite shear Alfvén wave compressibility via geodesic curvature coupling, respectively [2, 3].

As motivation for this thesis research, MST recently observed a mode exhibiting Alfvénic scaling in 300 kA, non-reversed plasmas with NBI [4]. Theoretical simulations using the STELLGAP code predict a TAE gap frequency much higher than the observed mode frequency from experiment [5]. Conversely, the BAE gap frequency computed is lower than the experimental frequency seen on MST. A known limitation of the STELLGAP model is the assumption of closed, nested flux surfaces. A sizable $m = 1, n = 5$ island exists in the core of MST for these operating conditions which is not taken into account in these computations. More recently, a BAE mode has been studied on the EAST tokamak. This mode is only present once an island width threshold has been reached, and appears to increase in frequency as the island evolves to a larger size [6]. Similar phenomena were originally observed on FTU [7, 8] and TEXTOR [9]. With these experimental findings as motivation, it is natural to investigate whether an island can modify the Alfvén spectrum.

The effects of an island on the shear Alfvén continuum have been studied in some detail by Biancalani et al. [10, 11, 12]. In Biancalani’s work, a shooting method code was used to compute the spectrum. Biancalani showed that an island induces an upshift in the spectrum’s minimum continuum accumulation point frequency. In the absence of an island, the spectrum minimum lies at the rational surface. In an equilibrium with an island, the location of the minimum shifts to the separatrix and the minimum frequency increases. In the following thesis, both analytic theory and novel numerical techniques are employed to investigate these findings and explain observations on MST and EAST during tearing mode activity.

1.1 Outline

This dissertation is laid out as follows: In this chapter, some background on shear Alfvén waves is presented, the distinction between continuum modes and discrete modes is made, and the coupling mechanism of the continua to form gaps where the discrete modes reside is discussed. The most commonly studied mode, the toroidicity-induced Alfvén eigenmode (TAE) is used as an example to illustrate the important concepts.

In Chapter 2, the equations for the shear Alfvén continuum are solved in the presence of a magnetic island using WKB theory. An island coordinate system is introduced, which is needed to solve the Alfvén spectrum when an island is present. Linearized ideal MHD is the model employed to describe the equilibrium with an island. The frequency continuum and eigenmode solutions are obtained globally, and the continuum is obtained exactly at the O-point (or core) of the island. The frequency upshift of the continuum accumulation point is demonstrated analytically for the first time, and it matches previous numerical results by Biancalani [10].

Chapter 3 explores the experimental observations of $n = 4$ Alfvénic bursting activity on MST. The bursts occur during neutral beam injection (NBI) on non-reversed plasmas containing a sizable $n_0 = 5$ magnetic island. The observed frequencies of the modes are compared favorably to the continuum frequencies from theory derived in Chapter 2. The $n = 4$ observations are shown to be consistent with an Alfvén gap mode living in the island-induced gap present in the core of the island.

Also included in Chapter 3 is a discussion on the modification of the BAE (beta-induced Alfvén eigenmode) continuum gap frequency for MST and the EAST and FTU tokamaks. The island upshift correction of the minimum continuum frequency is shown to be quite small in MST (7%), but considerable for tokamaks (25% for EAST). The island-induced BAE upshift from the continuum theory helps explain the observed frequencies on EAST.

In Chapter 4, MST is modeled as a Single Helical Axis (SHAx) state with the VMEC equilibrium code. Using this equilibrium, the STELLGAP code is used to solve for the Alfvén continuum and the AE3D code is used to solve for the discrete Alfvén eigenmodes (AEs). Though this configuration does not contain an island, the helical core serves as an approximation for the island without the separatrix. In the helical core, the continua from STELLGAP agree quite well with the results from the island continuum theory. A helicity-induced Alfvén eigenmode (HAE) is found with the AE3D code in the helical core. The mode is found at 149 kHz, in agreement with the 140 – 160 kHz observed in experiment.

VMEC and AE3D cannot properly handle magnetic topologies with an island, so another approach is needed for computations with an equilibrium containing two magnetic axes. To accomplish this task, the SIESTA equilibrium code and the new SIESTAAlfvén eigensolver are used and are discussed in Chapter 5. SIESTA begins with a VMEC equilibrium and includes non-ideal magnetic perturbations and finite resistivity to obtain an equilibrium containing islands if unstable to the tearing mode. A newly written code called SIESTAAlfvén is introduced; the code acts as a post-processing step once a SIESTA equilibrium is obtained. An inertia matrix is computed (which is not present in SIESTA) and a generalized eigenvalue problem is solved to obtain the MHD modes of the system, including the shear Alfvén modes. The SIESTAAlfvén code is benchmarked against the AE3D code for a configuration containing an $m = 1/m = 2$ -coupled TAE.

Chapter 6 presents the first identification of the Island-induced Alfvén Eigenmode (IAE), obtained using the SIESTAAlfvén code. The IAE is discovered in an MST SIESTA equilibrium containing a large island. The $n = 4/n = -1$ -coupled IAE mode is consistent with the helical $\delta n = 5$ coupling expected for the $n_0 = 5$ island. It is localized inside the island and is found at 145 kHz, consistent with the 140 – 160 kHz range identified experimentally on MST.

Additionally, Chapter 6 explores possible explanations for some $n = -1$ activity observed on MST, which is generally seen preceding the $n = 4$ Alfvén bursts. The case is made that the $n = -1$ bursts may be a second type of island-coupled mode, called here the Island-induced Global Alfvén Eigenmode (IGAE). This extremum mode lives below the lowest branch of the Alfvén continuum in the core of the island and is similar to an RSAE (reversed-shear Alfvén eigenmode) or a GAE (global Alfvén eigenmode).

Finally, Chapter 7 presents conclusions from this thesis as well as multiple future research directions that can build on this work. Several appendices are included at the end of the dissertation. Now on to some background on Alfvén waves.

1.2 Background on shear Alfvén waves

Before analyzing the shear Alfvén spectrum in the presence of a magnetic island, some preliminaries on Alfvén waves must first be addressed. In this section, we begin by discussing the

shear Alfvén wave (SAW), an ideal MHD wave. Next, we describe the continuum wave solutions and the formation of gaps within the continua in Secs. 1.2.1 and 1.2.2, respectively. Finally, a discussion of discrete Alfvén modes is presented in Sec. 1.2.3.

The shear Alfvén wave is a transverse, low-frequency electromagnetic wave [13]. These waves propagate along the magnetic field lines at a characteristic velocity, v_A [14]. In order to study shear Alfvén waves, we will begin with the ideal MHD equations in the low-beta limit, $p \rightarrow 0$, following *Tokamaks* by Wesson [15]. Consider a slab geometry with a uniform magnetic field in the \hat{x} -direction. This equilibrium satisfies

$$\mathbf{B} = B\hat{x}, \quad (1.1)$$

$$\mathbf{J} = 0. \quad (1.2)$$

Next the ideal MHD equations are linearized, giving the following perturbed equations where pressure and kinetic effects are not important (natural units $\mu_0, \epsilon_0 = 1$ are used here and throughout this thesis). The equations are the momentum equation, Ampère's law, Faraday's law, and the ideal MHD Ohm's law:

$$\rho \frac{\partial \mathbf{v}}{\partial t} = \delta \mathbf{J} \times \mathbf{B}, \quad (1.3)$$

$$\delta \mathbf{J} = \nabla \times \delta \mathbf{B}, \quad (1.4)$$

$$\frac{\partial \delta \mathbf{B}}{\partial t} = -\nabla \times \delta \mathbf{E}, \quad (1.5)$$

$$\delta \mathbf{E} = -\mathbf{v} \times \mathbf{B}. \quad (1.6)$$

In this configuration, the shear Alfvén wave displacement is in the transverse \hat{z} -direction, $\mathbf{v} = v_z \hat{z}$. Using this along with the perturbed quantities varying as $\mathbf{v}, \delta \mathbf{E}, \delta \mathbf{B}, \delta \mathbf{J} \sim \exp[i(k_x x + k_y y - \omega t)]$,

the linearized equations can be written as

$$\delta E_y = -v_z B, \quad (1.7)$$

$$\delta B_z = \frac{k_x}{\omega} \delta E_y, \quad (1.8)$$

$$\delta J_x = ik_y \delta B_z, \quad (1.9)$$

$$\delta J_y = -ik_x \delta B_z, \quad (1.10)$$

$$v_z = -\frac{i}{\omega \rho} \delta J_y B. \quad (1.11)$$

Combining these equations one obtains the shear Alfvén dispersion relation,

$$\omega = k_x v_A, \quad (1.12)$$

$$v_A = \frac{B}{\sqrt{\rho}}, \quad (1.13)$$

with v_A the Alfvén speed. In this derivation, the wave-vector had an arbitrary orientation in the x-y plane, $\mathbf{k} = k_x \hat{x} + k_y \hat{y}$. However, the dispersion relation only includes the k_x -component. Since the magnetic field is in the \hat{x} -direction, $k_x = k_{\parallel}$ and the dispersion relation is often written as $\omega = k_{\parallel} v_A$. Regardless of the direction of the shear Alfvén wave propagation, the wave travels with velocity $\omega/k_{\parallel} = v_A$ along the magnetic field direction.

The shear Alfvén wave propagating along the magnetic field lines is often described as a wave traveling along a vibrating, plucked guitar string. The magnetic field line bending $\mathbf{B} \cdot \nabla \mathbf{B}$ provides the tension, and the ion mass provides the inertia. The wave is both incompressible and transverse, with the fluid displacement perpendicular to the plane defined by the \mathbf{B} field and the wave-vector. The structure of the shear Alfvén wave is presented in Fig. 1.1.

Compressional Alfvén waves, or magnetosonic waves, will not be discussed much in this thesis. These waves involve a coupling between Alfvén waves and sound waves through plasma pressure. In these waves, the plasma displacement is no longer perpendicular to both \mathbf{k} and \mathbf{B} , and instead contains velocity oscillations with components parallel to \mathbf{k} . These waves are compressible $\nabla \cdot \boldsymbol{\xi} \neq 0$, since $\nabla \sim i\mathbf{k}$ and $\mathbf{k} \cdot \boldsymbol{\xi} \neq 0$. In this thesis, the slow-sound approximation is used several times to remove wave compressibility (and thus exclude magnetosonic waves), but it includes the

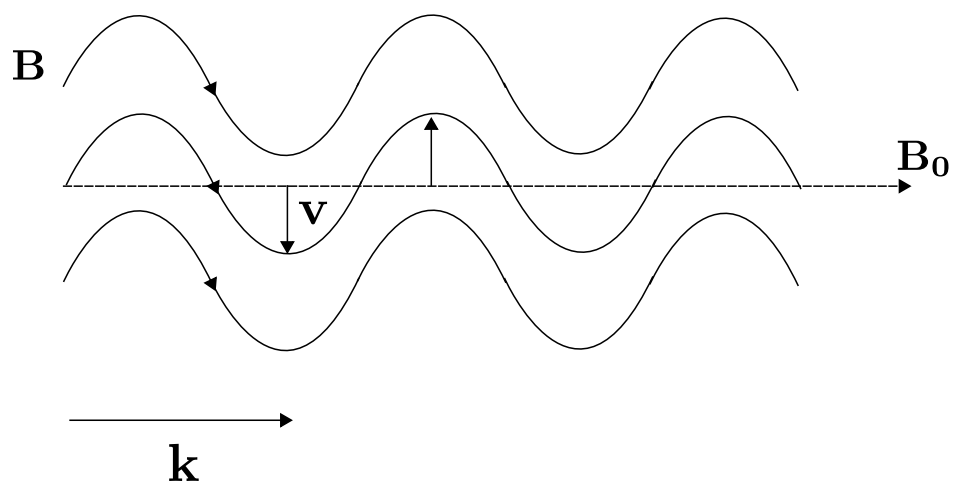


Figure 1.1 A propagating shear Alfvén wave with transverse plasma velocity v creating field line bending. The wavevector k is parallel to the background field in this case.

compressional fluid response to a propagating shear Alfvén wave. This approximation is described in Sec. 1.2.1.

1.2.1 Continuum modes

In a toroidal magnetic geometry with major radius R , there is a double-periodicity constraint on the shear Alfvén waves. The wave mode structure must accommodate m wavelengths in the poloidal direction and n wavelengths in the toroidal direction. Due to the magnetic field structure, the periodicity constraints require $k_{\parallel} = (n - m/q)/R$, where q is the safety factor. The safety factor is defined on a field line as $q = \Delta\phi/2\pi$, where $\Delta\phi$ is the change in toroidal angle required for the field line to return to the same poloidal location. Since the safety factor is a function of the radius (or poloidal flux), the average parallel wavevector $\langle k_{\parallel} \rangle = (n - m/q)/\langle R \rangle$ is also a function of radius. Thus the average frequency from the dispersion relation $\langle \omega \rangle = \langle k_{\parallel} \rangle \langle v_A \rangle$ varies with radius. The sheared magnetic field causes the average frequency $\langle \omega(\psi) \rangle$ to vary with radius or poloidal flux ψ for a general toroidal device.

Since the magnetic field lines lie on flux surfaces, the shear Alfvén waves propagating along the field lines are surface-localized. The waves propagating on a single flux surface are known as Alfvén continuum modes. The modes have a non-square-integrable radial structure; they are characterized by a delta function at the resonant surface. The shear Alfvén displacement has the following structure:

$$\xi_s = \delta(\psi - \psi_0) \cos(m\theta - n\zeta), \quad (1.14)$$

where ψ_0 is the surface on which the continuum mode lives. The poloidal and toroidal variation in the continuum wave is given by the dominant mode numbers m and n that identify the continuum frequency branch.

The nature of the continuum modes can easily be shown mathematically for an axisymmetric toroidal configuration [16]. For a toroidal plasma, the equilibrium values obey force balance,

Ampère's law, and the divergence constraint:

$$\mathbf{J} \times \mathbf{B} = \nabla p, \quad (1.15)$$

$$\nabla \times \mathbf{B} = \mathbf{J}, \quad (1.16)$$

$$\nabla \cdot \mathbf{B} = 0. \quad (1.17)$$

The linearized ideal MHD equations for this equilibrium are the momentum equation, the equation of state, and the combined Faraday's law/Ohm's law:

$$-\rho\omega^2 \boldsymbol{\xi} = (\nabla \times \mathbf{B}) \times \delta \mathbf{B} + (\nabla \times \delta \mathbf{B}) \times \mathbf{B} - \nabla \delta p, \quad (1.18)$$

$$0 = \delta p + \boldsymbol{\xi} \cdot \nabla p + \gamma p \nabla \cdot \boldsymbol{\xi}, \quad (1.19)$$

$$\delta \mathbf{B} = \nabla \times (\boldsymbol{\xi} \times \mathbf{B}). \quad (1.20)$$

Substituting Eq. (1.20) into Eq. (1.18) results in a system of four equations in four unknowns, $\boldsymbol{\xi}$ and δp .

This system of the modified Eq. (1.18) and Eq. (1.19) can be rewritten using a straight field line magnetic field representation and coordinate system. The magnetic field can be written as

$$\mathbf{B} = \nabla \zeta \times \nabla \psi + q \nabla \psi \times \nabla \theta, \quad (1.21)$$

where ψ is the poloidal flux, q is the safety factor, and θ and ζ are the generalized poloidal and toroidal angles, respectively. In terms of these flux coordinates, the system in Eqs. (1.18) and (1.19) can be rewritten using the variables $\nabla \cdot \boldsymbol{\xi}$, $\xi^\psi = \boldsymbol{\xi} \cdot \nabla \psi$, $\xi_{surf} = \boldsymbol{\xi} \cdot (\mathbf{B} \times \nabla \psi) / |\nabla \psi|^2$, and $\delta P = \delta p + \delta \mathbf{B} \cdot \mathbf{B}$. With these variables, the linearized MHD equations become

$$\nabla \psi \cdot \nabla \begin{bmatrix} \delta P \\ \xi^\psi \end{bmatrix} = \mathbf{C} \begin{bmatrix} \delta P \\ \xi^\psi \end{bmatrix} + \mathbf{D} \begin{bmatrix} \xi_{surf} \\ \nabla \cdot \boldsymbol{\xi} \end{bmatrix}, \quad (1.22)$$

$$\mathbf{E} \begin{bmatrix} \xi_{surf} \\ \nabla \cdot \boldsymbol{\xi} \end{bmatrix} = \mathbf{F} \begin{bmatrix} \delta P \\ \xi^\psi \end{bmatrix}, \quad (1.23)$$

where \mathbf{C} , \mathbf{D} , \mathbf{E} , and \mathbf{F} are 2×2 matrix operators containing surface derivatives $\mathbf{B} \cdot \nabla$ and $(\mathbf{B} \times \nabla \psi) \cdot \nabla$. Details on these matrices can be found in Appendix A. This system is solved by first

computing ξ_{surf} and $\nabla \cdot \xi$ in terms of δP and ξ^ψ from Eq. (1.23) by inverting the \mathbf{E} operator. These expressions are substituted into Eq. (1.22) which is solved for δP and ξ^ψ for solutions that are periodic in θ and ζ .

This solution method does not work if the \mathbf{E} matrix is not invertible for a given surface ψ_0 and frequency $\omega(\psi_0)$. In this case, Eq. (1.22) has a radial singularity. If a non-square-integrable solution with a radial singularity at ψ_0 exists, it will be a non-trivial periodic solution to the following:

$$\mathbf{E} \begin{bmatrix} \xi_{surf} \\ \nabla \cdot \xi \end{bmatrix} = 0. \quad (1.24)$$

The eigenvalue ω^2 which is buried in \mathbf{E} is the continuum frequency for the surface ψ_0 . If this procedure is followed for the eigenfrequencies for each flux surface, the corresponding spectrum $\omega^2(\psi)$ of continuous frequencies is the Alfvén continuum. Note that Eq. (1.24) involves a coupling between the shear Alfvén waves and acoustic waves through geodesic curvature and pressure. In the slow sound approximation $\gamma p / \rho \omega^2 R_0^2 \ll 1$, the equations decouple and become a single equation for the shear Alfvén displacement ξ_{surf} . This approximation removes compressibility from the Alfvén waves (creating purely shear Alfvén waves), but retains the compressional response of the fluid to the waves.

These continuum modes are generally strongly stable due to the phenomenon known as continuum damping. Continuum damping is the process of dispersion that occurs when a finite wave packet is excited within the plasma. Since a wave packet with radial extent would involve a coupling between different flux surfaces, the Alfvén velocity is different on each of these surfaces (from the shear) and the wave would quickly disperse. This coupling and spreading of energy to neighboring continuum waves makes it difficult for energetic particles to drive a continuum mode unstable.

1.2.2 Coupling of continua to form gaps

Continuum modes with different poloidal and toroidal mode numbers can couple together to form gaps in the continua [17, 18]. These frequency gaps are important because discrete Alfvén eigenmodes (AEs) can reside in these frequency bands without experiencing continuum damping.

These Alfvénic instabilities are the subject of Sec. 1.2.3. A useful resource on the coupling of Alfvén continua as well as discrete modes is Heidbrink’s 2008 PoP review [14], which was used to inform this discussion.

The existence of continuum gaps is a generic wave phenomenon. Bragg reflection in a crystal lattice and the electron band gap in conductors are examples of frequency gaps. Lord Rayleigh showed that any configuration which contains a periodic variation in the index of refraction N will induce a continuum frequency gap [19]. In the lattice of a conductor, the periodic potential modulation caused from the atoms gives a variation in N in the electron wave equation, resulting in the electron band gap.

The periodic variation in the index of refraction in the core of an optical fiber creates a frequency gap through the interaction of counter-propagating waves. The central frequency of the gap is

$$f_0 = \frac{\langle v \rangle}{2\Delta z}, \quad (1.25)$$

with $\langle v \rangle$ the average phase velocity in the fiber and Δz the length of the periodic modulation in N along the fiber. The gap frequency width is proportional to the modulation in N , $\Delta f \sim \Delta N / \langle N \rangle$ where $\Delta N = N_{max} - N_{min}$ and $\langle N \rangle$ is the average refractive index. The gap is created by the destructive interference of counter-propagating waves as they Bragg reflect off the periodic variations in the index of refraction.

Bragg reflection also occurs for Alfvén waves in plasmas. The Toroidicity-induced Alfvén Eigenmode (TAE) gap is arguably the most commonly encountered continuum gap in the fusion literature [20, 16], due to its prevalence in tokamaks, RFPs, and stellarators. An analogy with Bragg reflection in fiber optics is helpful in understanding the mechanism for TAE gap formation in toroidal devices. In a tokamak with magnetic shear, the field strength B varies along the field line. Poloidal currents in the external toroidal field (TF) coils create toroidal magnetic fields through Ampère’s law:

$$\oint \mathbf{B} \cdot d\mathbf{l} = B2\pi R = I_{enc}, \quad (1.26)$$

where R is the major radius. From this, the magnetic field strength is given by $B = I_{enc}/2\pi R$. This makes clear the fact that a torus has a high-field side (inboard) and a low-field side (outboard),

since $B \sim 1/R$. The poloidal direction of symmetry in a cylinder is broken in a torus through the modulation of the magnetic field strength. The “index of refraction” N for Alfvén waves in plasma can be defined as

$$N = \frac{\langle v_A \rangle}{v_A}, \quad (1.27)$$

where $\langle v_A \rangle$ is the average Alfvén speed in the plasma. Recalling from Sec. 1.2 that $v_A = B/\sqrt{\rho}$ allows us to write out the refractive index in terms of the field strength:

$$N = \frac{\sqrt{\rho}\langle v_A \rangle}{B} \sim \sqrt{\rho}R\langle v_A \rangle. \quad (1.28)$$

Assuming a uniform density, the index scales with major radius $N \sim R$. The variation in index of refraction as well as the Alfvén speed along a field line creates a continuum frequency gap analogous to the Bragg gap for fiber optics discussed above. Magnetic field lines sample both the high- and low-field sides of the torus, and counter-propagating waves traveling along the field reflect off the periodic variations in B and interfere to create the gap.

In order to compute the central frequency of the TAE gap analogously to the Bragg frequency in Eq. (1.25), the distance Δz along which the magnetic field varies periodically is needed. The distance along a field line to return to a given poloidal location is $\Delta z = q2\pi R_0$. This is the distance required to complete one full period in the modulation of the B field strength. Substituting this into Eq. (1.25) gives the central TAE gap frequency:

$$f = \frac{\langle v_A \rangle}{q4\pi R_0}. \quad (1.29)$$

To determine the gap width Δf , the equation $\Delta f \sim \Delta N/\langle N \rangle$ will be used. The average index for a field line on a flux surface is proportional to the major radius of the magnetic axis of the device, $\langle N \rangle \sim R_0$. Assuming a circular cross-section, a flux surface at minor radius r will have $N_{max} \sim R_0 + r$ and $N_{min} \sim R_0 - r$. This gives $\Delta N \sim r$, and the continuum gap width is proportional to r :

$$\Delta f \sim \frac{r}{R_0}. \quad (1.30)$$

This can easily be extended to non-circular flux surfaces using the poloidal flux as a radial coordinate, $\langle r \rangle \sim \sqrt{\psi}$. Eq. (1.30) gives the gap width as a function of minor radius, with the widest

TAE gap occurring at the edge $r = a$ where $\Delta f \sim a/R_0 = \epsilon$, the inverse aspect ratio. Physically, this widening of the gap with minor radius comes from the fact that the magnetic field variation on a flux surface increases with increasing r : $\Delta B \sim r$. The widening of the TAE gap with radius is shown in Fig. 1.2. In this plot, the central frequency of the gap $f_0 \sim 1/q$ decreases radially as this configuration has a monotonically increasing q -profile.

The gap frequency and width as a function of radius were derived from counter-propagating waves. The TAE example will be used to show how the shear Alfvén continua can couple together. For two continuum modes with the same toroidal mode number n and poloidal mode numbers differing by 1, the m and $m + 1$ mode numbers couple together. These two oppositely directed modes have equal wavenumbers $|k_{\parallel}|$ at a specific radius, which means their frequencies $\omega = |k_{\parallel}| v_A$ are also equal at that radius. The m continuum mode and the $m+1$ mode have the following parallel wavenumbers, respectively:

$$k_{\parallel} = \frac{1}{R}(n - m/q), \quad (1.31)$$

$$k_{\parallel} = -\frac{1}{R}|n - (m + 1)/q|. \quad (1.32)$$

The location where the wavenumbers match is the surface where $q = (m + 1/2)/n$; at this surface we have the following for both continua:

$$|k_{\parallel}| = \frac{1}{2qR}, \quad (1.33)$$

$$\omega = \frac{v_A}{2qR}. \quad (1.34)$$

This frequency is just the Bragg frequency from Eq. (1.25). When the toroidal coupling is included, these two waves mix and the frequency degeneracy is avoided. This leaves a gap at the location of the frequency crossing (at $q = (m + 1/2)/n$). Within this gap, a discrete Alfvén eigenmode can form, which is the subject of Sec. 1.2.3. Fig. 1.2 displays the continua with and without toroidal couplings. In the absence of continuum coupling from toroidicity, the $m = 4$ and $m = 5$ branches in the first plot have a frequency crossing at the location where $q = 9/8$. When toroidal effects are included, the crossing is replaced with a frequency gap, as illustrated in the second figure.

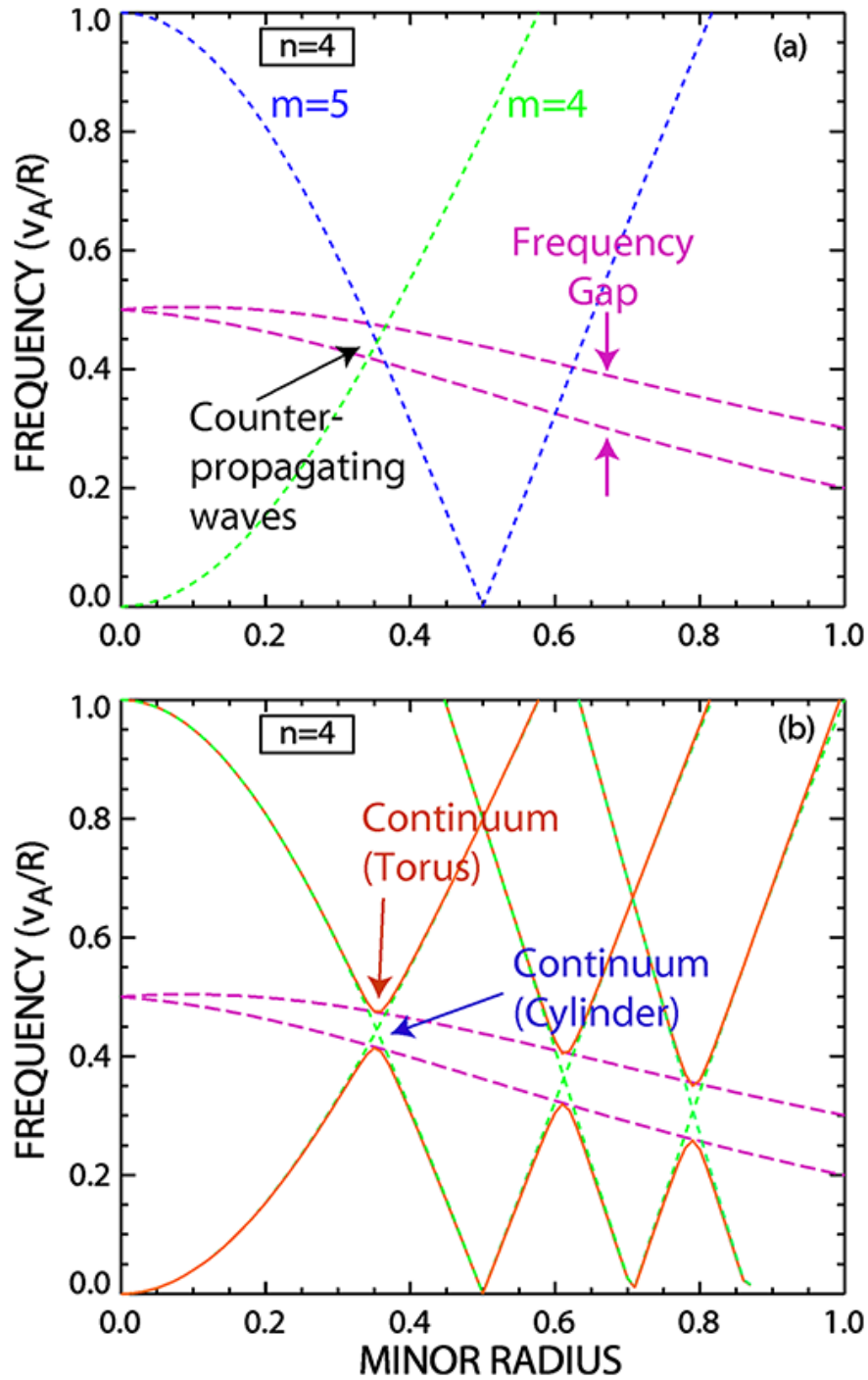


Figure 1.2 A coupling between m and $m + 1$ poloidal modes creates a TAE gap (Toroidicity-induced Alfvén Eigenmode gap). The gap width depends on field strength variation, $\Delta\omega \sim \Delta B/B \sim r/R_0$. a) Counter-propagating waves in a cylindrical geometry. b) In a torus, the m and $m + 1$ modes couple together to form gaps. Figure from Heidbrink, 2008 PoP [14].

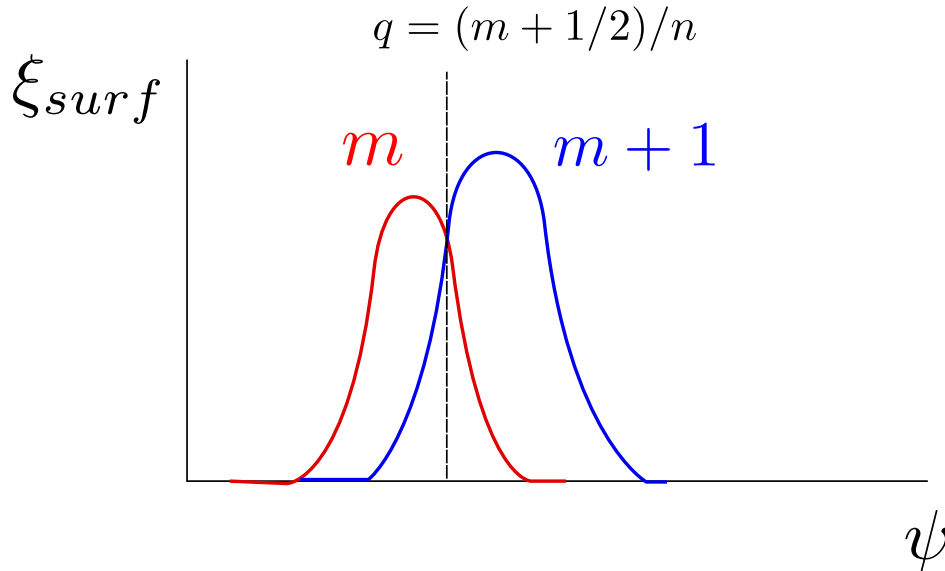


Figure 1.3 Cartoon showing the m and $m + 1$ poloidal harmonics coupled together to produce the Toroidicity-induced Alfvén Eigenmode (TAE). Both Fourier components have toroidal mode number n . The mode is localized at the surface where the safety factor is $q = (m + 1/2)/n$.

1.2.3 Discrete Alfvén eigenmodes (AEs)

Once a frequency gap is formed in the continuous spectrum as discussed in Sec. 1.2.2 for the TAE, discrete shear Alfvén eigenmodes (AEs), also known as gap modes, can form within the gap. These modes are essentially standing waves and are characterized by a finite radial extent and an eigenfrequency that lies in the gap frequency range. The global structure of an AE contains the poloidal and toroidal harmonics of the coupled continuum waves that created the gap. The coupling for a TAE mode is shown schematically in Fig. 1.3. The mode is localized around the $q = (m + 1/2)/n$ surface where the gap is centered and is dominated by m and $m + 1$ Fourier components, the same harmonics involved in the continuum coupling that formed the gap.

Gap modes are of particular interest as potential instabilities in fusion plasmas, since they can be driven unstable by interactions with energetic particles. Gap modes are generally weakly stable, but because they exist in a frequency gap they do not experience continuum damping by coupling to neighboring continuum waves. Without this damping process, it takes a relatively small drive from energetic particles to drive AEs unstable.

Mathematically, the cross-surface coupling present in the global structure of AEs makes them much more difficult to study analytically compared to continuum modes. To this end, reduced MHD equations are generally employed [21, 16, 5, 22]. While the details move beyond the scope of this work, the basic starting equations for AEs in a three-dimensional equilibrium are the ideal MHD Ohm's law and the vorticity equation written in terms of the electrostatic potential ϕ :

$$\frac{\partial \delta\psi}{\partial t} = \frac{1}{B} \mathbf{B} \cdot \nabla \phi, \quad (1.35)$$

$$\nabla \cdot \left[\frac{\rho}{B} \frac{d}{dt} \left(\frac{\nabla \phi}{B} \right) \right] = \mathbf{B} \cdot \nabla \frac{\delta J_{\parallel}}{B} + \delta \mathbf{B} \cdot \nabla \frac{J_{\parallel}}{B}. \quad (1.36)$$

Here $\delta\psi$ is the perturbed poloidal magnetic flux. Using the relations $\delta J_{\parallel} = \nabla^2 \delta\psi$ and $\delta \mathbf{B} = \nabla \zeta \times \nabla \delta\psi$ and inserting Eq. (1.35) into Eq. (1.36) gives the following eigenvalue equation:

$$\omega^2 \nabla \cdot \left(\frac{1}{v_A^2} \nabla \phi \right) + \mathbf{B} \cdot \nabla \left[\frac{1}{B} \nabla^2 \left(\frac{\mathbf{B}}{B} \cdot \nabla \phi \right) \right] + \nabla \zeta \times \nabla \left(\frac{\mathbf{B}}{B} \cdot \nabla \phi \right) \cdot \nabla \frac{J_{\parallel}}{B} = 0. \quad (1.37)$$

In this equation, the first term provides the inertia and the second provides the field-line bending. Both of these terms are also present in the continuum equations. However, a third ballooning term is also present in this formulation for discrete AEs which is not included in the equations for the continuum waves. The eigenmode solutions ϕ to this equation represent the discrete Alfvén modes together with the mode frequencies ω^2 . Even though reduced MHD has been used here, the complexity of this equation usually requires it to be solved computationally. Solution of Eq. (1.37) using the AE3D code will be discussed in Chapter 4.

An extensive taxonomy of AEs exists. Along with the previously discussed TAE, the Alfvén zoo contains the beta-induced Alfvén eigenmode (BAE), the ellipticity-induced Alfvén eigenmode (EAE), the mirror-induced Alfvén eigenmode (MAE), and the helicity-induced Alfvén eigenmode (HAE), just to name a few. All of these modes and corresponding frequency gaps arise due to various couplings between poloidal and/or toroidal harmonics. The coupling is caused from a different physical or geometric mechanism in each case, but each is due to the effects of a broken symmetry on the interactions of counter-propagating waves. Most of these modes have been observed extensively on various experiments [23, 24, 25, 26, 27]. The BAE and HAE will both be discussed in some detail in this thesis, along with the identification of a new type of AE, the Island-induced Alfvén Eigenmode (IAE).

Chapter 2

Analytical theory of the shear Alfvén continuum in the presence of a magnetic island

Most theoretical descriptions of the Alfvén spectrum rely on the existence of topologically toroidal flux surfaces. In this chapter, the effect of a magnetic island chain on the shear Alfvén continuum is calculated analytically. Using a WKB approximation of the linearized ideal MHD equations, the island is shown to cause an upshift in the continuum accumulation point frequency. This minimum of the frequency spectrum is shifted from the rational surface to the island separatrix. The structure of the eigenmodes is also presented.

2.1 Island coordinate system

In order to obtain the Alfvén continuum, a straight field-line representation of the equilibrium magnetic field that includes the island has been employed [28, 29]. The island will be treated as a static feature of the equilibrium, a good approximation since tearing mode timescales are generally much longer than the Alfvén timescales of interest here, $\omega_{tearing} \ll \omega_A$. The portion of the field without an island is represented in straight field-line coordinates as $\mathbf{B}_0 = q\nabla\psi \times \nabla\theta + \nabla\zeta \times \nabla\psi$, where ψ is the poloidal flux and θ and ζ are the poloidal and toroidal coordinates respectively; q is the safety factor. A symmetry-breaking magnetic field of the form $\sqrt{g}\mathbf{B}_1 \cdot \nabla\psi = n_0 A \sin(m_0\theta - n_0\zeta)$ causes an island to form at $q(\psi_0) = q_0 = m_0/n_0$. Here, the Jacobian is $\sqrt{g} = (\nabla\psi \times \nabla\theta \cdot \nabla\zeta)^{-1}$. The constant- ψ approximation of tearing mode analysis is utilized in this work, allowing us to treat A as a constant throughout the island region [30].

A coordinate transformation to (Ψ^*, χ, α) space given by

$$\begin{aligned}\Psi^* &= \int d\psi(q - q_0) - A \cos(n_0\alpha) \\ &\approx q'_0 \frac{x^2}{2} - A \cos(n_0\alpha),\end{aligned}\tag{2.1}$$

$$\chi = \theta,\tag{2.2}$$

$$\alpha = \zeta - q_0\theta,\tag{2.3}$$

is employed as a first step to derive a straight field representation for the total magnetic field. Here $x = \psi - \psi_0$ is the distance from the rational surface and $q'_0 = dq/d\psi|_{\psi=\psi_0}$. These coordinates comprise a Hamiltonian system analogous to the pendulum, where (ψ, α) are the action-angles, Ψ^* is the Hamiltonian, and χ is the time-like coordinate [31]. The magnetic island width is given by $w = 4\sqrt{|A/q'_0|}$, and the island width will be considered small compared to equilibrium scales throughout this analysis, $\epsilon = q'_0 w/2 \ll 1$. Ψ^* is a flux surface label, $\mathbf{B} \cdot \nabla \Psi^* = 0$ for the equilibrium in the presence of an island. See Fig. 2.1 for a visualization of the island coordinates. The island O-point is located at $\Psi^* = -A$ and the separatrix is at $\Psi^* = A$.

This transformation allows the total equilibrium field including the magnetic island $\mathbf{B} = \mathbf{B}_0 + \mathbf{B}_1$ to be written as

$$\mathbf{B} = \nabla\alpha \times \nabla\psi + \nabla\Psi^* \times \nabla\chi.\tag{2.4}$$

Next the coordinates $\Phi^* = \Phi^*(\Psi^*)$ and α^* are defined such that

$$\nabla\alpha \times \nabla\psi = \nabla\alpha^* \times \nabla\Phi^*,\tag{2.5}$$

$$\frac{\partial x}{\partial \Phi^*} = \frac{\Omega}{q'_0 x},\tag{2.6}$$

$$\frac{\partial \alpha}{\partial \alpha^*} = \frac{q'_0 x}{\Omega}.\tag{2.7}$$

Φ^* labels flux surfaces along with Ψ^* , and α^* is a helical angle in the reference frame of the island with $(0, 2\pi)$ periodicity on each helical flux surface. The definitions of Φ^* and α^* inside and outside the island separatrix are presented in Appendix C. The island rotational transform Ω introduced here can be computed with the following:

$$\Omega(\Psi^*) = \frac{d\Psi^*}{d\Phi^*} = \frac{1}{\oint \frac{n_0 d\alpha}{2\pi} \left[1 / \frac{\partial \Psi^*}{\partial x} \right]}.\tag{2.8}$$

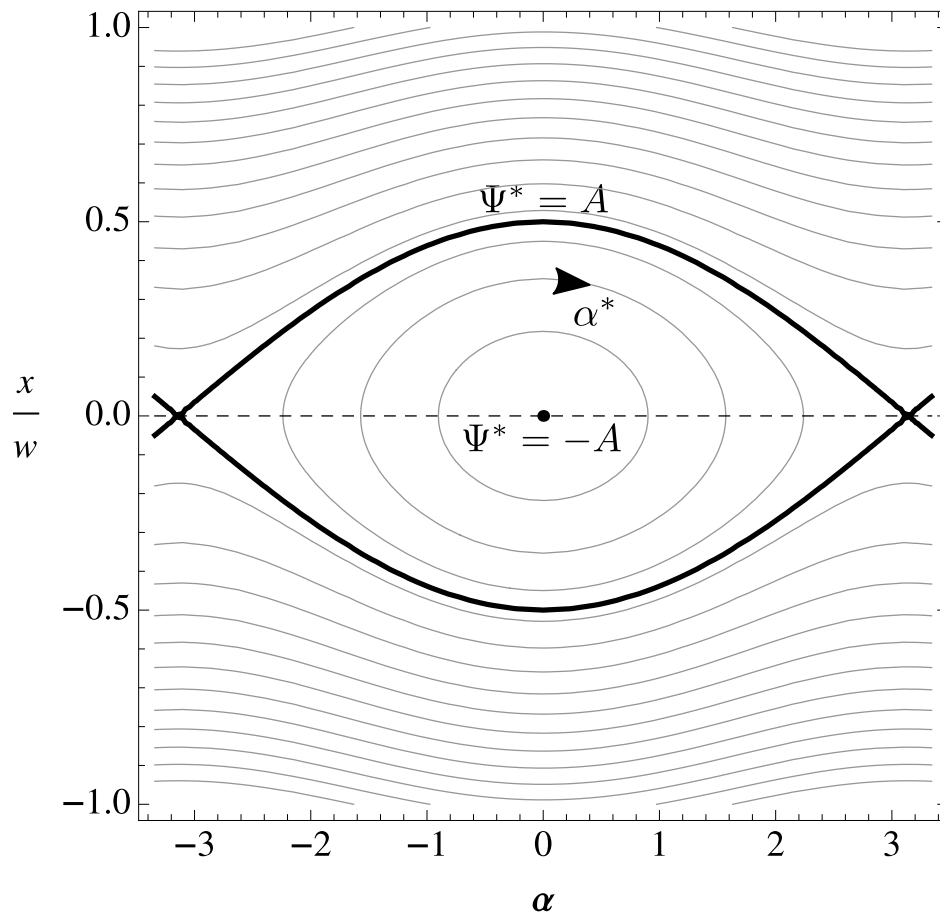


Figure 2.1 Island coordinate system for $n_0 = 1$. Surfaces of constant $\Psi^*/\text{constant } \Phi^*$ appear as contours in the plot.

Here, the distance x from the rational surface can be written in terms of Ψ^* and α as $x = \pm\sqrt{2/q'_0(\Psi^* + A \cos(n_0\alpha))}$.

Outside the island separatrix, $|\Psi^*| > A$, it is useful to define a flux surface label $k^2 = 2A/(|\Psi^*| + A)$. In this parameter, the separatrix is located at $k = 1$. The island rotational transform outside the island is given by

$$\Omega = \pm \frac{\pi\epsilon}{2kK(k^2)}, \quad (2.9)$$

where $\epsilon = q'_0 w/2$ is the island half width (our small parameter) and $K(k^2)$ is the complete elliptic integral of the first kind. The plus and minus signs correspond to surfaces with $x > 0$ ($\psi > \psi_0$) and $x < 0$ ($\psi < \psi_0$), respectively.

Inside the island, $-A < \Psi^* < A$, we will label flux surfaces with $\kappa^2 = (\Psi^* + A)/2A$. The O-point is at $\kappa = 0$ and the separatrix is at $\kappa = 1$. Written with this surface label, the island rotational transform inside the magnetic island is the following:

$$\Omega(\Psi^*) = \frac{\pi\epsilon}{4K(\kappa^2)}. \quad (2.10)$$

A derivation of the rotational transform inside the separatrix is given in Appendix B. Fig. 2.2 displays the helical rotational transform both inside and outside the island.

Using this island coordinate system, the total magnetic field can be written in a straight field form as

$$\mathbf{B} = \mathbf{B}_0 + \mathbf{B}_1 = \nabla\alpha^* \times \nabla\Phi^* + \Omega\nabla\Phi^* \times \nabla\chi. \quad (2.11)$$

This allows us to write the derivative along the magnetic field line in a much simpler form:

$$\mathbf{B} \cdot \nabla\lambda = \frac{1}{\sqrt{g}} \left[\frac{\partial\lambda}{\partial\chi} + \Omega \frac{\partial\lambda}{\partial\alpha^*} \right]. \quad (2.12)$$

This parallel gradient operator will be used in the next section when deriving the model equations.

2.2 Ideal MHD in the presence of an island

In order to study the Alfvén spectrum in the vicinity of an island, a linearized ideal MHD model has been implemented. Throughout this manuscript, an equilibrium with a finite-sized magnetic island will be assumed. This is reflected in the equilibrium magnetic field representation $\mathbf{B} =$

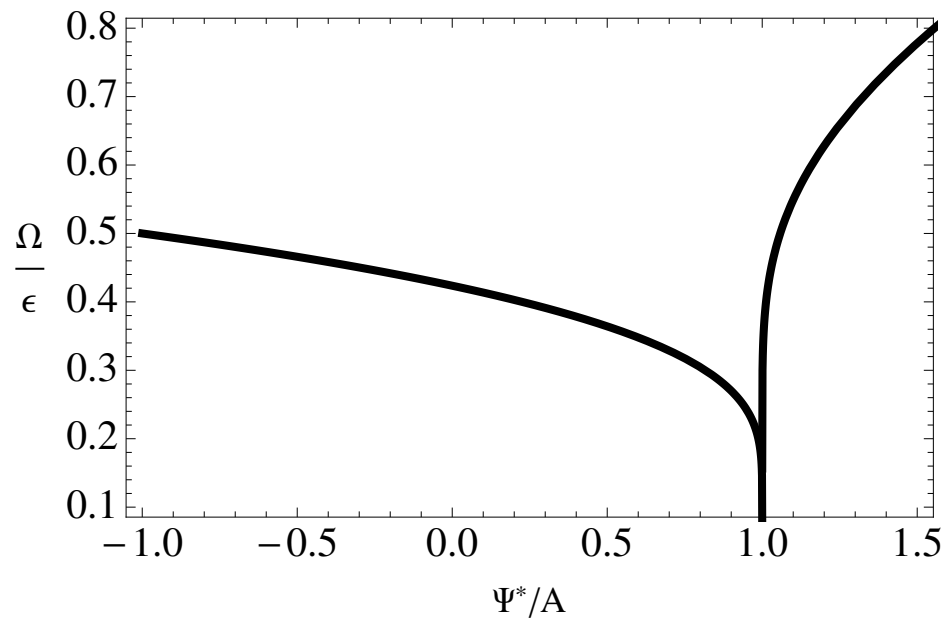


Figure 2.2 Island rotational transform inside and outside the island. Note that $\Omega \rightarrow 0$ at the separatrix, $\Psi^* = A$.

$\nabla\alpha^* \times \nabla\Phi^* + \Omega\nabla\Phi^* \times \nabla\chi$ derived in the last section. The equilibrium quantities satisfy force balance, Ampère's Law, and the divergence constraint:

$$\mathbf{J} \times \mathbf{B} = \nabla p, \quad (2.13)$$

$$\nabla \times \mathbf{B} = \mathbf{J}, \quad (2.14)$$

$$\nabla \cdot \mathbf{B} = 0. \quad (2.15)$$

The linearized ideal MHD equations are the momentum equation, the combined Faraday's law/Ohm's law, and the equation of state (natural units for plasmas, $\mu_0, \epsilon_0 = 1$, will be used throughout this dissertation). The linear system of equations for the MHD displacement vector $\boldsymbol{\xi}$, magnetic field perturbation $\delta\mathbf{B}$, and pressure perturbation δp is given by

$$-\rho\omega^2\boldsymbol{\xi} = (\nabla \times \mathbf{B}) \times \delta\mathbf{B} + (\nabla \times \delta\mathbf{B}) \times \mathbf{B} - \nabla\delta p, \quad (2.16)$$

$$0 = \delta p + \boldsymbol{\xi} \cdot \nabla p + \gamma p \nabla \cdot \boldsymbol{\xi}, \quad (2.17)$$

$$\delta\mathbf{B} = \nabla \times (\boldsymbol{\xi} \times \mathbf{B}). \quad (2.18)$$

Following Cheng and Chance's treatment (as discussed in Sec. 1.2.1), but now using the variables $\nabla \cdot \boldsymbol{\xi}$, $\xi^{\Phi^*} = \boldsymbol{\xi} \cdot \nabla\Phi^*$, $\delta P = \delta p + \delta\mathbf{B} \cdot \mathbf{B}$, and the perpendicular surface component of the MHD displacement $\xi_s = \boldsymbol{\xi} \cdot (\mathbf{B} \times \nabla\Phi^*)/|\nabla\Phi^*|^2$, the ideal MHD eigenmode equations can be written in matrix form as [16]

$$\nabla\Phi^* \cdot \nabla \begin{bmatrix} \delta P \\ \xi^{\Phi^*} \end{bmatrix} = C \begin{bmatrix} \delta P \\ \xi^{\Phi^*} \end{bmatrix} + D \begin{bmatrix} \xi_s \\ \nabla \cdot \boldsymbol{\xi} \end{bmatrix}, \quad (2.19)$$

$$E \begin{bmatrix} \xi_s \\ \nabla \cdot \boldsymbol{\xi} \end{bmatrix} = F \begin{bmatrix} \delta P \\ \xi^{\Phi^*} \end{bmatrix}, \quad (2.20)$$

where C , D , E , and F are complicated operators containing only surface derivatives. The details of these operators are found in Appendix A. The Alfvén and sound continua arise from solutions with a non-square-integrable singular radial structure. These solutions occur when the operator E does not have an inverse. Thus to find these continuum modes and their eigenfrequencies, ω^2 ,

which compose the spectrum, the following system must be solved for every surface in the domain:

$$E \begin{bmatrix} \xi_s \\ \nabla \cdot \boldsymbol{\xi} \end{bmatrix} = 0. \quad (2.21)$$

In a general toroidal equilibrium with nonzero geodesic curvature $\kappa_s \neq 0$, the two equations in Eq. (2.21) give a coupling of the Alfvén and sound waves. Writing out this system of two equations gives the MHD eigenmode equations, where the shear Alfvén and acoustic continuum modes are coupled through pressure and curvature:

$$0 = \omega^2 \rho \frac{|\nabla\Phi^*|^2}{B^2} \xi_s + \mathbf{B} \cdot \nabla \left(\frac{|\nabla\Phi^*|^2}{B^2} \mathbf{B} \cdot \nabla \xi_s \right) + \gamma p \kappa_s \nabla \cdot \boldsymbol{\xi}, \quad (2.22)$$

$$0 = \kappa_s \xi_s + \left(\frac{\gamma p + B^2}{B^2} \right) \nabla \cdot \boldsymbol{\xi} + \frac{\gamma p}{\omega^2 \rho} \mathbf{B} \cdot \nabla \left(\frac{1}{B^2} \mathbf{B} \cdot \nabla (\nabla \cdot \boldsymbol{\xi}) \right). \quad (2.23)$$

The shear Alfvén waves are primarily governed by Eq. (2.22) while sound waves are mostly controlled by Eq. (2.23), but the coupling is apparent. The slow sound approximation $\gamma p / \rho \omega^2 R_0^2 \ll 1$ reduces the system to a single equation while still retaining the acoustic effects to lowest order [32]. Taking this approximation to first order results in

$$\omega^2 \rho \frac{|\nabla\Phi^*|^2}{B^2} \xi_s + \mathbf{B} \cdot \nabla \left(\frac{|\nabla\Phi^*|^2}{B^2} \mathbf{B} \cdot \nabla \xi_s \right) - \frac{\gamma p \kappa_s^2 B^2}{\gamma p + B^2} \xi_s = 0. \quad (2.24)$$

The minimum frequency of the spectrum is known as the BAE-CAP (continuum accumulation point) frequency, which in the absence of an island occurs at the rational surface where $\mathbf{B} \cdot \nabla \sim (m_0 - n_0 q) = 0$. Setting the parallel gradient term to zero in Eq. (2.24), the BAE-CAP frequency becomes approximately $\omega_{BAE}^2 = \langle \kappa_s \rangle^2 \gamma p B^4 / \rho |\nabla\psi|^2 (\gamma p + B^2)$, where all the values are evaluated at the resonant surface, and we are assuming the island component of \mathbf{B} is small compared to the toroidal component [32, 33]. In this expression, the $\sin\theta$ dependence of κ_s is removed through flux-surface averaging. This expression makes clear the importance of both the plasma pressure and the curvature; both are required for a non-zero BAE-CAP frequency. In a cylinder the geodesic

curvature is zero, and the Alfvén continuum goes to zero at the rational surface. When the cylinder is wrapped into a torus, the curvature couples the shear Alfvén and acoustic waves, and the BAE-CAP frequency becomes non-zero. Substituting ω_{BAE} into Eq. (2.24) results in the general eigenmode equation:

$$(\omega^2 - \omega_{BAE}^2)\rho \frac{|\nabla\Phi^*|^2}{B^2}\xi_s + \mathbf{B} \cdot \nabla \left(\frac{|\nabla\Phi^*|^2}{B^2}\mathbf{B} \cdot \nabla\xi_s \right) = 0. \quad (2.25)$$

For a cylindrical equilibrium with an island, the geodesic curvature given by $\kappa_s = 2\boldsymbol{\kappa} \cdot (\mathbf{B} \times \nabla\psi/B^2)$ is zero and the Alfvén and acoustic continua decouple. The general eigenmode equation for the shear Alfvén waves from Eq. (2.21) is then

$$\omega^2\rho \frac{|\nabla\Phi^*|^2}{B^2}\xi_s + \mathbf{B} \cdot \nabla \left(\frac{|\nabla\Phi^*|^2}{B^2}\mathbf{B} \cdot \nabla\xi_s \right) = 0. \quad (2.26)$$

This equation is the same as Eq. (2.25), but without the frequency upshift by ω_{BAE}^2 [32, 33]. For the work that follows we will simply use ω^2 as in Eq. (2.26), but everything can be generalized to a torus in the slow sound limit by replacing ω^2 with $\omega^2 - \omega_{BAE}^2$ as is done in Eq. (2.25).

If we assume that the surface displacement can be described with a quantum number l in the island direction χ , $\xi_s(\chi, \alpha^*) = \xi_0(\alpha^*) \exp(il\chi)$, then the parallel gradient operator given by Eq. (2.12) can be written as

$$\begin{aligned} \mathbf{B} \cdot \nabla\xi_s &= \frac{1}{\sqrt{g}} \left(\Omega \frac{\partial}{\partial\alpha^*} + il \right) \xi_s \\ &= \frac{1}{\sqrt{g}} e^{-\frac{il}{\Omega}\alpha^*} \Omega \frac{\partial}{\partial\alpha^*} \left(\xi_s e^{\frac{il}{\Omega}\alpha^*} \right). \end{aligned} \quad (2.27)$$

Substituting this back into Eq. (2.26) results in

$$\frac{d}{d\alpha^*} \left(|\nabla\Phi^*|^2 \frac{d}{d\alpha^*} Y \right) + \omega^2 \rho \frac{\sqrt{g}^2}{\Omega^2} |\nabla\Phi^*|^2 Y = 0, \quad (2.28)$$

where we have set $Y = \xi_0(\alpha^*) \exp(il\alpha^*/\Omega)$. Thus a second-order ODE for the Alfvén eigenspectrum is obtained for each flux surface in the presence of a magnetic island.

2.3 WKB analysis of continuum equation

The result derived in the last section, Eq. (2.28), can be rewritten with the identification $|\nabla\Phi^*|^2 = (g'_0 x/\Omega)^2 |\nabla\psi|^2$ and a normalized frequency given by $\hat{\omega}^2 = \omega^2/\omega_A^2$. Here the Alfvén

frequency is $\omega_A = 1/[\sqrt{\rho}\sqrt{g}]$. Employing these definitions simplifies the eigenmode equation as follows:

$$\frac{d}{d\alpha^*} \left[x^2 \frac{d}{d\alpha^*} Y \right] + \frac{\hat{\omega}^2 x^2}{\Omega^2} Y = 0. \quad (2.29)$$

From Eq. (2.29), the frequency $\hat{\omega}^2$ can be shown to be positive:

$$\hat{\omega}^2 = \Omega^2 \frac{\oint d\alpha^* x^2 \left| \frac{dY}{d\alpha^*} \right|^2}{\oint d\alpha^* x^2 |Y|^2} \geq 0. \quad (2.30)$$

Thus the square of the Alfvén spectrum frequencies cannot be negative, meaning the spectrum is stable. In the following, we will show that the presence of the island causes a non-zero upshift to the minimum frequency.

Eq. (2.29) can be written in terms of a dimensionless distance from the rational surface, $\hat{x} = \sqrt{\kappa^2 - \sin^2 n_0 \alpha / 2}$ where $x = (w/2)\hat{x}$. This results in our final form of the continuum equation, cast in Schrödinger form:

$$\frac{\Omega^2}{\hat{\omega}^2} \hat{x}^2 \frac{d}{d\alpha^*} \left[\hat{x}^2 \frac{d}{d\alpha^*} Y \right] + \hat{x}^4 Y = 0. \quad (2.31)$$

The representation of \hat{x} in α^* -space is included in Appendix C. Here we will consider $l = 0$ in $\xi_s = Y(\alpha^*) \exp[il(\chi - \alpha^*/\Omega)]$, so our solutions are equal to the surface displacements, $Y = \xi_s$. Our boundary conditions are periodic in α^* :

$$Y(\alpha^*) = Y(\alpha^* + 2\pi), \quad (2.32)$$

$$\left. \frac{dY}{d\alpha^*} \right|_{\alpha^*} = \left. \frac{dY}{d\alpha^*} \right|_{\alpha^* + 2\pi}. \quad (2.33)$$

Eq. (2.31) lends itself to a WKB analysis (named after Wentzel-Kramers-Brillouin). Comparing the equation to the canonical Schrödinger equation

$$\delta^2 \frac{d^2 Y}{dt^2} - Q(t)Y = 0, \quad (2.34)$$

yields the following identities:

$$Q = -\hat{x}^4, \quad (2.35)$$

$$\delta = \frac{\Omega}{\hat{\omega}}, \quad (2.36)$$

$$\frac{d\alpha^*}{dt} = \hat{x}^2. \quad (2.37)$$

The formal WKB expansion for the solution is $Y \sim \exp[(1/\delta) \sum \delta^n S_n(t)]$, where the summation is from $n = 0$ to ∞ and the small parameter $\delta \sim \Omega \sim \epsilon$. Inserting this expansion into the general Schrödinger equation and solving to second order gives the following solutions for S_0 , S_1 , and S_2 in terms of the potential Q :

$$S_0 = \pm \int \sqrt{Q} dt, \quad (2.38)$$

$$S_1 = -\frac{1}{4} \log Q, \quad (2.39)$$

$$S_2 = \pm \int \left[\frac{Q''}{8Q^{3/2}} - \frac{5(Q')^2}{32Q^{5/2}} \right] dt. \quad (2.40)$$

Inserting $Q = -\hat{x}^4$ into the lowest two orders and working out the details gives

$$S_0 = \pm i\alpha^*, \quad (2.41)$$

$$S_1 = -\frac{1}{4} \log(-\hat{x}^4), \quad (2.42)$$

The specific form of S_2 is presented in Appendix C for surfaces both inside and outside the separatrix.

Substituting S_0, S_1 , and S_2 into $Y \sim \exp[S_0/\delta + S_1 + \delta S_2]$ results in the following WKB solution:

$$Y \sim \frac{1}{\hat{x}} e^{\pm i \left(\frac{\hat{\omega}}{\hat{\Omega}} \alpha^* + \frac{\hat{\Omega}}{\hat{\omega}} \hat{S}_2(\alpha^*) \right)}. \quad (2.43)$$

Here $S_2(\alpha^*) = \pm i \hat{S}_2(\alpha^*)$. The plus and minus signs correspond to two linearly independent solutions for the second-order ODE. These two solutions can be combined to form odd and even solutions given by the following:

$$Y_O \sim \frac{1}{\hat{x}} \sin \left(\frac{\hat{\omega}}{\hat{\Omega}} \alpha^* + \frac{\hat{\Omega}}{\hat{\omega}} \hat{S}_2(\alpha^*) \right), \quad (2.44)$$

$$Y_E \sim \frac{1}{\hat{x}} \cos \left(\frac{\hat{\omega}}{\hat{\Omega}} \alpha^* + \frac{\hat{\Omega}}{\hat{\omega}} \hat{S}_2(\alpha^*) \right). \quad (2.45)$$

With this result, we will derive the structure of the eigenmodes and the corresponding shear Alfvén eigenspectrum in the next section.

2.4 Alfvén continuum and eigenmode structure

The solutions from Eqs. (2.44) and (2.45) can be made consistent with the periodic boundary conditions given in Eqs. (2.32) and (2.33). The resulting continuum frequencies are given by

$$\hat{\omega}^2 = \left[\frac{j\Omega}{2} + \sqrt{\left(\frac{j\Omega}{2}\right)^2 + \frac{q'_0}{2} \left(\Psi^* - \frac{1}{2}\Omega\Phi^*\right)} \right]^2, \quad (2.46)$$

where j is a positive integer. We will see that outside the separatrix, $j = j_{out}$ where $j_{out} = 1, 2, 3, \dots$ is the quantum number. Inside the separatrix, $j = n_0(j_{in} + 1)$ where $j_{in} = 1, 2, 3, \dots$ is the quantum number for the interior region of the island. Eq. (2.46) represents the shear Alfvén eigenspectrum, valid for surfaces inside and outside the separatrix. In order to investigate the nature of the eigenmodes, we will consider surfaces both inside and outside the separatrix.

For flux surfaces outside the island, the envelope function $1/\hat{x}$ of the solution remains well-behaved since \hat{x} does not pass through zero. Due to this, modes of both parities are allowed for all quantum numbers outside the separatrix, giving us the following eigenmodes outside the island:

$$Y_O^j = \frac{1}{\sqrt{\pi\hat{x}(\alpha^*)}} \sin [j_{out}\alpha^*], \quad (2.47)$$

$$Y_E^j = \frac{1}{\sqrt{\pi\hat{x}(\alpha^*)}} \cos [j_{out}\alpha^*]. \quad (2.48)$$

Here the quantum number $j_{out} = 1, 2, 3, \dots$. The coefficient comes from the normalization condition, $\oint d\alpha^* \hat{x}^2 |Y|^2 = 1$.

For surfaces within the island, the envelope of the solutions contains an apparent $1/\hat{x}$ singularity occurring when $\hat{x} = 0$ at $\alpha^* = \pi/2n_0$. This singularity can be removed by forcing the trigonometric functions in Eqs. (2.44) and (2.45) to zero at $\alpha^* = \pi/2n_0$. Under this constraint we lose half of the solutions inside the island, and our eigenmodes are odd for j_{in} odd and even for j_{in} even:

$$Y_O^j = \frac{1}{\sqrt{\pi\hat{x}(\alpha^*)}} \sin [n_0(j_{in} + 1)\alpha^*], \quad j_{in} = 1, 3, 5, \dots, \quad (2.49)$$

$$Y_E^j = \frac{1}{\sqrt{\pi\hat{x}(\alpha^*)}} \cos [n_0(j_{in} + 1)\alpha^*], \quad j_{in} = 2, 4, 6, \dots \quad (2.50)$$

This restriction on parity inside the island is a new result, not identified by Biancalani et al. [12]. In Biancalani's work, the Alfvén continuum was solved numerically using a shooting code. In this solution method, the boundary conditions (j_{in} and parity) are entered by hand to initialize the simulation. This numerical approach did not take the correct steps to ensure regularity. In lieu of a proper analytic treatment as presented here there is no reason to assume that odd and even parities can't both exist for all values of j_{in} , and thus Biancalani's computational results inside the island incorrectly contain both the odd and even modes. Only half of these continuum modes survive when the boundary conditions are handled properly as shown here for the analytical solution, with odd parity for j_{in} odd and even parity for j_{in} even.

Now that we have the equation for the shear Alfvén continuum and the corresponding continuum modes, we can look at the structure of the spectrum. The Alfvén eigenspectrum given by Eq. (2.46) is plotted in Fig. 2.3. Note that Eq. (2.31) can be solved analytically at the O-point ($\Psi^* = -A$), resulting in $\hat{\omega}^2/\epsilon^2 = n_0^2 j_{in} (j_{in} + 2) / 4$. This agrees well with our second-order WKB approximated solution at the O-point plotted in Fig. 2.3. The analytic solution of the continuum at the O-point is presented in Sec. 2.5.

Two zero frequency modes, $\hat{\omega}^2 = 0$, have been included in the figure as purple points; one is located at the O-point and the other at the X-point of the separatrix. The solution $\hat{\omega}^2 = 0$ with Y a constant is a known, trivial solution to the Alfvén eigenmode equation for any magnetic geometry and is generally not included. It is usually neglected because the quantum numbers are zero which makes the eigenmode a constant. It is included and important at the singular O- and X-points here because in the original θ and ζ coordinates from the toroidal magnetic field, the quantum numbers are non-zero. Indeed, the zero frequency behavior at the O-point and X-point corresponds to $m = m_0, n = n_0$. This means that the O-point and X-point retain the marginal stability ($\hat{\omega}^2 = 0$) inherent in the original resonant, rational surface ψ_0 . As such, the O-point and X-point will still be only marginally stable to $m = m_0$ and $n = n_0$ perturbations.

The behavior of the spectrum near the separatrix ($\Psi^* = A$) is of considerable interest. Since the rotational transform Ω goes to zero at the separatrix, $\delta = \Omega/\hat{\omega} \rightarrow 0$, the WKB expansion is formally valid for all finite j at the separatrix. Fig. 2.4 provides a close-up of the spectrum

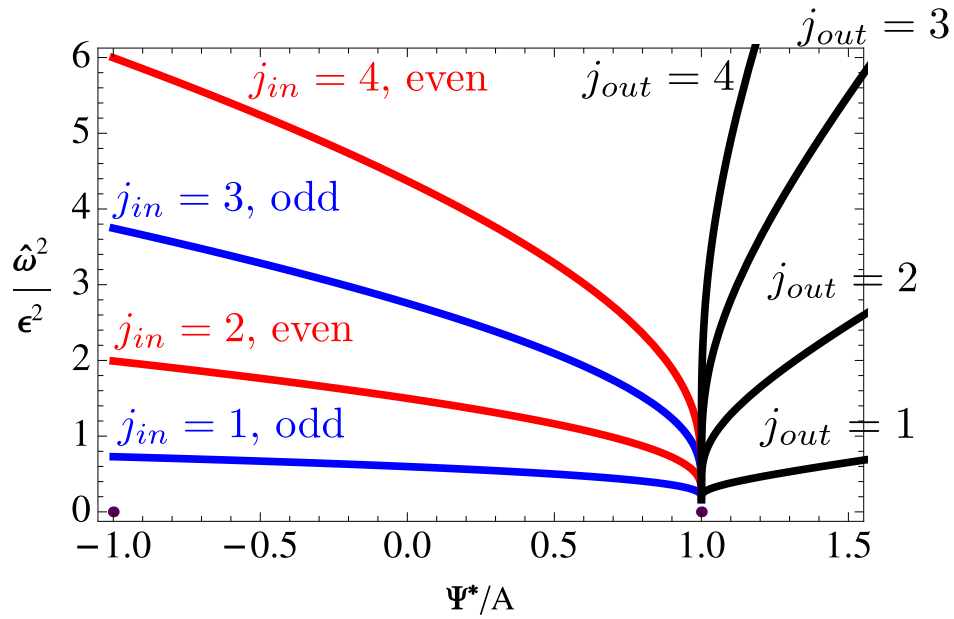


Figure 2.3 Shear Alfvén continuum in the presence of a magnetic island. Inside the separatrix, the frequencies of the odd modes are blue curves while the even modes are red. Outside the separatrix, both parities exist at the same frequency.

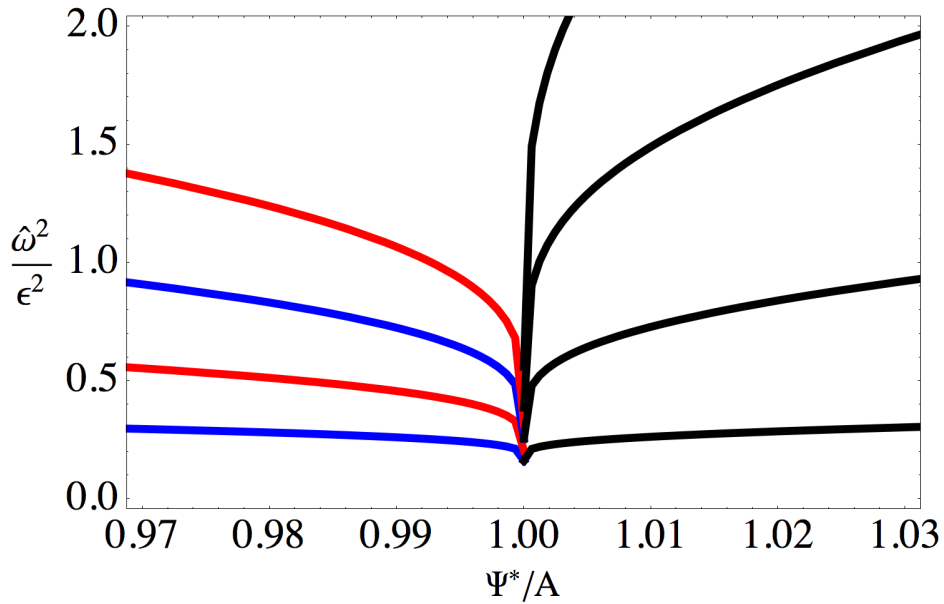


Figure 2.4 Shear Alfvén continuum behavior near the separatrix ($\Psi^* = A$). Note that all branches of the continuum limit to a non-zero frequency at the separatrix, $\hat{\omega}_{sep}^2/\epsilon^2 = 1/8$.

for surfaces near the separatrix. It can be seen that all of the frequencies converge to an island-modified, non-zero continuum accumulation point frequency at the separatrix. Every continuum branch limits to the same frequency at the separatrix, and the value of this minimum limiting frequency is

$$\left(\frac{\hat{\omega}_{sep}}{\epsilon}\right)^2 = \lim_{\Psi^* \rightarrow A} \left(\frac{\hat{\omega}}{\epsilon}\right)^2 = \frac{1}{8}. \quad (2.51)$$

This minimum frequency at the separatrix can be written out explicitly as $\omega_{sep}^2 = (q'_0 w)^2 \omega_A^2 / 32$. After transforming to the proper coordinates, this is the same frequency upshift that was previously found numerically by Biancalani [12] (see Appendix D for coordinate conversions). This minimum continuum accumulation point suggests the possibility of global BAE (beta-induced Alfvén eigenmodes) below this frequency gap. BAEs in the presence of an island will be discussed in Sec. 3.4 for MST and tokamaks.

The lowest two eigenmodes for each parity outside the separatrix given by Eqs. (2.47) and (2.48) are plotted in Fig. 2.5 for $\Psi^* = 2A$ ($k^2 = 2/3$). The lowest two eigenmodes inside the separatrix given by Eqs. (2.49) and (2.50) are plotted in Fig. 2.6 for $\Psi^* = A/2$ ($\kappa^2 = 3/4$).

2.5 Exact continuum solution at the O-point

Note that Eq. (2.31) can be solved analytically at the O-point, $\Psi^* = -A$. For reference, the continuum equation derived in Sec. 2.3 is

$$\frac{\Omega^2}{\hat{\omega}^2} \hat{x}^2 \frac{d}{d\alpha^*} \left[\hat{x}^2 \frac{d}{d\alpha^*} Y \right] + \hat{x}^4 Y = 0. \quad (2.31)$$

The equation can be recast by letting $Y = f(\alpha^*)/\hat{x}$. After substituting this into Eq. (2.31), one arrives at a differential equation for f :

$$\frac{d^2 f}{d\alpha^{*2}} + \left(\frac{\hat{\omega}^2}{\Omega^2} - \frac{\hat{x}''}{\hat{x}} \right) f = 0. \quad (2.52)$$

Here $\hat{x}'' = d^2 \hat{x} / d\alpha^{*2}$. This equation can be rewritten in the following suggestive form:

$$-\frac{d^2 f}{d\alpha^{*2}} + \frac{\hat{x}''}{\hat{x}} f = \frac{\hat{\omega}^2}{\Omega^2} f. \quad (2.53)$$

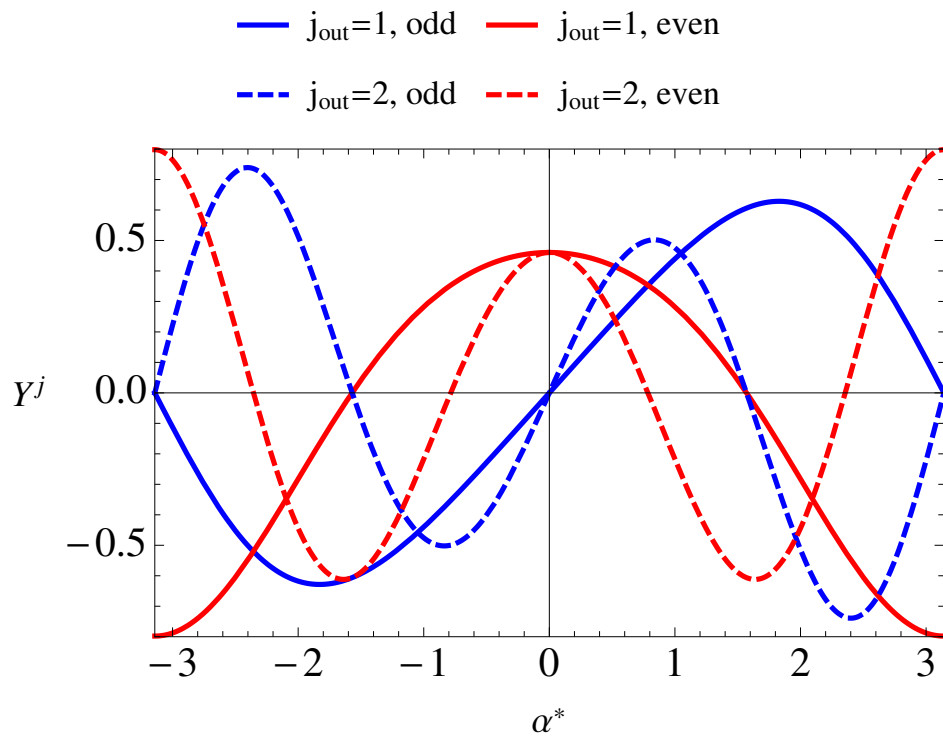


Figure 2.5 $j_{out} = 1$ (solid) and $j_{out} = 2$ (dashed) mode structure for $\Psi^* = 2A$ surface outside the island. Outside the separatrix, even and odd parities are both present and degenerate in frequency.

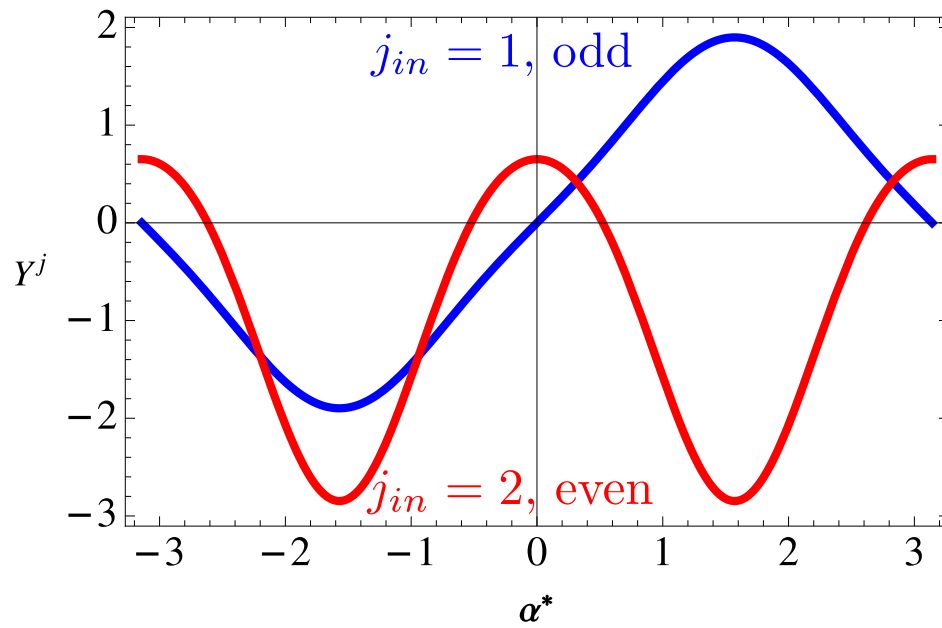


Figure 2.6 $j_{in} = 1$ odd (blue) and $j_{in} = 2$ even (red) mode structure for $\Psi^* = A/2$ surface inside the island. Inside the separatrix, odd j_{in} correspond to odd modes and even j_{in} correspond to even modes.

The continuum equation is thus mathematically equivalent to a 1D time-independent Schrödinger equation from quantum mechanics, which is given by

$$-\frac{\hbar^2}{2m} \frac{d^2}{dx^2} \psi + V\psi = E\psi. \quad (2.54)$$

From this it is apparent that the potential V for the continuum equation is $V = \hat{x}''/\hat{x}$. Since Eq. (2.53) is a general result for all flux surfaces in the domain, we now turn to finding where the potential lends itself to an analytic solution.

For surfaces inside the island separatrix, the normalized distance from the rational surface in terms of α^* is given by $\hat{x} = \kappa cn [2n_0 K(\kappa^2) \alpha^* / \pi, \kappa^2]$, where cn is the Jacobi elliptic function. Thus for a general surface inside the island, the potential is

$$V = \frac{\hat{x}''}{\hat{x}} = \left(\frac{2n_0 K(\kappa^2)}{\pi} \right)^2 \left[2\kappa^2 sn^2 \left(\frac{2n_0 K(\kappa^2)}{\pi} \alpha^*, \kappa^2 \right) - 1 \right], \quad (2.55)$$

where sn is the Jacobi elliptic function. This form for the potential is rather complicated and does not lend itself to a general exact solution.

Analytic progress can still be made by looking at the limiting behavior of the potential (and the continuum equation). For surfaces near the O-point, $\kappa \rightarrow 0$, the expressions for \hat{x} and V simplify considerably:

$$\lim_{\kappa \rightarrow 0} \hat{x} = \kappa \cos n_0 \alpha^*, \quad (2.56)$$

$$\lim_{\kappa \rightarrow 0} V = \lim_{\kappa \rightarrow 0} \frac{\hat{x}''}{\hat{x}} = -n_0^2. \quad (2.57)$$

At the O-point the continuum equation, Eq. (2.53), simplifies using this limiting V :

$$\frac{d^2 f}{d\alpha^{*2}} = - \left(\frac{\hat{\omega}^2}{\Omega^2} + n_0^2 \right) f. \quad (2.58)$$

This is now a Schrödinger equation with constant potential, which of course has the known solutions,

$$f_1 = \sin \left[\sqrt{\frac{\hat{\omega}^2}{\Omega^2} + n_0^2} \alpha^* \right], \quad (2.59)$$

$$f_2 = \cos \left[\sqrt{\frac{\hat{\omega}^2}{\Omega^2} + n_0^2} \alpha^* \right]. \quad (2.60)$$

Recalling that our actual solution is given by $Y = f(\alpha^*)/\hat{x}$ results in the following solutions at the O-point:

$$Y_1 \sim \sin \left[\sqrt{\frac{\hat{\omega}^2}{\Omega^2} + n_0^2 \alpha^*} \right] / \cos n_0 \alpha^*, \quad (2.61)$$

$$Y_2 \sim \cos \left[\sqrt{\frac{\hat{\omega}^2}{\Omega^2} + n_0^2 \alpha^*} \right] / \cos n_0 \alpha^*. \quad (2.62)$$

Next, in order to determine the eigenmodes and frequencies, the boundary conditions on Y must be imposed. The 2π -periodic boundary conditions in α^* were given in Sec. 2.3 in Eqs. (2.32) and (2.33). In order to satisfy periodicity, the following must be enforced:

$$\sqrt{\frac{\hat{\omega}^2}{\Omega^2} + n_0^2} = j, \quad (2.63)$$

where j is an integer. To avoid singularities in the solution caused by the $\cos n_0 \alpha^*$ in the denominator, j is further constrained to $j = n_0(j_{in} + 1)$. To ensure regular solutions, $j_{in} = 1, 3, 5, \dots$ correspond to odd modes and $j_{in} = 2, 4, 6, \dots$ correspond to even modes. The odd and even eigenmodes are therefore given by

$$Y_O^j = \frac{1}{\sqrt{\pi}} \frac{\sin [n_0(j_{in} + 1)\alpha^*]}{\cos n_0 \alpha^*}, \quad j_{in} = 1, 3, 5, \dots, \quad (2.64)$$

$$Y_E^j = \frac{1}{\sqrt{\pi}} \frac{\cos [n_0(j_{in} + 1)\alpha^*]}{\cos n_0 \alpha^*}, \quad j_{in} = 2, 4, 6, \dots \quad (2.65)$$

The normalization factor $\sqrt{\pi}$ comes from $\oint d\alpha^* \hat{x}^2 |Y|^2 = 1$.

The continuum frequencies at the O-point are obtained by combining the regularity condition $j = n_0(j_{in} + 1)$ with Eq. (2.63) and rearranging:

$$\frac{\hat{\omega}^2}{\epsilon^2} = \frac{n_0^2 j_{in} (j_{in} + 2)}{4}. \quad (2.66)$$

Here the limiting value of the rotational transform at the O-point, $\Omega \rightarrow \epsilon/2$, has been used. Eq. (2.66) agrees well with our second-order WKB approximated solution for the continuum at the O-point shown in Fig. 2.3.

2.6 Summary

The shear Alfvén continuum for an equilibrium with an island has been obtained using a WKB analysis. A finite upshift in the continuum accumulation point frequency has been demonstrated analytically for the first time for modes with the same helicity as the magnetic island ($l = 0$). This result confirms past numerical simulations by Biancalani et al that show an increase in this minimum frequency of the spectrum as well as a movement of the location of this frequency from the rational surface to the island separatrix [12]. Specifically, the WKB theory presented here predicts an upshift of the frequency to $\omega_{sep}^2 = \omega_{BAE}^2 + (q'_0 w)^2 \omega_A^2 / 32$ for a toroidal equilibrium with finite κ_s (where we have let $\omega^2 \rightarrow \omega^2 - \omega_{BAE}^2$ as described in Sec. 2.2). This frequency upshift also holds for a cylindrical equilibrium where $\omega_{BAE} = 0$. Parity restrictions on the continua inside the separatrix due to the boundary conditions were derived analytically; these restrictions were not treated properly in previous numerical work by Biancalani.

The properties of the spectrum and modes for $l \neq 0$ will be studied in the future. This study will be compared to the results of Biancalani for $l \neq 0$ [10, 11]. In particular, secondary resonances are expected at rational Ω surfaces where $l_0 - j_0 \Omega = 0$. Preliminary comparisons with observations on MST show that the AE frequencies from the experiments are consistent with modes that lie in the gap induced by the magnetic island. This will be the topic of Chapter 3. The majority of the work that was presented in this chapter has already been published [34].

Chapter 3

Comparison of theoretical continua to experimental observations

Alfvén activity has been observed in the Madison Symmetric Torus reversed-field pinch (RFP) experiment during neutral beam injection (NBI). Three different NBI-driven modes have been observed: $n = 5$, $n = 4$, and $n = -1$. The $n = 5$ mode has been identified as an energetic particle mode (EPM) and will not be discussed in great detail in this thesis. The $n = 4$ mode has been identified as an Alfvén Eigenmode (AE) due to its experimental scaling with the Alfvén velocity [4]. This $n = 4$ AE has not been characterized as a specific type up until now, and will be the subject of much of the rest of this dissertation. The $n = -1$ mode has not been experimentally identified as an AE or EPM (or anything else), and will be discussed in Chapter 6.

In the EAST, FTU, and TEXTOR tokamaks, beta-induced Alfvén eigenmode (BAE) activity has been observed in the presence of a magnetic island [6]. The BAE frequency appears to be intricately linked to the tearing mode amplitude (island width). The implications of the island Alfvén continua theory from Chapter 2 for EAST and FTU will be discussed towards the end of this chapter.

3.1 Background on the Madison Symmetric Torus (MST)

MST is an axisymmetric RFP device with a close-fitting conducting shell. MST has a major radius of $R_0 = 1.5$ m and a minor radius of $a = 0.5$ m. Typically, plasma currents in MST are in the range of 200 – 500 kA [35]. This section describes the MST configuration and the neutral beam injector; it borrows heavily from Jon Koler's thesis [36].

Parameter	Range
I_p	200 – 600 kA
B_ϕ on axis	0.2 – 0.55 T
q_0 on axis	0.167 – 0.23
q_a on edge	–0.15 – 0.01
$\langle n_e \rangle$	$0.3 \times 10^{19} - 1.6 \times 10^{19}/m^3$
T_e	0.1 – 2 keV
Discharge duration	30 – 75 ms

Table 3.1 MST parameters

3.1.1 Geometry and equilibrium features

MST is a relatively simple geometry to study because the aspect ratio of $R_0/a = 3$ makes it amenable to a cylindrical approximation. Toroidal effects are relatively weak on MST, due to the safety factor $q < 1$. In addition, the circular cross section removes much of the coupling due to the strong shaping present in tokamaks. The operating parameters for MST are presented in Table 3.1.

In this dissertation, MST will be studied in the non-reversed configuration. In a non-reversed equilibrium the reversal surface where $B_\phi = 0$ is located at the edge ($F = 0$). This forces the safety factor q to zero at the edge as well. See Fig. 3.1 for the q profile and magnetic field for this configuration. The q profile is small in RFPs and monotonically decreases with radius. Note that the safety factor passes through the $1/5$ surface in the plasma core.

3.1.2 Neutral beam injection

A 1 MW neutral beam injector (NBI) is installed on MST [37], which is used to heat the core ions. The NBI can fire hydrogen or deuterium beams at energies up to 25 keV; this works out to beam velocities of 2.2×10^6 m/s for hydrogen and 1.6×10^6 m/s for deuterium beams. The beam is injected at an angle tangential to the core magnetic field; see Fig. 3.2 for a schematic of the beam view. The hydrogen or deuterium neutral particles injected by the NBI are ionized through collisions sustained along their path through the plasma core. The pulse length of the beam lasts

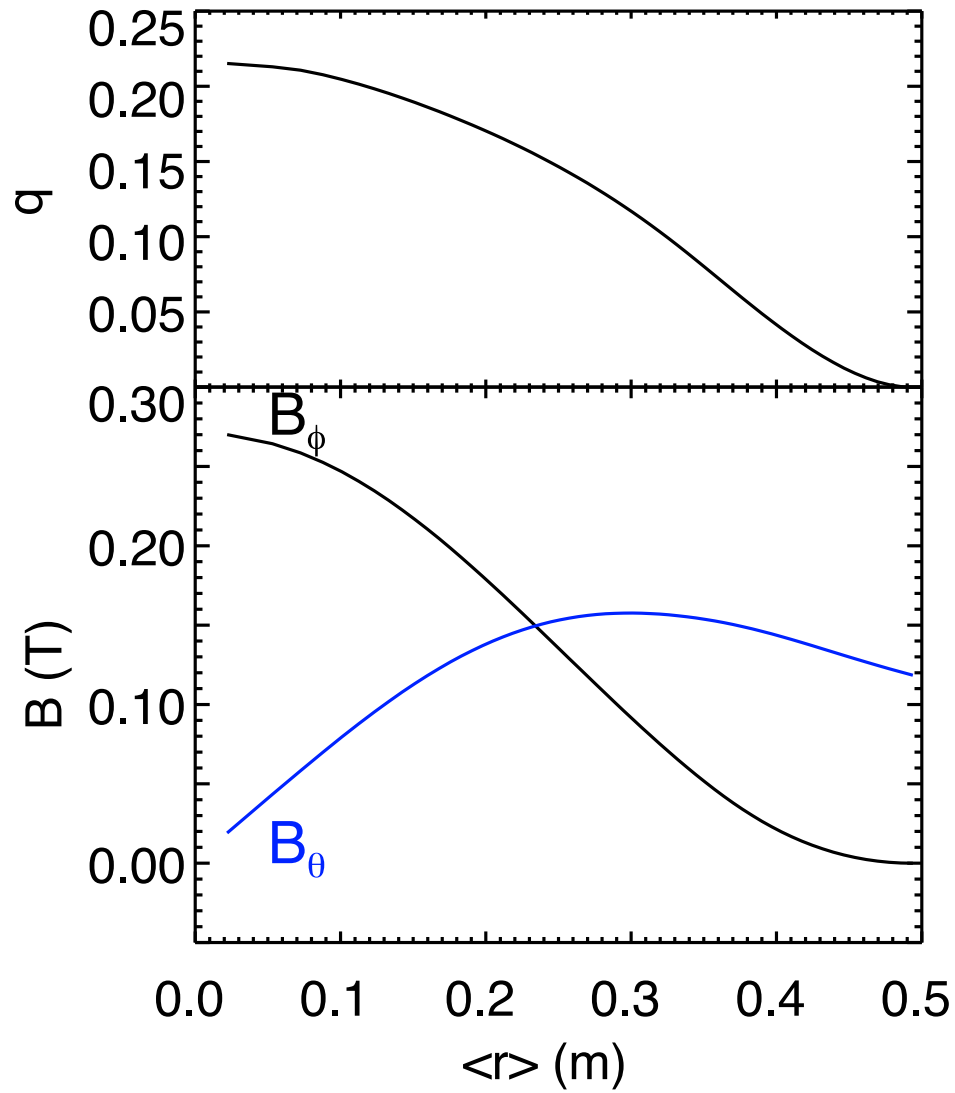


Figure 3.1 Safety factor and magnetic field profiles for a non-reversed MST configuration. Both the safety factor and the toroidal magnetic field B_ϕ go to zero at the edge. Figure courtesy of Jay Anderson, adapted from Kollner's thesis.

for 5 to 20 ms. This allows the beam to be turned on and off during a typical shot on MST, which lasts about 30 to 75 ms. The beam drive can be considered an equilibrium feature for an analysis of Alfvén waves during tearing mode activity, since both the Alfvén timescale $\tau_A = 1/k_{\parallel}v_A \sim 1\mu s$ and the $n = 5$ island toroidal rotation timescale $\tau_{tear} = 1/f_{tear} \sim 250\mu s$ are much shorter than the beam duration $\tau_A \ll \tau_{tear} \ll \tau_{beam}$.

The use of neutral beam injection (NBI) and the concomitant fast ion population serves as a destabilizing drive for energetic particle modes (EPMs) and Alfvén eigenmodes (AEs). Fig. 3.3 shows the fast ion density distribution in v_{\parallel} and radius along with the Alfvén speed v_A . Much of the core fast ion population is resonant with the Alfvén speed, allowing the energetic particles to potentially drive AEs to instability.

3.1.3 Alfvénic activity during NBI

Alfvénic activity has been studied in NBI-heated plasmas in MST in the non-reversed configuration [4]. In the non-reversed configuration, the reversal surface with $B_{\phi} = 0$ is locked at the plasma edge. By scanning the plasma current from $I_p \approx 200$ kA to $I_p \approx 500$ kA, the core \mathbf{B} field can be adjusted. Modifying the magnetic field results in a change in the Alfvén speed, $v_A = B/\sqrt{\rho}$. A detailed scan in observed burst frequency vs. core Alfvén speed was performed by Kolerer (see Kolerer’s thesis). The Alfvénic frequency activity (~ 100 kHz and up) on MST is measured through the use of 32 B_{θ} signals from the toroidal array of magnetic coils and 8 B_{θ} and B_{ϕ} signals from the poloidal array of coils. The results of the study for deuterium, hydrogen, and helium plasmas are presented in Fig. 3.4. These frequencies have all been Doppler corrected for the tearing mode frequency of 10 – 30 kHz for MST.

The $n = 5$ bursts do not show a strong scaling with the Alfvén velocity. They have been shown to be energetic particle modes (EPMs) that scale with the NBI beam velocity [4]. The $n = 4$ burst frequencies exhibit a strong scaling with core Alfvén speed and thus have been determined to be AEs. In addition to scanning the core \mathbf{B} field to modify v_A , the Alfvén speed can also be changed by adjusting the mass density $\rho = m_i n_i$ experimentally in two ways. First, the ion number density n_i can be tweaked; second, the experiment can be run with a different plasma species, giving a

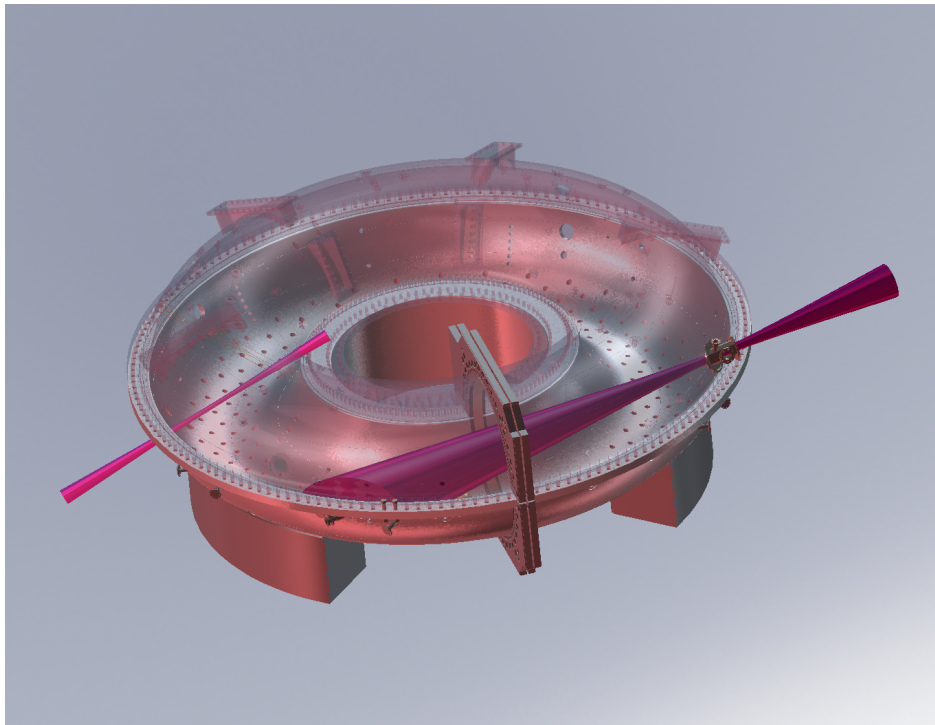


Figure 3.2 Schematic view of the neutral beam injector installed on MST. The beam passes through the core tangential to the toroidal magnetic field. The smaller radial beam is the diagnostic neutral beam, which is not discussed in this paper. Figure courtesy of Steve Oliva.

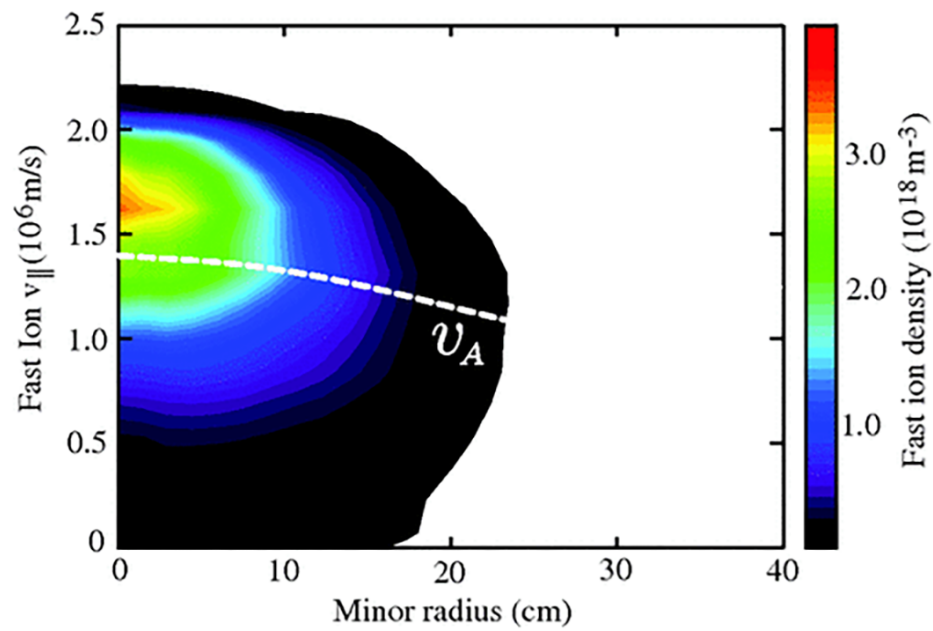


Figure 3.3 Fast ion density as a function of v_{\parallel} and radius in MST. This plot was calculated using the TRANSP code for plasmas with $n_i = 0.7 \times 10^{19}/m^3$. The Alfvén speed v_A is plotted vs. radius, and much of the core fast ion population is resonant with the Alfvén wave. Figure from Kollner, 2012 PRL [4].

different ion mass m_i . While deuterium ($m_i = 2m_p$) is used for most of the shots, hydrogen ($m_i = m_p$) is used to probe the high Alfvén speed regime, and helium ($m_i = 4m_p$) is used to probe the low Alfvén speed regime.

3.2 Investigation of $n = 4$ Alfvén bursting modes on MST

Since the $n = 4$ activity on MST has been shown to be Alfvénic, the question naturally turns to characterizing the type of AE. Simulations are generally used to study the Alfvén continuum and mode structure. As a first step for any computation of the Alfvén continua and modes, an equilibrium model is needed. Generally the next step is to compute the continuum for the equilibrium using an ideal MHD code that solves for radially-singular solutions to the shear Alfvén equations. The Alfvén continuum is studied for frequency gaps, which indicate frequency ranges to search for discrete Alfvén eigenmodes. Finally, these AEs are found and analyzed (if present) using a generalized eigenvalue matrix solver that includes coupling across flux surfaces, allowing for global, non-singular solutions. These codes for discrete modes generally solve equations based on a reduced MHD formulation.

For the MST configuration under consideration here, Koliner has studied the Alfvén spectrum numerically using the VMEC and STELLGAP codes [36]. These codes are all discussed in detail in Chapter 4. The Variational Moments Equilibrium Code (VMC), developed by S. P. Hirshman [38, 39], is used to solve for the equilibrium. VMC is a three-dimensional ideal MHD equilibrium code that solves for equilibria with closed nested flux surfaces. The VMC code will be discussed in detail in Sec. 4.2. Once a VMC solution for MST is found, the equilibrium is used as an input to the STELLGAP code to compute the shear Alfvén continuum [40]. STELLGAP was developed by D. A. Spong, and will output the Alfvén continuum frequencies as a function of flux throughout the domain.

For the MST case considered here, we are interested in understanding the nature of the $n = 4$ AE bursts. A canonical case from experiment is core $v_A \approx 1.5 \times 10^6$ m/s and Alfvén burst frequencies of $f \approx 130$ kHz. Koliner studied this non-reversed configuration numerically using VMC and STELLGAP [4]. The q -profile from VMC and the continuum frequencies from

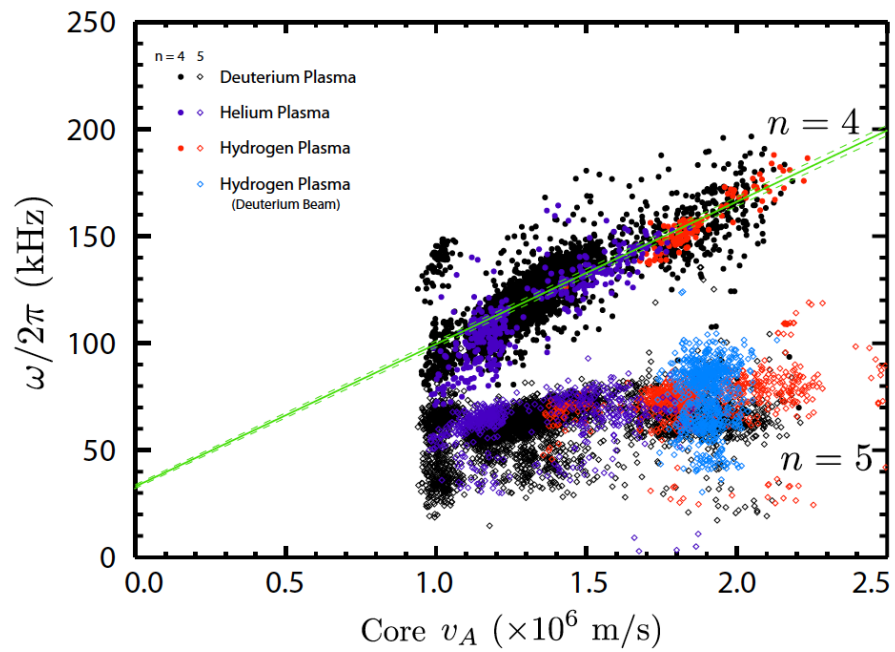


Figure 3.4 $n = 4$ and $n = 5$ MST burst frequency data vs. Alfvén speed. Note that the $n = 5$ bursts exhibit weak scaling with v_A , while the $n = 4$ bursts are clearly Alfvénic in nature. Figure from Koller's thesis.

STELLGAP are presented in Fig. 3.5. An $n = 4$ toroidicity-induced Alfvén eigenmode (TAE) frequency gap is present in the computed continuum from $f \approx 210$ kHz to $f \approx 300$ kHz. This gap range is much higher than the observed frequency of 130 kHz. Therefore we can conclude that the Alfvén activity observed on MST is not a TAE mode.

Since the TAE gap is too high to explain the observations, another possibility is the beta-induced Alfvén eigenmode (BAE) gap, which exists at low frequencies. A version of STELLGAP exists that includes acoustic couplings to lowest order [41]. D. A. Spong has run STELLGAP simulations that use the slow-sound approximation to include the fluid’s compressional response to the Alfvén wave in order to study the BAE gap for this case (unpublished, presented in 2013 ISHW invited talk). In Fig. 3.6, the acoustic coupling pulls the $n = 5$ continuum branch out of resonance at the $q = 1/5$ surface and gives a gap frequency upshift of $f_{BAE} = 24$ kHz. This gap is much lower than the observed mode frequency of 130 kHz. Thus the Alfvénic activity on MST is neither a TAE nor a BAE.

3.3 Effects of $n_0 = 5$ island on MST continuum

It is important to note that the model used by Kollner described in Sec. 3.2 assumed nested, topologically toroidal flux surfaces. This assumption is built into the VMEC code. Returning to Fig. 3.5, the $n = 5$ continuum is in resonance at the $q = 1/5$ surface where the branch frequency goes to zero. This low-order rational surface in the core of MST is unstable to tearing modes, and an island forms when finite resistivity is included [42].

Experimentally, MST has measured a sizable core island in this configuration using Thomson scattering fluctuations correlated with edge-measured magnetic amplitudes [43, 44, 45]. The mode numbers of the island are $m_0 = 1$, $n_0 = 5$, consistent with the q -profile passing through $1/5$, and a half-width of about 7 cm. Because this island in the core was neglected in the VMEC/STELLGAP simulations discussed in Sec. 3.2, it is natural to consider the following two questions: 1) How does the presence of this large island affect both the Alfvén continuum and discrete modes in MST? 2) Could the island create a gap that the observed AEs live in?

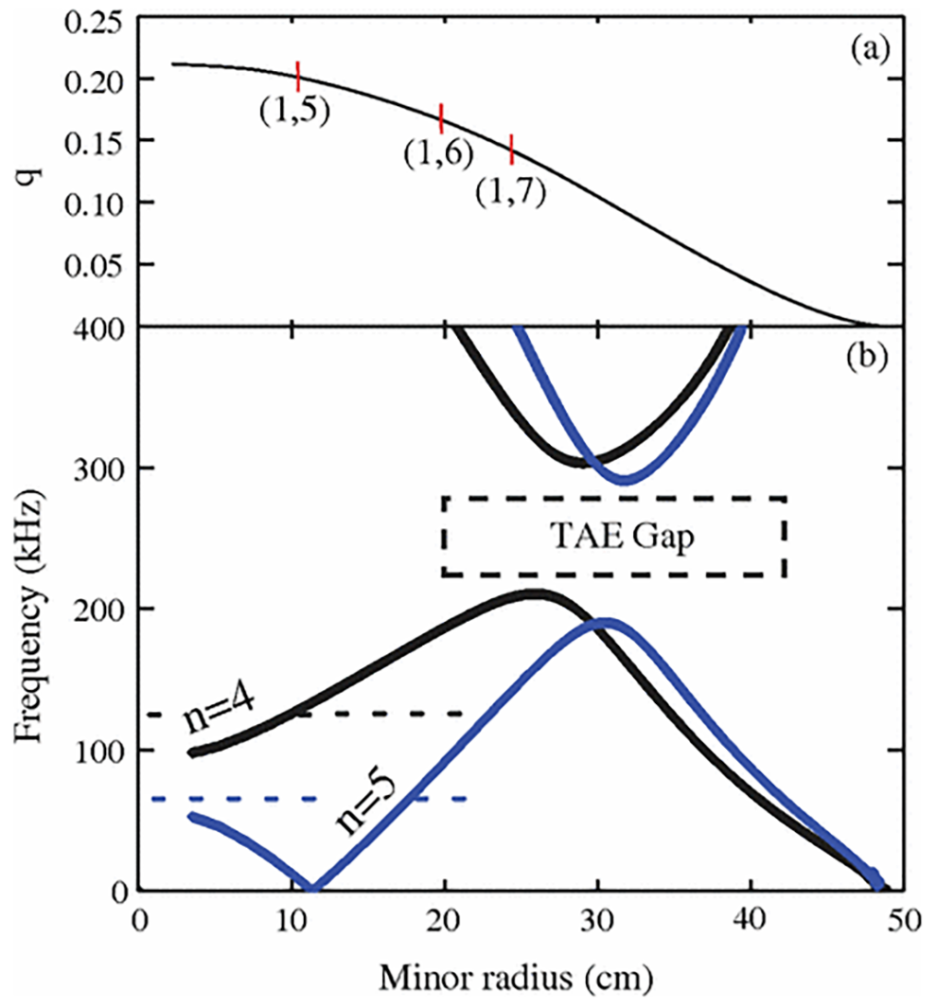


Figure 3.5 Top plot: safety factor q computed with VMEC for the non-reversed MST configuration. Bottom plot: shear Alfvén continuum frequencies from STELLGAP. A sizable TAE gap is predicted in the 200 – 300 kHz range. The gap is too high to explain the observations of an AE at ~ 130 kHz. Figure from Koliner, 2012 PRL [4].

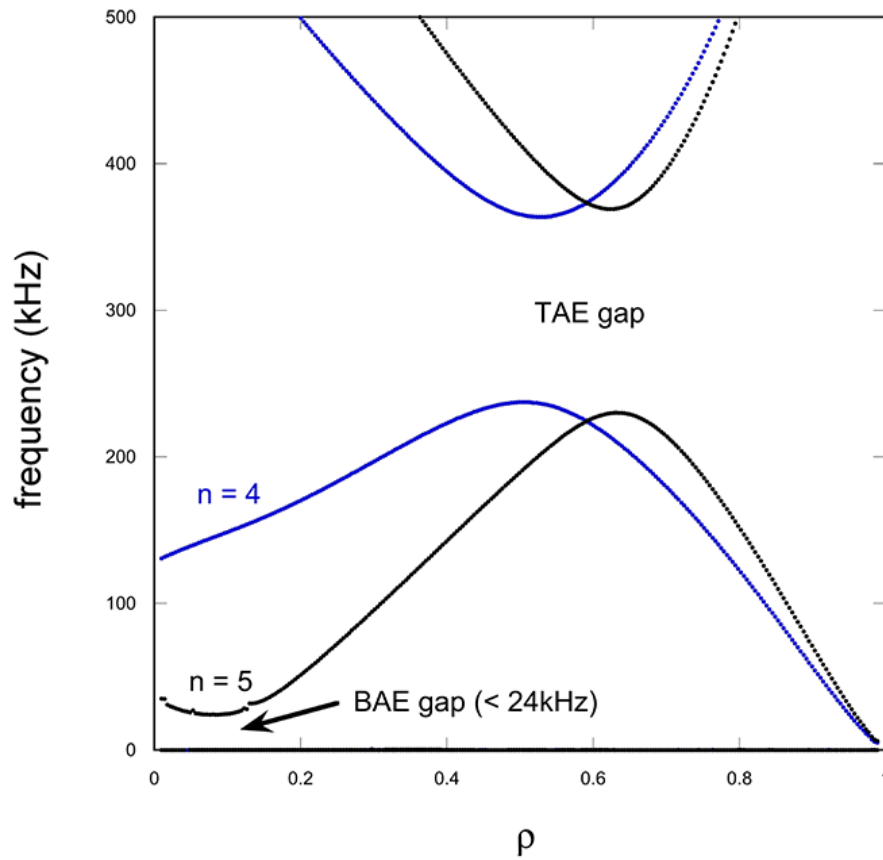


Figure 3.6 A STELLGAP simulation of the continua in MST with finite beta effects included through the slow-sound approximation. The BAE gap can be seen below 24 kHz. Figure courtesy of Don Spong.

The Alfvén continuum in the presence of an island was investigated analytically in Chapter 2. In order to compare this theory to the MST experimental observations, a brief discussion on mode numbers is needed. Experimentally (and in the absence of an island), the poloidal harmonic m and the toroidal harmonic n are used as good quantum numbers in the sense that the linear operator commutes with the rotation operator. The quantities of interest can be expanded in a Fourier series in these harmonics; here we are interested in the shear Alfvén displacement:

$$\xi_s = \sum_{m,n} \xi_{m,n} e^{i(m\theta - n\zeta)}. \quad (3.1)$$

Once an island is formed, these m, n numbers are no longer the best quantum numbers to use for the magnetic surfaces inside the island. Instead the j_{in} and l numbers from the theory presented in Chapter 2 should be used, with the displacement expanded as

$$\xi_s = \sum_{j_{in}, l} \xi_{j_{in}, l} e^{i(l\chi - j_{in}\alpha^*)}. \quad (3.2)$$

However, when an island is present, experimental observations will still measure the poloidal and toroidal mode numbers m and n , since these are what can be measured by the various diagnostics on the machine. Each mode still has a dominant m component, which is what is measured and used here.

Because both experiments and the VMEC coordinates (presented in Chapter 4) used for the numerical simulations in this dissertation use m and n , while the analytic theory from Chapter 2 uses j_{in} and l , it would be useful to have a simple mapping between the two sets of numbers. The problem is that one set of quantum numbers does not easily translate into the other. This is simply because the island numbers serve as a good set of quantum numbers inside the island where the poloidal/toroidal harmonics do not work. Similarly, the dominant poloidal/toroidal harmonics are used far outside the island or when no island is present, where the island numbers do not work. It is possible, however, to gain a rough understanding of the mapping between the two sets of numbers by considering a j_{in}, l mode and an m, n mode in the core of the island. In this way, we can gain an understanding of what j_{in} and l correspond to a given m and n .

It is useful to relate an m, n mode to an h, l mode, where h is the mode number for the α coordinate. Then we will relate h back to j_{in} , the α^* quantum number we actually want. The

relationship between the cylindrical and island modes for an island in a cylinder is

$$\xi_s \sim e^{i(m\theta - n\zeta)} = e^{i(l\chi - hn_0\alpha)}, \quad (3.3)$$

$$m\theta - n\zeta = l\chi - hn_0\alpha. \quad (3.4)$$

Recall from Sec. 2.1 that $\chi = \theta$ and $\alpha = \zeta - q_0\theta$. Substituting these relations gives $m\theta - n\zeta = (l + m_0h)\theta - n_0h\zeta$, which allows a mapping between the mode numbers given by

$$m = l + m_0h, \quad (3.5)$$

$$n = n_0h. \quad (3.6)$$

This relationship is exact, but is in α space; what we actually want is the relation to α^* space with quantum number j_{in} . To convert to this other set of quantum numbers, the relationship will no longer be exact. The rough map from j_{in} to h can be determined by considering a small island embedded in a global equilibrium. On a global scale, the island is localized to a resonant flux surface. From a global view, the h number valid on the original rational surface would correspond to $j_{in} \approx 2h$ on a flux surface just inside the separatrix. This doubling in quantum number is due to the doubling in periodicity which occurs when crossing from a surface just outside the separatrix to a surface just inside the separatrix. Using $j_{in} \approx 2h$ in Eqs. (3.5) and (3.6) results in the following approximate conversions between island mode numbers j_{in} and l and global mode numbers m and n :

$$j_{in} \approx \frac{2}{n_0}n, \quad (3.7)$$

$$l \approx m - \frac{m_0}{n_0}n. \quad (3.8)$$

For MST, the island has mode numbers $m_0 = 1$ and $n_0 = 5$. The Fourier modes observed experimentally and found numerically (treated later on in this dissertation) are $m = 1, n = 4$ and $m = 0, n = -1$. With Eqs. (3.7) and (3.8), these can be related back to approximate j_{in} and l from the continuum theory. Recalling that $j_{in} = 1, 2, 3, \dots$ and $l = 0, 1, 2, \dots$, an $m = 1, n = 4$ mode corresponds to $j_{in} \approx 2$ and $l \approx 0$, and an $m = 0, n = -1$ mode corresponds to $j_{in} \approx 1$ and $l \approx 0$. This mapping will be useful throughout this thesis. Additionally, since the theory in

Chapter 2 was developed for $l = 0$, this shows that the lowest continuum branch from theory with $j_{in} = 1$ roughly corresponds to $m = 0, n = -1$, and the second lowest branch ($j_{in} = 2$) roughly corresponds to $m = 1, n = 4$ for the MST equilibrium.

In Sec. 2.5, the continuum frequencies at the O-point (or core) of the island was derived analytically, resulting in Eq. (2.66):

$$\frac{\hat{\omega}^2}{\epsilon^2} = \frac{n_0^2 j_{in} (j_{in} + 2)}{4}. \quad (2.66)$$

This equation can be rewritten in a form more amenable to experimental parameters, recalling that $\hat{\omega}^2 = (\omega^2 - \omega_{BAE}^2)/\omega_A^2$. Writing in terms of frequency and using $f_A = k_{\parallel} v_A$ one arrives at

$$f = \sqrt{f_{BAE}^2 + \frac{n_0^2 j_{in} (j_{in} + 2)}{4} \epsilon^2 k_{\parallel}^2 v_A^2}, \quad (3.9)$$

where $k_{\parallel} = 1/(q_0 2\pi R_0)$. For MST, the relevant parameters are $n_0 = 5$, $q_0 = 1/5$, $R_0 = 1.5$ m, $k_{\parallel} = 0.53/\text{m}$, $f_{BAE} = 24$ kHz, $w/2 = 7$ cm, $q'_0 = .004/\text{cm}$, and $\epsilon = q'_0 w/2 = .028$. These parameters come from private correspondence with Jay Anderson as well as Jon Koller [4]. When these parameters are used in Eq. (3.9), the resulting continuum frequencies as a function of Alfvén speed for $j_{in} = 1$ and $j_{in} = 2$ are plotted in Fig. 3.7. The continuum frequencies converge to the same BAE accumulation point frequency in the limit of $v_A \rightarrow 0$. As the Alfvén speed increases, the continuum branches spread into a wide gap. The burst frequencies measured on MST are also plotted for deuterium, helium, and hydrogen plasmas. As mentioned previously, the experimental data has been Doppler shifted to correct for the 10 – 30 kHz tearing mode rotation frequency on MST. The Doppler correction is pulled from a database for each shot. Experimental data is available in the range of $v_A \sim 1 \times 10^6$ to $\sim 2.5 \times 10^6$ m/s. At the time of writing, about 430 new bursts have been included in this plot thanks to recent analysis by John Boguski and Ruiyang Feng. The burst data lies inside of the envelope formed from the $j_{in} = 1$ and $j_{in} = 2$ continuum branches from theory. Thus, the experimental observations are consistent with an $n = 4$ Alfvén eigenmode existing in the frequency gap induced in the core of the $n_0 = 5$ island. Notice that the frequency gap width between the two continuum branches increases with increasing v_A . This gap is named here the Island-induced Alfvén Eigenmode (IAE) gap, since the island creates this

gap in the continuous spectrum. The scaling of the gap between the continuum branches in the island according to Eq. (3.9) predicts that the $n = 4$ AE frequencies on MST should scale with the island width. Experiments are underway on MST to measure the $n = 4$ mode frequency at various different island sizes. The island width can be modified by pulling the q -profile down and bringing the $1/5$ resonant surface closer to the magnetic axis. The “pressure” from the circular axis causes the island to squeeze to a smaller size as it is dragged towards the center of the plasma.

For the regime of interest from experiment, the continuum branches in the island from theory are very insensitive to the BAE frequency used. In Fig. 3.8, Eq. (3.9) has been plotted for $j_{in} = 1$ and $j_{in} = 2$ with and without the BAE frequency upshift, f_{BAE} . The upshift results in very small corrections to the continua in the 1×10^6 to 2×10^6 m/s range in which experimental observations are available. Thus the inclusion of f_{BAE} in Eq. (3.9) is not necessary to capture the IAE gap for MST.

The continua in the core of the island do have a strong dependence on the normalized island half-width $\epsilon = q'_0 w/2$. The continuum branches scale up and down in frequency with ϵ , and the gap width Δf also scales with ϵ . A larger island width increases the continuum frequencies and also increases the gap between the branches. Fig. 3.9 shows the behavior of the frequencies in the island core at three different island widths. An expression for the gap size in terms of ϵ and the Alfvén speed can be derived by comparing the $j_{in} = 1$ and $j_{in} = 2$ branches:

$$\Delta f = \left(\sqrt{2} - \frac{\sqrt{3}}{2} \right) n_0 k_{\parallel} \epsilon v_A. \quad (3.10)$$

Here the simplification $f_{BAE} = 0$ has been used as discussed above; the approximation barely affects the result. This gap width scaling with ϵ suggests that an island width threshold may exist, below which no Alfvénic activity would occur. At sufficiently small ϵ , the IAE frequency gap may be too small to support an Alfvén mode, as continuum damping could prevent the instability from growing. Preliminary experimental results from MST appear to support this conclusion. Comparing Fig. 3.9 to Fig. 3.7 suggests a possible explanation for the burst data that lies outside of the continuum envelope. If the equilibrium has evolved to a significantly larger or smaller magnetic island size during a shot, then the burst frequency may lie outside the continua which

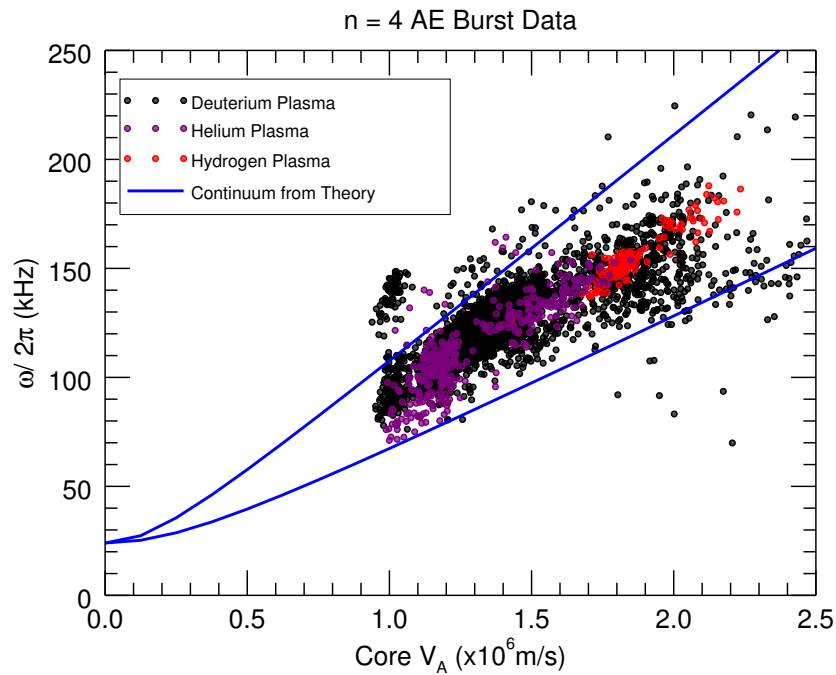


Figure 3.7 The theoretical continuum frequencies at the island O-point for $j_{in} = 1$ and $j_{in} = 2$ plotted along with observed Doppler-corrected Alfvénic burst data from MST experiment. The continuum branches provide an envelope for the AE bursts throughout. New data courtesy of John Boguski and Ruiyang Feng.

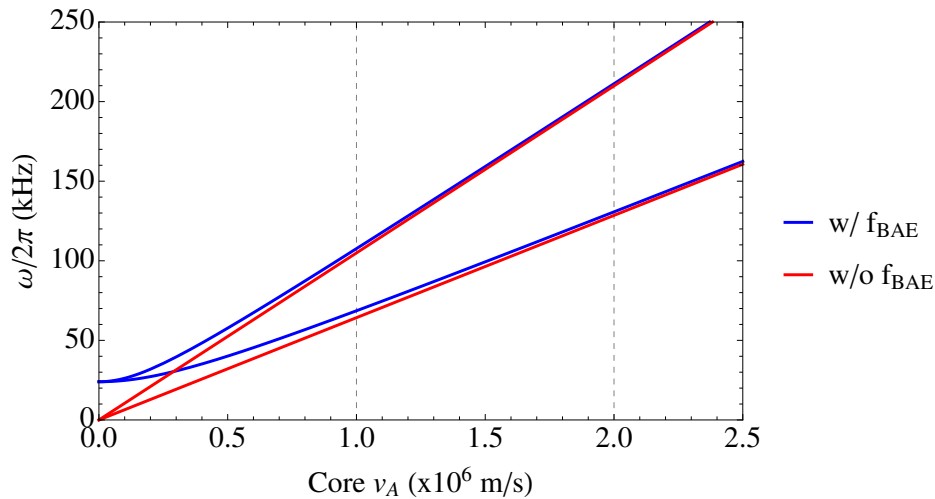


Figure 3.8 The theoretical continuum frequencies at the island O-point for $j_{in} = 1$ and $j_{in} = 2$ plotted with BAE frequency upshift in blue and without upshift in red. The BAE upshift is not very significant in the region with experimental observations, from $\sim 1 \times 10^6$ to $\sim 2 \times 10^6$ m/s.

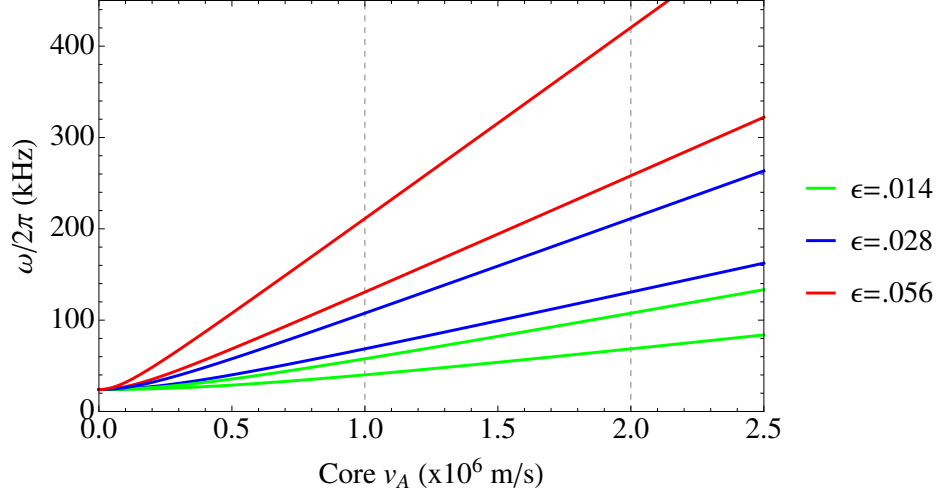


Figure 3.9 The theoretical continuum frequencies at the island O-point for $j_{in} = 1$ and $j_{in} = 2$ for three different values of $\epsilon = q'_0 w/2$. The frequencies of the continuum branches as well as the size of the gap scales with the island width, ϵ .

are computed assuming a fixed island size of $\epsilon = .028$. A larger island shifts both the continua and allowed burst frequencies higher, and a smaller island shifts the continua and allowed burst frequencies lower.

3.4 Island-modified BAE modes in MST vs. tokamaks

In addition to the helically-coupled gap in the core of the island already discussed in this chapter, there is another type of gap affected by an island. Recall from Sec. 2.2 that the beta-induced Alfvén eigenmode (BAE) continuum accumulation point frequency ω_{BAE} occurs at the rational surface in the absence of an island. For ω_{BAE} to be nonzero, geodesic curvature and finite pressure effects must be included through the slow sound approximation $\gamma p/\rho\omega^2 R_0^2 \ll 1$ to retain the compressional response of the fluid to the shear Alfvén waves. When an island is present, we have shown that the BAE accumulation frequency is upshifted, and the new minimum is located at the separatrix. The upshifted BAE frequency at the separatrix is given by

$$\omega_{sep}^2 = \omega_{BAE}^2 + (q'_0 w)^2 \omega_A^2 / 32. \quad (3.11)$$

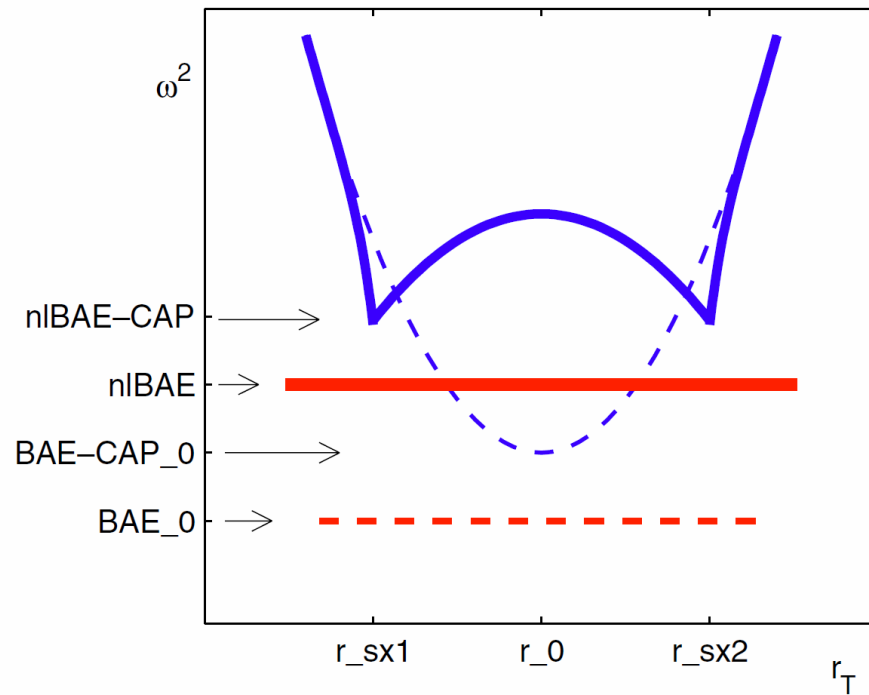


Figure 3.10 Schematic showing the modified Alfvén continuum due to a magnetic island. The continuum and discrete frequencies are shown with dashed lines in the absence of an island and solid lines when an island is present. The frequency is plotted vs. minor radius, so the separatrix is counted twice. Figure from Biancalani, 2011 PPCF [12].

Fig. 3.10 shows a schematic of the frequency upshift effect from the island. When no island is present, the minimum frequency ω_{BAE} is located at the resonant surface; the continuum in this case is shown with a dashed blue curve. A discrete BAE mode could only exist at a frequency below this minimum, as illustrated by the dashed red line. When an island is present the minimum frequency is increased, and the location of the minimum is moved to the separatrix, as shown with the solid blue curve. This higher minimum allows BAEs to potentially exist at a higher frequency without experiencing continuum damping, as demonstrated with the solid red line.

3.4.1 BAE frequency upshift on MST

Beneath the BAE continuum frequency (often called the BAE gap), a discrete BAE mode can resonant and can be driven unstable by energetic particles. Since the island leads to an upshift in the BAE continuum frequency, there is a larger BAE gap frequency range for a BAE to occupy. For MST, the BAE upshift correction is found to be quite small. Eq. (3.11) can be rewritten in a form that is easier to compare to experiment:

$$f_{sep} = \sqrt{f_{BAE}^2 + \frac{(\epsilon k_{\parallel} v_A)^2}{8}}. \quad (3.12)$$

Here k_{\parallel} is measured in m^{-1} and recall that $\epsilon = q'_0 w/2$. This allows us to use the standard MST parameters introduced in this chapter: $\epsilon = .028$, $k_{\parallel} = .53/m$, and $v_A = 1.75 \times 10^6 m/s$. From the finite-beta STELLGAP simulation in Fig. 3.6, the BAE frequency in the absence of an island is $f_{BAE} = 24$ kHz. Using these values in Eq. (3.12) gives a minimum frequency at the separatrix of $f_{sep} = 25.7$ kHz. The magnetic island thus gives a small correction of about 7% to the BAE minimum frequency in MST. No Alfvénic modes have been identified below the 25 kHz range on MST, so no BAE activity has been observed.

3.4.2 BAEs on the EAST tokamak

In tokamaks, a much larger upshift to the BAE continuum frequency from a magnetic island is found. In MST, the very small shear ($q'_0 = .004/cm$) in the core of the plasma where the island is located leads to a very small $\epsilon = q'_0 w/2$ of $\epsilon = .028$ and thus a small correction to the BAE

Device	ϵ	f_{BAE}	f_{sep}	Correction
EAST	.125	17 kHz	21.3 kHz	25%
MST	.028	24 kHz	25.7 kHz	7%

Table 3.2 A comparison of the continuum upshifts due to an island in EAST and MST.

frequency. Tokamaks tend to have a much larger value for the magnetic shear q'_0 at the rational surface compared to MST. The EAST tokamak is a good example. EAST contains tearing mode activity at a $q_0 = 2/1$ surface; the shear at this location is approximately $q'_0 = .05 /cm$ (see Fig. 3.11, plot a)), leading to $\epsilon = .125$ for a 5 cm island [6]. This ϵ for EAST is over 4 times larger than the value for MST, so the BAE upshift correction is expected to be much higher.

EAST has a major radius of 1.7 m, toroidal field $B_T = 1.8$ T, and generally runs with deuterium plasmas at densities of $n_i \sim 2 \times 10^{19}/m^3$. With these operating conditions, the parallel wavelength and Alfvén speed are $k_{\parallel} = .047m^{-1}$ and $v_A = 6.2 \times 10^6 m/s$. The BAE minimum continuum frequency has been calculated by Xu in the absence of an island [6]. Xu used the following equation derived from an asymptotic solution to the generalized fishbone-like dispersion relation (GFLDR) developed by Zonca [46]:

$$f_{BAE} = \frac{1}{\sqrt{2m_i\pi R_0}} \sqrt{T_e + \frac{7}{4}T_i}. \quad (3.13)$$

Using experimental parameters, Xu calculates this to be $f_{BAE} = 17$ kHz. In EAST, the upshifted BAE frequency at the separatrix due to an island from Eq. (3.12) is $f_{sep} = 21.3$ kHz. This is a much larger correction than that seen for MST; the island upshifts the frequency by about 25% in EAST. A comparison of the continuum upshifts for MST and EAST is shown in Table 3.2.

This island-induced BAE frequency upshift has not been taken into account before for EAST, and it helps explain some experimental observations. The discrete BAE frequencies measured on EAST should lie below the minimum BAE continuum frequency, but the observed mode frequencies of 14 – 18 kHz are very close to and even touch and cross over the BAE continuum frequency computed with no island in Eq. (3.13). Fig. 3.11, plot b) shows this phenomenon. Using the island-upshifted continuum frequency of $f_{sep} = 21.3$ kHz computed here shows that the observed

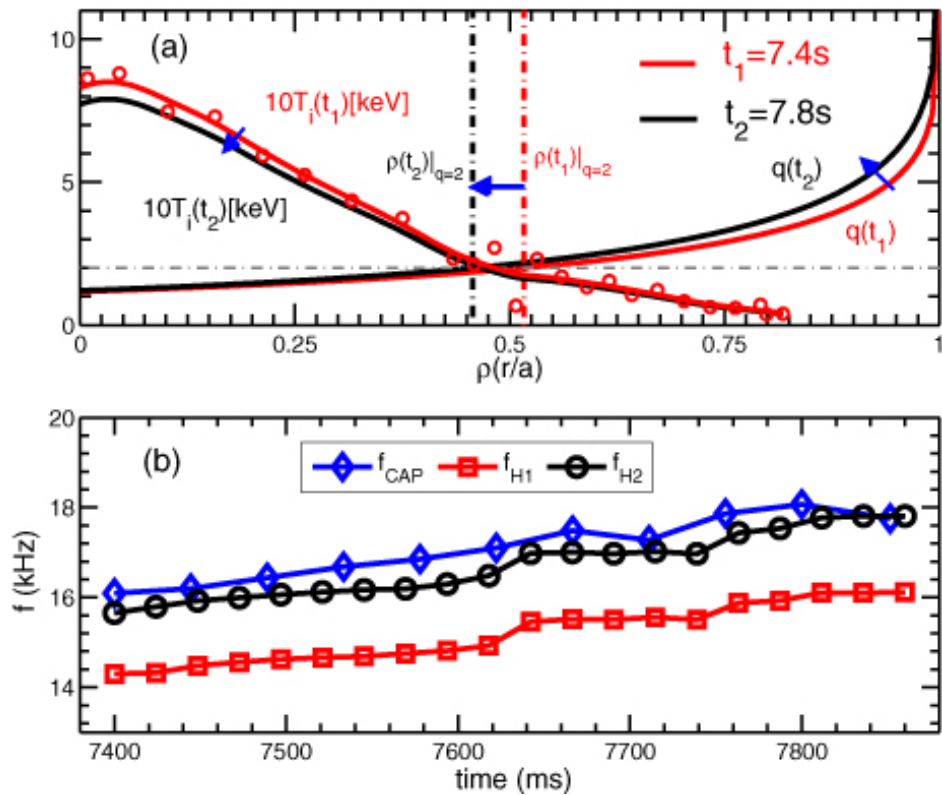


Figure 3.11 Experimental data from EAST tokamak. a) Safety factor profile and ion temperature at two different times during the shot. b) Observed BAE mode frequencies (labeled f_{H1} and f_{H2}) and theoretical BAE continuum accumulation point frequency f_{BAE} from Eq. (3.13) (labeled here f_{CAP}). Figure from Xu, 2013 PPCF [6].

modes can be identified as BAE modes living below the island-upshifted minimum continuum frequency. These modes are consistent with a modified version of the BAE named here the IBAE for Island-upshifted Beta-induced Alfvén Eigenmode. The mode is still a BAE in character, but can exist at a higher frequency without damping on the continuum thanks to the increased continuum accumulation point frequency caused from the island.

3.4.3 BAEs on the FTU tokamak

As further evidence of the validity of the island-induced BAE frequency upshift, experiments on the Frascati Tokamak Upgrade (FTU) during strong tearing mode activity have observed BAE mode frequencies that scale roughly linearly with the island width, as measured through poloidal magnetic fluctuations [47]. Fig. 3.12 displays the measured $n = -1$ BAE frequencies vs. the tearing mode amplitude measured through poloidal magnetic fluctuations. The scaling of these observed modes with island width is consistent with modes residing in an island-upshifted BAE gap given by Eq. (3.12) derived in this thesis.

The shear at the resonant surface in tokamaks including EAST and FTU is generally significantly larger than the tiny shear at the $q = 1/5$ surface in the core of MST. This higher shear makes the island's effects on the low-frequency BAE gap significantly greater in tokamaks than that which is seen on MST (and RFPs in general with a core-localized island). BAE activity is thus expected to be more intricately linked to magnetic island growth in tokamaks compared to RFPs, as can be seen in the literature [6, 8, 47].

3.5 Summary

The $n = 4$ Alfvénic burst activity on MST has been shown to be consistent with a gap mode residing in the core of the $n_0 = 5$ magnetic island. The AE burst frequencies obtained from an experimental scan in the core Alfvén speed v_A lie in the gap in the core of the island obtained from the continuum theory presented in Chapter 2. The $j_{in} = 1$ and $j_{in} = 2$ continuum branches sandwich the burst data as expected for an island-induced Alfvén eigenmode. This $n = 4$ AE will be investigated numerically in the subsequent chapters.

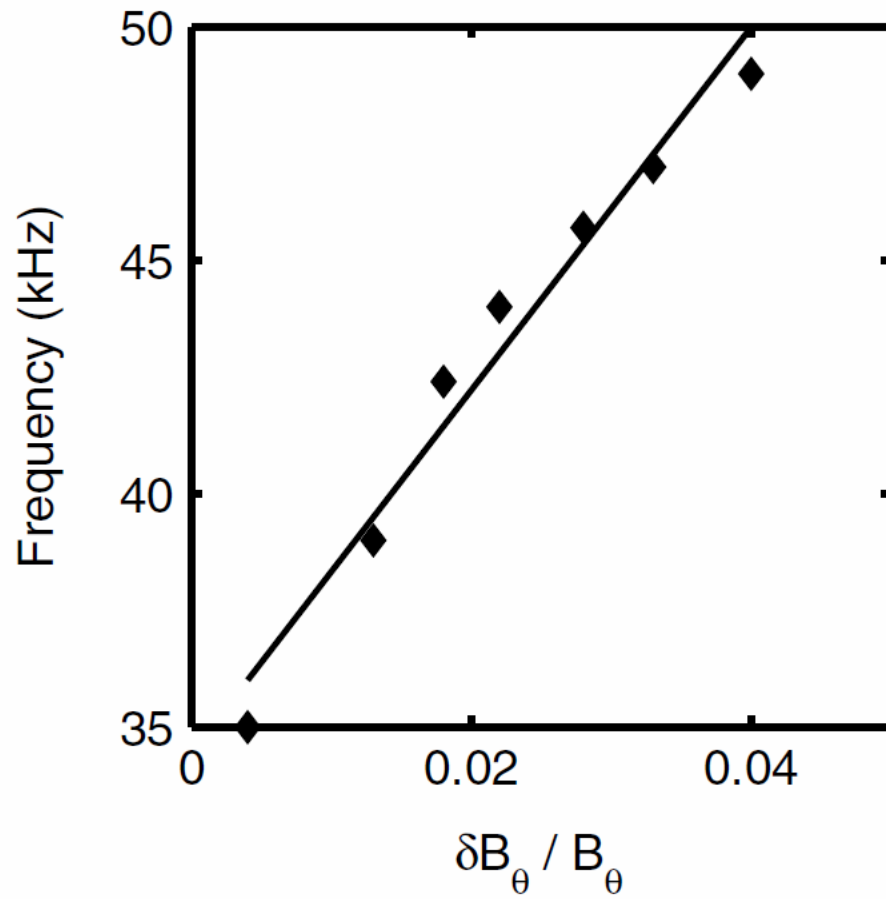


Figure 3.12 Experimental BAE frequencies measured on the FTU tokamak vs. tearing mode amplitude measured as magnetic fluctuations. The BAE frequencies scale strongly with the magnetic island width. Figure from Buratti, 2005 Nucl. Fusion [47].

A magnetic island is shown to cause a larger BAE frequency upshift in tokamaks compared to MST. The larger upshift arises from the significantly larger shear q'_0 (and thus ϵ) present in tokamaks. The island-modified BAE continuum frequency explains observed BAE mode activity on EAST and FTU.

Chapter 4

Numerical investigation of Alfvén eigenmodes on MST

In Chapter 3, we showed that the $n = 4$ Alfvénic bursting activity observed on MST is consistent with a discrete shear Alfvén mode living in the island-induced gap predicted by the analytic theory of the continua. We will now strive to confirm this hypothesis using two types of numerical investigations. In this chapter, the STELLGAP code is used to compute the Alfvén continuum which can be compared to the theoretical spectrum for MST discussed in Chapter 3. Second, AE3D is used to search for discrete Alfvén eigenmodes. Prior to discussing either of these codes, a numerical model approximating an MST equilibrium with an island is needed.

4.1 Modeling MST with an island as a SHAx state

It is known experimentally that a large $n_0 = 5$ island is present in the non-reversed MST configuration. Recall that the safety factor in Fig. 3.5 passes through $q = 1/5$ in the core. An equilibrium code called VMEC was used by Jon Kollerer to model MST. The VMEC equilibrium code assumes closed, nested flux surfaces and thus can only model a single magnetic axis. Due to the restriction of a single axis, one of two approximations has to be made when modeling the MST configuration with a core $1/5$ island. First, the island can be neglected as was done by Kollerer [4], yielding an axisymmetric equilibrium. As was shown in Sec. 3.2, this model did not yield Alfvén continua consistent with Alfvén burst frequencies from experiment. Second, the axisymmetric circular magnetic axis can be neglected resulting in magnetic surfaces that vary smoothly from a helical axis out to circular flux surfaces at the plasma edge. In the parlance of the RFP world, this is known as a Single Helical Axis (SHAx) state.

We will now investigate this second approximation, where we simplify the equilibrium containing a circular and helical axis (island) into a SHAx state. There is considerable motivation for doing so: the continuum theory in Sec. 2.4 showed that the frequency branches inside of the island all converge to a continuum accumulation point at the separatrix. Since the frequencies all drop close to zero at the separatrix, this effectively localizes any modes present to the island core, where it is free of continuum damping. In order to extend out to the separatrix and beyond, a mode would couple to the accumulating continua and stabilize. Since all of the action of the Alfvén mode takes place in the core of the island, this is the area of the equilibrium that must be accurately modeled. In a SHAx state approximation, the helical core axis approximates the axis of the island, and thus the equilibrium features of the island core should be captured. The island separatrix and accompanying topology change is not included in this model, but should not be crucial for obtaining the qualitative features of AEs inside the island.

The canonical MST case to be considered here contains deuterium plasmas with a current of $I_p = 300$ kA and $n_i = 0.7 \times 10^{19} m^{-3}$ ion density. With this plasma current, the core magnetic field is $B = 0.3$ T. Using these parameters and $m_i = 2m_p$ for deuterium, the Alfvén speed is $v_A = B/\sqrt{\mu_0 m_i n_i} = 1.75 \times 10^6$ m/s. For this value of v_A , the experimental mode frequencies from Fig. 3.7 are in the 140 to 160 kHz range. We will use these frequencies to compare to numerical simulation results in this and upcoming chapters. The VMEC code will now be briefly introduced for modeling the MST equilibrium. Then the STELLGAP and AE3D codes will be discussed along with simulation results of the Alfvén continua and discrete modes.

4.2 The Variational Moments Equilibrium Code (VMEC)

The Variational Moments Equilibrium Code, VMEC, is an extremely useful code for computing three-dimensional plasma equilibrium. It is the workhorse equilibrium code for many stellarator simulations and reconstructions. VMEC obtains an equilibrium by using a variational method to find a minimum of the energy in the system [38, 39].

VMEC tries to find an equilibrium in MHD force balance,

$$\mathbf{F} = \mathbf{J} \times \mathbf{B} - \nabla p = 0, \quad (4.1)$$

while also enforcing Ampère's law and the divergence constraint:

$$\nabla \times \mathbf{B} = \mathbf{J}, \quad (4.2)$$

$$\nabla \cdot \mathbf{B} = 0. \quad (4.3)$$

To obtain this force balance, VMEC minimizes the total energy. The total plasma energy is given by

$$W = \int \left(\frac{B^2}{2} + \frac{p}{\gamma - 1} \right) dV, \quad (4.4)$$

where the first term is the magnetic energy, the second is the kinetic energy, and the integration is taken over the entire volume of the plasma.

In order to conserve magnetic flux, a contravariant representation of the \mathbf{B} field is utilized. When solving for RFP equilibria, the logical 'LRFP' is set to true in VMEC, allowing the code to run in terms of safety factor and poloidal flux. The magnetic field written in terms of poloidal flux, denoted here by ψ , is the following:

$$\mathbf{B} = \nabla \zeta \times \nabla \psi + q \nabla \psi \times \nabla \theta^*. \quad (4.5)$$

The poloidal-like angle θ^* used in VMEC is given by $\theta^* = \theta + \lambda(\psi, \theta, \zeta)$, with λ a poloidal stream-function used to make the field lines straight. This is done for numerical reasons; using λ to normalize the poloidal coordinate allows the Fourier series to be truncated at a finite number of harmonics. In VMEC, the coordinates are denoted by s , u , and v , where $s = \psi/\psi_{edge}$ is the normalized poloidal flux, $u = \theta$, and $v = \zeta$.

VMEC represents the magnetic flux surfaces using the following Fourier series:

$$R = \sum_{m,n} R_{m,n}(s) \cos(mu - nv), \quad (4.6)$$

$$Z = \sum_{m,n} Z_{m,n}(s) \sin(mu - nv), \quad (4.7)$$

$$\lambda = \sum_{m,n} \lambda_{m,n}(s) \sin(mu - nv). \quad (4.8)$$

During the energy minimization process, VMEC modifies the spectral components of the flux surfaces to find a lower energy state. Once a minimum of the energy is found, the configuration is in ideal MHD force balance and thus an equilibrium is obtained.

To initialize VMEC, the pressure profile, safety factor profile, and total enclosed magnetic flux ψ_{edge} are specified in an input file. In addition, information regarding the magnetic flux geometry of a starting configuration is needed. VMEC can be run in two modes: fixed boundary and free boundary. In free boundary runs, the simulation is initialized by specifying the location and currents in the external coils. In these simulations, the last closed flux surface is allowed to evolve. For fixed boundary simulations the $R_{m,n}$ and $Z_{m,n}$ Fourier components of the last closed flux surface are specified as inputs, and this plasma boundary remains unchanged throughout the energy minimization process in VMEC. In practice free boundary simulations are performed initially for a device's current coil configuration, and then the resulting outer flux surface is generally used as a starting point for future fixed boundary runs, which run much faster than the free boundary computations.

A 500 kA SHAx VMEC input file was available from MST. The input file is from a V3FIT reconstruction [48] which agrees well with experiment. In order to scale the profiles to 300 kA, the pressure profile was scaled down by a factor of .602 to match the total integrated pressure of the desired case. This factor is the ratio of total integrated pressure in the 300 kA case to the integrated pressure for the 500 kA case. The PHIEDGE parameter in VMEC for total enclosed magnetic flux has also been reduced, adjusting the total enclosed magnetic flux to the proper level for 300 kA plasmas. Running VMEC in fixed boundary mode, a well-converged VMEC equilibrium for the SHAx model of interest has been obtained. Three flux surfaces from the VMEC SHAx configuration are shown in Fig. 4.1. The surfaces transition smoothly from a helical core to circular, axisymmetric surfaces towards the edge. Using this equilibrium, the continuum and discrete modes can be studied with STELLGAP and AE3D, respectively.

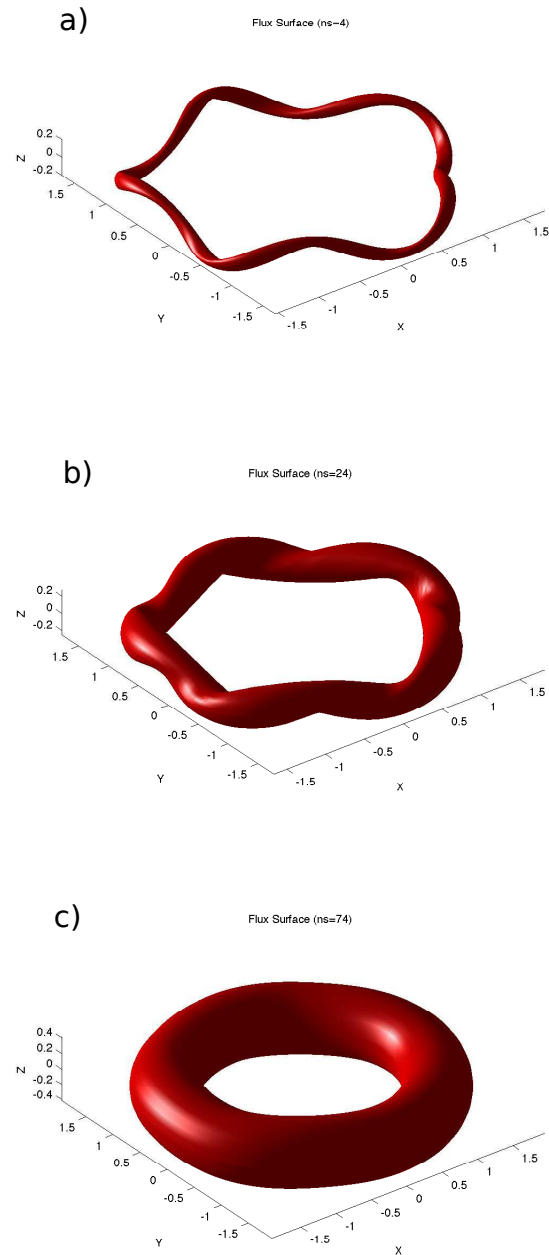


Figure 4.1 Three flux surfaces for an MST SHAx equilibrium from VMEC. a) A helical core flux surface near the axis. b) A surface in the region that transitions from helical to circular surfaces. c) A circular, axisymmetric surface near the plasma edge.

4.3 The STELLGAP continuum code

STELLGAP is a code written by Don Spong of Oak Ridge National Lab to compute the shear Alfvén continuum [40]. STELLGAP follows the theoretical framework set up by Salat and Tataronis [49, 50]. It requires a VMEC equilibrium as an input.

4.3.1 Model equations

The Alfvén continuum equation for incompressible waves (no $\xi_{||}$) in the low- β limit is

$$\rho_m \omega^2 \frac{|\nabla\psi|^2}{B^2} E_\psi + \mathbf{B} \cdot \nabla \left[\frac{|\nabla\psi|^2}{B^2} \mathbf{B} \cdot \nabla E_\psi \right] = 0, \quad (4.9)$$

where ψ is the poloidal flux and E_ψ is the covariant ψ component of the electric field. To avoid confusion with the normalized poloidal flux $\rho = \psi/\psi_{edge}$, the mass density is labeled as ρ_m . The first term provides the wave's inertia while the second-term provides a restoring force (tension) through field-line bending. Note that this is the same basic equation as Eq. (2.26) from Chapter 2, but in the absence of an island. This equation is valid for three-dimensional geometry, and no coupling to acoustic waves is present. In STELLGAP, Eq. (4.9) is solved using Boozer coordinates. Boozer coordinates are a special case of straight field-line coordinates, and as such offer a particularly simple representation for the parallel gradient operator, $\mathbf{B} \cdot \nabla$ [51, 52]. To obtain the Boozer coordinates required by STELLGAP, a VMEC equilibrium must first be run through the Boozer-Xform code before being passed to STELLGAP. Boozer-Xform had a problem handling the reversal surface in RFPs. This has been fixed by switching to poloidal flux and using q instead of the rotational transform ι (see Appendix E). In terms of Boozer coordinates, the following parallel gradient operator and $|\nabla\psi|^2$ can be used in Eq. (4.9):

$$\mathbf{B} \cdot \nabla = \frac{1}{\sqrt{g}} \left(\frac{1}{q} \frac{\partial}{\partial \theta} + \frac{\partial}{\partial \zeta} \right), \quad (4.10)$$

$$|\nabla\psi|^2 = g^{\rho\rho} \left(\frac{d\psi}{d\rho} \right)^2. \quad (4.11)$$

Here ρ is the normalized flux surface label, θ is the poloidal angle, ζ is the toroidal angle, and $g^{\rho\rho}$ is the contravariant $\rho\rho$ metric element.

Next, the electric field in Eq. (4.9) is expanded in a Fourier series:

$$E_\psi = \sum_{m,n} E_\psi^{m,n} \cos(m\theta - n\zeta). \quad (4.12)$$

Only the even (cos) parity of the electric field is required for devices with stellarator symmetry. After using these representations for $\mathbf{B} \cdot \nabla$, $|\nabla\psi|^2$, and E_ψ , Eq. (4.9) is multiplied by $\sqrt{g} \cos(m\theta - n\zeta)$ and flux surface averaged to give the symmetric generalized matrix eigenvalue equation,

$$\omega^2 \mathbf{A} \mathbf{x} = \mathbf{B} \mathbf{x}. \quad (4.13)$$

In this equation, $\mathbf{x} = [E_\psi^{m_1, n_1}, E_\psi^{m_2, n_2}, E_\psi^{m_3, n_3}, \dots]^T$ gives the continuum mode structure, ω^2 is the eigenfrequency, and \mathbf{A} and \mathbf{B} are both symmetric matrices. Within STELLGAP, Eq. (4.13) is solved using the DGEGV LAPACK subroutine from the IBM ESSL library.

The continuum equation assumes solutions with a non-square-integrable, singular radial structure. Thus Eq. (4.13) must be solved separately for each flux surface throughout the domain, resulting in a continuum of eigenfrequencies as a function of radius. No coupling across surfaces is included, so the matrices \mathbf{A} and \mathbf{B} are constructed for each surface. The included poloidal and toroidal mode numbers for the simulation can be specified with m_{max} and n_{max} , and range according to $0 \leq m \leq m_{max}$ and $-n_{max} \leq n \leq n_{max}$. The dominant m and n values are output along with frequency and radius, allowing the different continuum branches to be distinguished. In addition to the desired mode numbers, the ion density profile and ion mass is also specified in an input file to STELLGAP.

4.3.2 Computing the MST Alfvén continuum

The MST SHAx equilibrium from VMEC shown in Fig. 4.1 is used to initialize a STELLGAP simulation. Recall that the closed, nested flux surfaces vary smoothly from helical surfaces in the core to surfaces with a circular cross-section out towards the plasma edge. After running the VMEC coordinates through Boozer-Xform to obtain the Boozer coordinates needed by STELLGAP, the Alfvén continua are computed using STELLGAP's eigensolver routines.

The continuum frequencies vs. radius are plotted along with dominant n in Fig. 4.2 and dominant m in Fig. 4.3. In the core of the plasma where the surfaces are helical, a sizable frequency

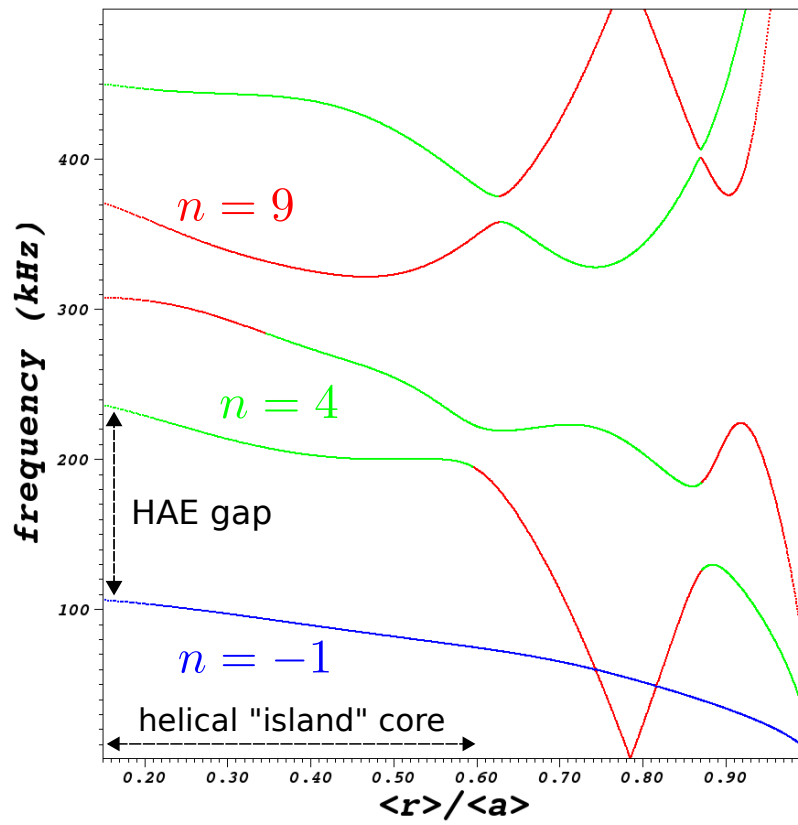


Figure 4.2 Shear Alfvén continuum in MST computed using STELLGAP. Dominant n toroidal mode number is color-coded. A helicity-induced Alfvén eigenmode (HAE) gap is present in the helical core with an $n = 4/n = -1$ coupling.

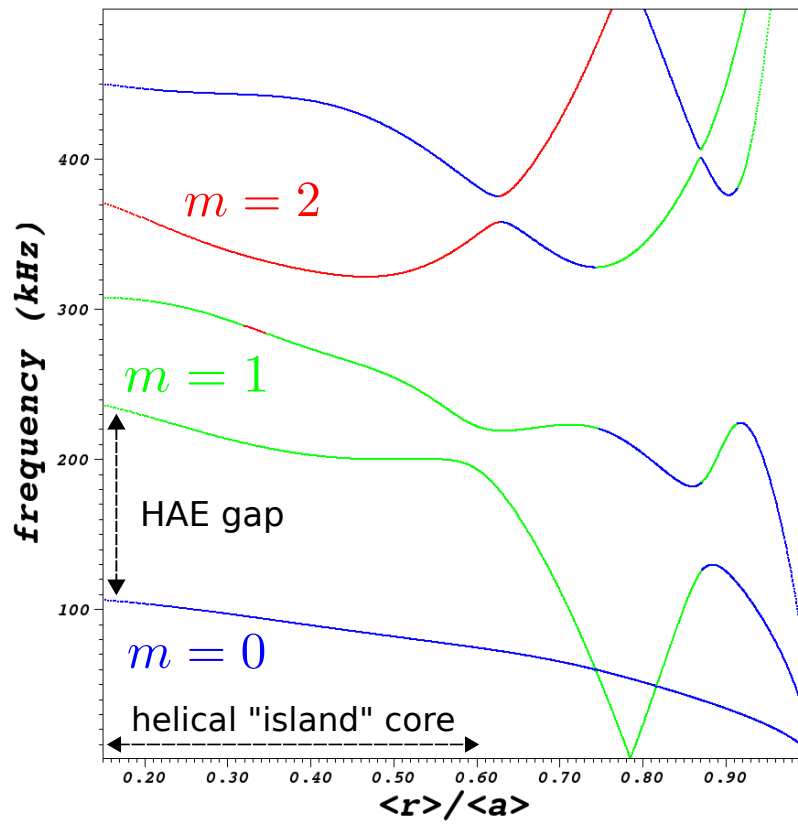


Figure 4.3 Shear Alfvén continuum in MST computed using STELLGAP. Dominant m poloidal mode number is color-coded. A helicity-induced Alfvén eigenmode (HAE) gap is present in the helical core with an $m = 1/m = 0$ coupling.

gap exists in the 110 to 230 kHz range. This continuum gap involves a helical coupling between $n = -1$ and $n = 4$ toroidal Fourier modes and $m = 0$ and $m = 1$ poloidal Fourier modes. A helicity-induced Alfvén eigenmode (HAE) gap exhibits the following general coupling [53]:

$$\delta n = n_2 - n_1 = n_0, \quad (4.14)$$

$$\delta m = m_2 - m_1 \geq 1. \quad (4.15)$$

Here n_0 is the toroidal mode number of the island; $n_0 = 5$ for MST. The gap is identified as with an HAE, since $\delta n = n_0 = 5$ and $\delta m = 1$ for this case. The frequencies of the $m = 0, n = -1$, and $m = 1, n = 4$ continuum branches in the helical core (the approximate $n_0 = 5$ island) can be compared to the island core continua frequencies from analytic theory for $j_{in} = 1$ and $j_{in} = 2$; recall that these numbers map to each other. From Fig. 3.7, the continuum frequencies from theory for $v_A = 1.75 \times 10^6$ m/s are 115 kHz for $j_{in} = 1$ and 185 kHz for $j_{in} = 2$, in reasonable agreement to 110 kHz and 230 kHz from STELLGAP, especially considering that VMEC/STELLGAP is using a SHAx approximation to the island. This gap frequency range of 110 – 230 kHz found numerically will now be used as a target frequency to search for global modes using the AE3D code.

Additional STELLGAP simulations have been performed for $I_p = 200$ kA and $I_p = 250$ kA in MST. The results are shown in Fig. 4.4. In the helical core, the continua appear to obey the v_A scaling of Eqs. (3.9) and (3.10) from the analytic theory for the island O-point frequencies and frequency gap in MST. Note that the HAE gap width scales with the plasma current, and the continuum branch frequencies also increase with increasing $I_p \sim B \sim v_A$.

STELLGAP serves as a useful code not only for computing the continuum, but also for identifying frequency and radius ranges in which to search for eigenmodes using the AE3D code. AE3D allows the user to specify a frequency range for the calculations, and frequencies in a continuum gap from a STELLGAP simulation generally provide an excellent starting point.

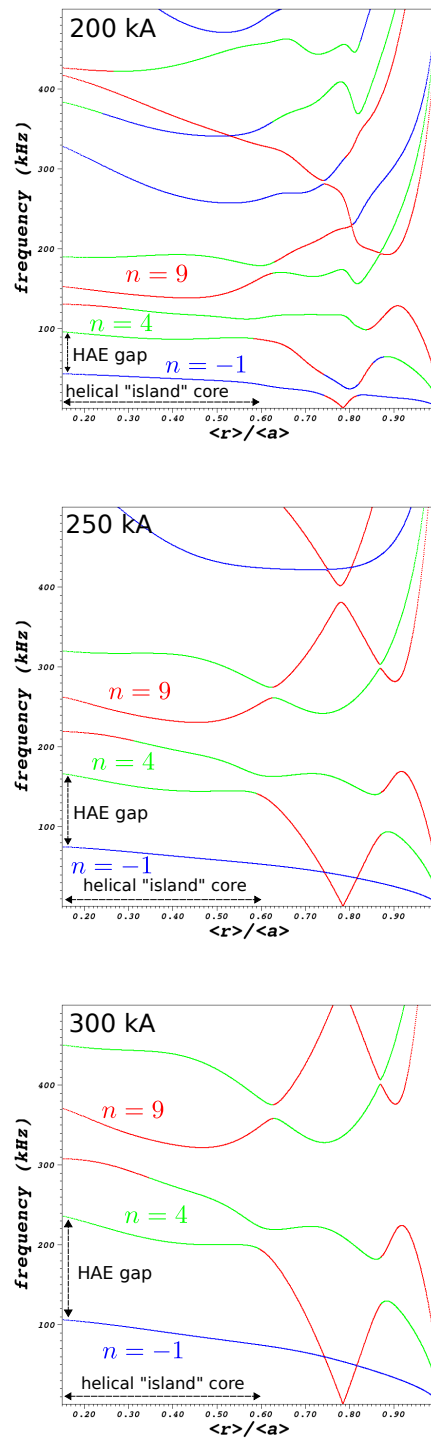


Figure 4.4 Shear Alfvén continua in MST computed using STELLGAP for $I_p = 200, 250,$ and 300 kA. The HAE gap frequencies and width increase with I_p , and thus v_A .

4.4 The AE3D code for calculating Alfvén modes

The calculation of discrete AEs with radial extent is significantly more complicated than computing continuum modes. A reduced MHD formulation in the low- β limit is employed to allow for the finite radial extent of discrete Alfvén eigenmodes in AE3D. AE3D was written by Don Spong to calculate Alfvén eigenmodes [5]. Following the reduced MHD equations of Kruger, Hegna, and Callen [22], AE3D computes modes of finite radial extent along with their eigenfrequencies.

4.4.1 Model equations

The basic model equations are the vorticity equation and the ideal Ohm's law:

$$\nabla \cdot \left[\frac{\rho_m}{B} \frac{d}{dt} \left(\frac{\nabla \phi}{B} \right) \right] = \mathbf{B} \cdot \nabla \frac{\delta J_{\parallel}}{B} + \delta \mathbf{B} \cdot \nabla \frac{J_{\parallel}}{B}, \quad (4.16)$$

$$\frac{\partial \delta \psi}{\partial t} = \frac{1}{B} \mathbf{B} \cdot \nabla \phi. \quad (4.17)$$

Here the perturbed quantities are denoted with a δ , and the remaining are equilibrium quantities. The electrostatic potential is ϕ ; $\delta \psi$ is the perturbed poloidal magnetic flux.

The perturbed parallel current and perturbed magnetic field can be written in terms of $\delta \psi$ as

$$\delta J_{\parallel} = \nabla^2 \delta \psi, \quad (4.18)$$

$$\delta \mathbf{B} = \nabla \zeta \times \nabla \delta \psi. \quad (4.19)$$

Using the ideal Ohm's law Eq. (4.17) in Eqs. (4.18) and (4.19), and substituting these back into Eq. (4.16) gives the following eigenvalue equation:

$$\omega^2 \nabla \cdot \left(\frac{1}{v_A^2} \nabla \phi \right) + \mathbf{B} \cdot \nabla \left[\frac{1}{B} \nabla^2 \left(\frac{\mathbf{B}}{B} \cdot \nabla \phi \right) \right] + \nabla \zeta \times \nabla \left(\frac{\mathbf{B}}{B} \cdot \nabla \phi \right) \cdot \nabla \frac{J_{\parallel}}{B} = 0. \quad (4.20)$$

Here ϕ and all of the perturbed quantities are assumed to vary in time as $e^{-i\omega t}$. AE3D solves this equation for ϕ , the electrostatic potential eigenmodes. This equation is similar to Eq. (4.9), with the first term providing the inertia and the second term the field-line bending. Since modes are not restricted to a singular radial structure, a third ballooning term is also present in this formulation.

Next, Eq. (4.20) is multiplied by a trial function $\tilde{\phi}$ and integrated over the plasma volume. The resulting equation is solved using a Galerkin approach, where ϕ and $\tilde{\phi}$ are expanded in a

finite element (in radius) and Fourier series (in poloidal/toroidal angles) representation. Churning through this process results in a generalized matrix eigenvalue equation:

$$\mathbf{F}\mathbf{y} = \omega^2\mathbf{G}\mathbf{y}, \quad (4.21)$$

where \mathbf{F} and \mathbf{G} are block tridiagonal matrices. The eigenvector is

$\mathbf{y} = [\phi_{\rho_1}^{m_1, n_1}, \phi_{\rho_1}^{m_2, n_2}, \dots, \phi_{\rho_2}^{m_1, n_1}, \phi_{\rho_2}^{m_2, n_2}, \dots]^T$, a column vector of the Fourier components of the potential for each flux surface. AE3D solves for the Alfvén eigenmode potentials \mathbf{y} and the eigenfrequencies ω^2 using several different solvers that are selectable by the user, including LAPACK/DGGEV and JDQZ. JDQZ uses a Jacobi-Davidson QZ algorithm written by G. Sleijpen and H. van der Vorst, which allows very fast, efficient solution of Eq. (4.21) by pre-specifying a target frequency (eigenvalue) on which to center the eigenmode search. Instead of computing all the eigenvalues, JDQZ computes just a subset, allowing for much faster run times. The target frequency is generally chosen to be a gap frequency of interest from STELLGAP simulations.

The surface displacement ξ_s used in the analytic theory of Chapter 2, the electric field E_ψ used in STELLGAP, and the potential ϕ used by AE3D are all closely related to one another. The potential and E_ψ are related in the normal manner, through $\mathbf{E} = -\nabla\phi$. Here \mathbf{E} , E_ψ , ϕ , and ξ_s are all perturbed wave quantities. In terms of the flux coordinates ψ , θ , and ζ , this relation is

$$\mathbf{E} = -\left(\frac{\partial\phi}{\partial\psi}\nabla\psi + \frac{\partial\phi}{\partial\theta}\nabla\theta + \frac{\partial\phi}{\partial\zeta}\nabla\zeta\right). \quad (4.22)$$

By inspection, $E_\psi = -\partial\phi/\partial\psi$. The plasma displacement and electric field are related through the ideal MHD Ohm's law,

$$\mathbf{E} = -\frac{\partial\xi}{\partial t} \times \mathbf{B}. \quad (4.23)$$

Assuming the quantities have a $e^{-i\omega t}$ time dependence and looking at the covariant- ψ component gives $E_\psi = i\omega\xi_s$ (recall that $\xi_s = \boldsymbol{\xi} \cdot (\mathbf{B} \times \nabla\psi)/|\nabla\psi|^2$). Thus the relationship between the three different representations of the eigenmodes is the following:

$$E_\psi \sim -\frac{\partial\phi}{\partial\psi} \sim i\omega\xi_s. \quad (4.24)$$

It should be noted that AE3D is also capable of computing the continuum modes localized to a single flux surface. Fig. 4.5 shows an example of a continuum mode computed with AE3D.

The radial structure appears as an approximation to a singularity (the sign of the singularity does not matter). In this case the mode is an $m = 1$, $n = 6$ continuum mode localized to a surface at $\sqrt{\psi} = 0.72$. These singular modes can be computed much more quickly and efficiently by the STELLGAP code, but also are found with AE3D as delta function solutions along with the global solutions. This continuum mode structure is in stark contrast to the Alfvén eigenmodes of finite radial extent computed with AE3D, as shown in Fig. 4.6, which will be discussed shortly. By scanning the modes output by AE3D, the global AEs vs. the continuum modes can be identified.

4.4.2 Computing Alfvén eigenmodes in MST

An extensive search for Alfvén modes in MST has been conducted using the AE3D code. Using the JDQZ solver in AE3D, a scan in the range of 0 to 300 kHz has been performed. For the parameters of interest with $v_A = 1.75 \times 10^6$ m/s, a discrete Helicity-induced Alfvén Eigenmode (HAE) has been found within the HAE continuum gap frequency range found with STELLGAP. The structure of the mode is presented in Fig. 4.6. The AE is localized to the core of the helical plasma, as expected for our SHAx proxy to the island. The eigenfrequency was found to be 149 kHz, consistent with the 140 to 160 kHz range in which Alfvén bursts have been observed experimentally. The HAE frequency lies in the center of the 110 – 230 kHz HAE gap from STELLGAP, as well as the 115 – 185 kHz gap in the island core from theory. The structure of the HAE is dominated by the $m = 1$, $n = 4$ Fourier component, but also has a significant $m = 0$, $n = -1$ contribution. This agrees with the $\delta n = 5$, $\delta m \geq 1$ coupling expected from the continuum gap. Experimentally, the $n = 4$ Alfvén burst is measured to have an $m = 1$ poloidal structure. In addition, the $n = 4$ bursts are generally observed along with $m = 0$, $n = -1$ activity in MST [54]; this will be discussed in greater detail in Chapter 6.

AE3D has also been used to find the discrete modes for the $I_p = 200$ kA and 250 kA cases. The continua for these two configurations were studied in Sec. 4.3.2. In both cases, AE3D computed a core-localized HAE mode dominated by the $m = 1$, $n = 4$ Fourier component. The eigenfunction for the HAE in the 200 kA case is shown in Fig. 4.7. The 200 kA HAE eigenfrequency is 90

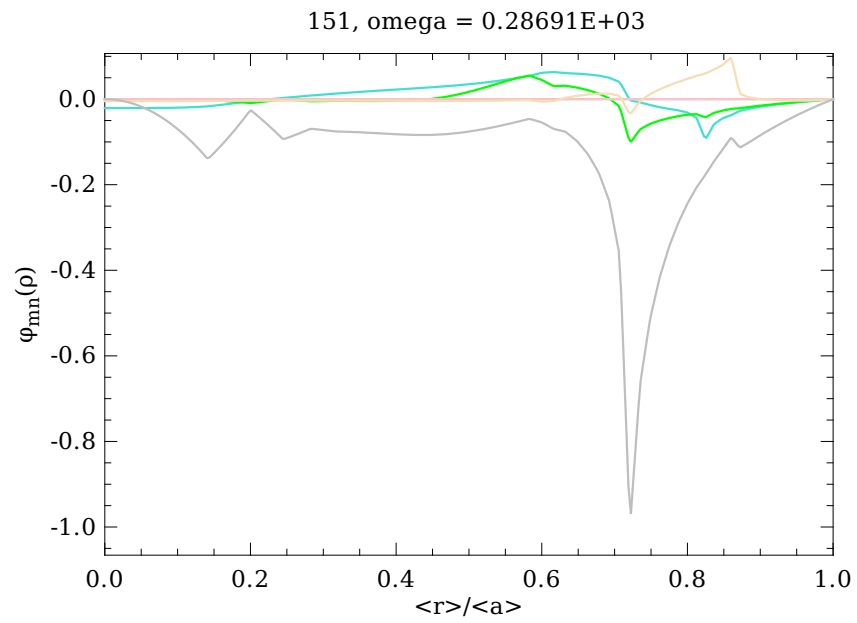


Figure 4.5 Shear Alfvén continuum mode computed with AE3D. The radial structure is singular at the flux surface on which the continuum mode resides, $\sqrt{\psi} = 0.72$ for this case. This $m = 1$, $n = 6$ continuum mode oscillates at 287 kHz.

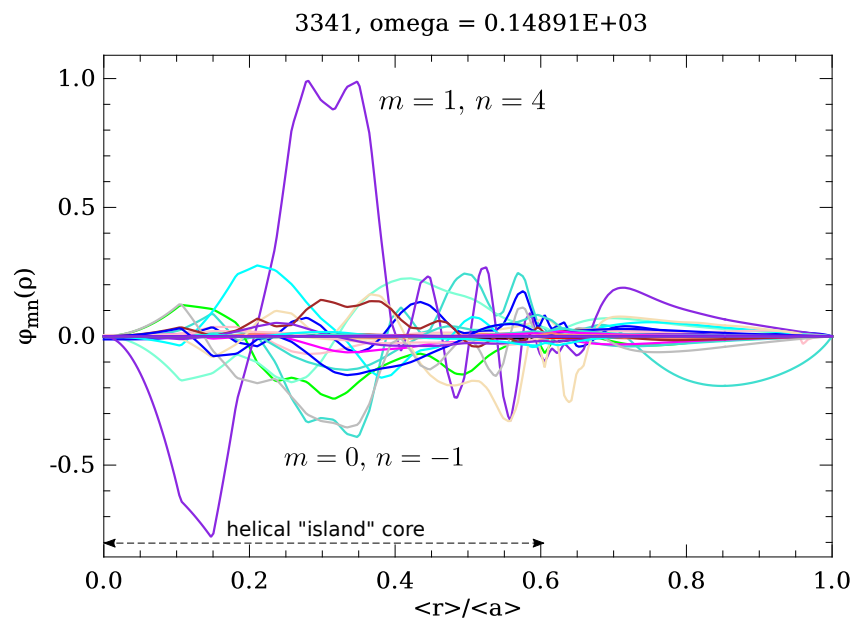


Figure 4.6 Helicity-induced Alfvén Eigenmode (HAE) in MST computed with the AE3D code.

The Fourier mode components of the electrostatic potential are plotted vs. $\sqrt{\psi}$. The mode is dominated by a coupling between the $m = 1, n = 4$ and $m = 0, n = -1$ Fourier components.

The AE is largely localized in the helical core. The frequency of the mode is 149 kHz, in agreement with 140 – 160 kHz from experiment.

kHz, lower as expected for this configuration. The frequencies of the modes scale with the plasma current since $v_A \sim B \sim I_p$, as expected from theory.

Eq.(3.9) from Chapter 3 for the continuum frequencies in the core of the island is

$$f = \sqrt{f_{BAE}^2 + \frac{n_0^2 j_{in} (j_{in} + 2)}{4} \epsilon^2 k_{\parallel}^2 v_A^2}; \quad (3.9)$$

this theory can be compared with the computed core HAE gap continuum frequencies from STELLGAP (from Sec. 4.3.2) and the discrete AE frequencies computed from AE3D. Fig. 4.8 shows the continuum theory curves for $j_{in} = 1$ and $j_{in} = 2$, along with STELLGAP-computed continuum frequencies and discrete Alfvén eigenmode frequencies computed with AE3D for $I_p = 200$ kA, 250 kA, and 300 kA.

The AE3D-computed mode frequencies lie in both the theory continuum gap and the continuum gap from STELLGAP for all three values of v_A tested. The theory and STELLGAP continua frequencies both exhibit positive scaling with the core Alfvén velocity, and both gaps increase as v_A increases. However, agreement is not perfect. Because STELLGAP uses a VMEC SHAx approximation to the actual equilibrium containing an island, the agreement with the island theory is not expected to be exact. The discrepancies between theory and STELLGAP are believed to stem from both the SHAx approximation, as well as the lack of mode localization. Specifically, the STELLGAP/VMEC simulations lack a separatrix to truly localize the mode activity within the island. In VMEC, the gradual transition from core helical flux surfaces to edge circular flux surfaces does not include a separatrix, and thus it is unsurprising that the STELLGAP continua do not line up exactly with the continua predicted from theory. The AEs computed are not as localized as they should be if a true separatrix were included. Recall that the accumulation of continua at the separatrix effectively limits the radial extent of modes due to continuum coupling. In addition, the continuum branch curves from theory are from the solution at the O-point. Figs. 4.6 and 4.7 identify an HAE mode that exists throughout the core of the magnetic island, not just at the O-point. If the continua from theory were plotted for surfaces further out from the O-point within the island, better agreement may be obtained. Nevertheless, the STELLGAP/AE3D simulations

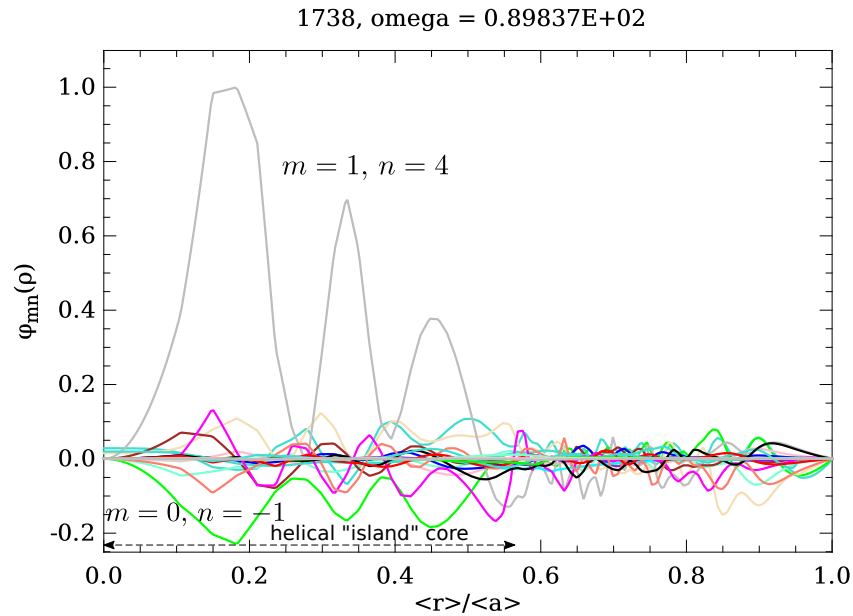


Figure 4.7 Helicity-induced Alfvén eigenmode (HAE) from 200 kA MST case, computed using AE3D. The mode is localized to the helical core and is dominated by $m = 1, n = 4$, along with coupling to $m = 0, n = -1$. At this lower v_A (from lower I_p), the eigenfrequency is 90 kHz.

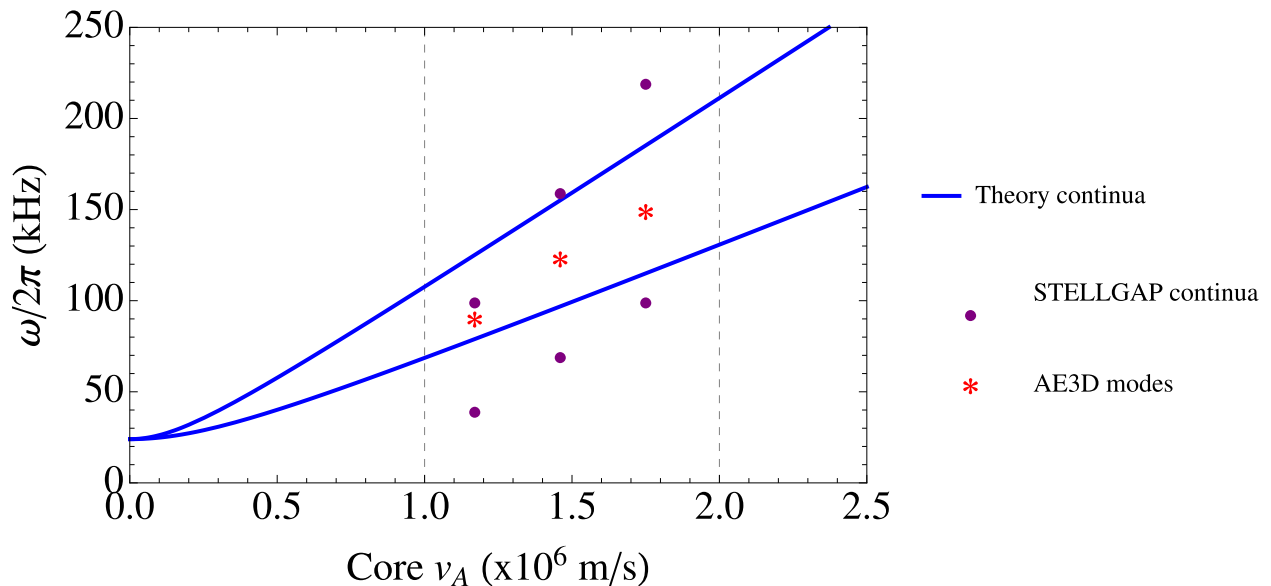


Figure 4.8 Comparison of theory, STELLGAP, and AE3D frequencies vs. Alfvén speed. The $j_{in} = 1$ and $j_{in} = 2$ continuum branches from theory and the computed STELLGAP continuum frequencies from the helical core both increase with increasing $v_A \sim I_p$; the gap also increases with v_A . The AE3D mode frequencies lie in the gaps obtained from both theory and STELLGAP.

appear to capture the essence of the $n_0 = 5$ island core and the shear Alfvén continua and HAE mode contained within.

4.5 Summary

MST has been modeled as a Single Helical Axis (SHAx) equilibrium in VMEC. The $m = 1$, $n = 5$ helical core present in this equilibrium serves as an approximation to the island found in non-reversed MST plasmas. Using this VMEC closed-surface approximation, the STELLGAP and AE3D codes have been utilized to find the shear Alfvén continua and discrete modes, respectively. The continuum branches computed with STELLGAP agree relatively well with the continua from theory in the core of an island. An $n = 4/n = -1$ coupled Helicity-induced Alfvén Eigenmode (HAE) has been found with AE3D in the helical core of the SHAx equilibrium. A scan in plasma current was conducted, and the mode is a robust feature for the range of currents in which the AE is observed experimentally.

We have established the existence of an Alfvén mode located in the helical core of the SHAx equilibrium in VMEC, our approximation to an island. This HAE found with AE3D is an important first step in categorizing the $n = 4$ activity on MST. However, to truly get the details correct and to identify the Alfvén bursts as an island-induced mode, an equilibrium containing an actual island must be used. The SIESTA equilibrium code is capable of resolving this topology containing two magnetic axes.

Chapter 5

Computing MHD modes with the SIESTAIfvén code

SIESTA is a three-dimensional equilibrium code capable of resolving magnetic islands [55]. Most MHD equilibrium codes such as VMEC [38] and EFIT [56] assume the existence of nested, topologically toroidal flux surfaces. Several equilibrium codes such as HINT [57], PIES [58], and SPEC [59] have been developed that allow for magnetic islands; however these codes all use a very different approach from SIESTA and have been dogged by overly simplistic geometries or restrictively slow computation time. SIESTA fills a much needed gap, allowing for very fast, scalable simulations of global equilibria containing multiple islands and stochastic regions.

SIESTA is in many ways the logical successor to the VMEC equilibrium code. A large suite of codes have been developed around VMEC. VMEC serves as the equilibrium “engine” of sorts for stability codes, extended MHD simulations, neoclassical transport calculations, and of course experimental reconstruction codes (like V3FIT [48]). SIESTA was written by the same author as VMEC (Steve Hirshman), and actually begins its calculations with an equilibrium from VMEC. The hope is that one day SIESTA can fill the role that VMEC currently plays: the MHD equilibrium engine for a myriad of other simulations, but with the added ability to handle magnetic islands.

SIESTA requires a VMEC equilibrium as input, and utilizes this as a starting equilibrium. From there, magnetic perturbations and resistivity are included to form islands if the configuration is unstable to tearing modes. In this chapter the SIESTA energy minimization process is discussed, followed by a presentation on the addition of inertia to SIESTA and the modifications made with the new SIESTAIfvén code. SIESTAIfvén is a new code for finding the MHD modes from a SIESTA equilibrium. Finally, SIESTAIfvén is benchmarked against the AE3D code.

5.1 The Scalable Iterative Equilibrium Solver for Toroidal Applications (SIESTA)

SIESTA, the Scalable Iterative Equilibrium Solver for Toroidal Applications, is a code for resolving an equilibrium containing islands [55]. SIESTA uses the fixed coordinate representation of the closed flux surfaces from VMEC as a static coordinate system throughout the perturbation and convergence process. SIESTA uses the square root of normalized flux $r = \sqrt{s}$ as its radial coordinate, where s is the normalized flux from VMEC. This is used to provide better resolution of the equilibrium flux surface structure near the magnetic axis. In order to compare SIESTA and VMEC results to each other, the radial mapping from the VMEC s coordinate to the SIESTA r coordinate must be taken into account. Because VMEC uses a uniformly spaced radial mesh in s while SIESTA uses a uniformly-spaced radial mesh in $r = \sqrt{s}$, some care has to be used in analyzing the gridding for derivatives, etc. Throughout this thesis, results are generally shown in r -space, the natural radial coordinate for SIESTA. This also makes comparison to experiment easier since $r = \langle r \rangle / \langle a \rangle$.

5.1.1 MHD equilibrium energy principle

The SIESTA iterative scheme works as follows. Beginning with a VMEC equilibrium, non-ideal resonant perturbations are added. Next, the nonlinear ideal MHD energy is minimized by solving the linearized ideal MHD force balance equations for a new plasma displacement. After each major iteration, resistive perturbations to the magnetic field are added to continue the tearing process (if unstable). After each step, the nonlinear force is obtained and compared to the specified force tolerance. If it is above the tolerance, the process is repeated. If it is below the tolerance, an equilibrium solution has been found.

In order to minimize the MHD force residual and obtain force balance, the energy is minimized using an MHD energy principle. SIESTA has the same expression for total energy as VMEC (magnetic plus pressure),

$$W = \int \left(\frac{B^2}{2} + \frac{p}{\gamma - 1} \right) dV, \quad (5.1)$$

but the details of each term differ due to the included resistive effects. For a variational treatment, the time derivative of the energy is taken. Using Faraday's law and particle conservation,

$$\frac{\partial \mathbf{B}}{\partial t} = -\nabla \times \mathbf{E}, \quad (5.2)$$

$$\frac{\partial p}{\partial t} = (\gamma - 1)\mathbf{v} \cdot \nabla p - \gamma \nabla \cdot (p\mathbf{v}), \quad (5.3)$$

the change in total energy is given by

$$\frac{\partial W}{\partial t} = \int [-\mathbf{E} \cdot \mathbf{J} + \mathbf{v} \cdot \nabla p] dV - \oint \mathbf{S} \cdot d\mathbf{A}. \quad (5.4)$$

To reach this form, Ampère's law $\nabla \times \mathbf{B} = \mathbf{J}$ and the Poynting and kinetic flux equation $\mathbf{S} = \mathbf{E} \times \mathbf{B} + \gamma/(\gamma - 1)p\mathbf{v}$ have been used.

Currently SIESTA only runs in fixed boundary mode; this allows the surface integral term to be dropped. Using the resistive Ohm's law $\mathbf{E} + \mathbf{v} \times \mathbf{B} = \eta \mathbf{J}$, the MHD energy principle becomes

$$\frac{\partial W}{\partial t} = - \int [\mathbf{v} \cdot (\mathbf{J} \times \mathbf{B} - \nabla p) + \eta J^2] dV. \quad (5.5)$$

The velocity \mathbf{v} is the variational parameter. The resistivity is decreased to zero, $\eta \rightarrow 0$ as the energy is minimized, leading to an equilibrium where W is stationary and $\mathbf{F} = \mathbf{J} \times \mathbf{B} - \nabla p = 0$.

Integrating the time out of Eq. (5.5) without the resistivity, the equation becomes the variation in W in terms of the perturbed MHD displacement vector $\boldsymbol{\xi}$ where $\boldsymbol{\xi} = \mathbf{v}\Delta t$:

$$\delta W = \int [B_i \delta B^i + \delta p] \sqrt{g} dr du dv. \quad (5.6)$$

The variational energy has been written in terms of SIESTA's curvilinear coordinates r , u , and v , and Einstein summation notation is used. The δW variation's dependence on the displacement $\boldsymbol{\xi}$ comes through the perturbed pressure and the perturbed magnetic field:

$$\delta \mathbf{B} = \nabla \times (\boldsymbol{\xi} \times \mathbf{B}), \quad (5.7)$$

$$\delta p = (\gamma - 1)\boldsymbol{\xi} \cdot \nabla p - \gamma \nabla \cdot (p\boldsymbol{\xi}). \quad (5.8)$$

SIESTA tries to minimize Eq. (5.6) using ξ as the unconstrained variational parameter. In terms of SIESTA's curvilinear representation, the variations in Eq. (5.6) are

$$\delta B^i = \frac{\partial}{\partial x^j} (\xi^i B^j - \xi^j B^i), \quad (5.9)$$

$$\delta p = -\gamma \frac{\partial (p \xi^i)}{\partial x^i} + (\gamma - 1) \xi^i \frac{\partial p}{\partial x^i}. \quad (5.10)$$

It should be noted that the Jacobian and the metric elements, \sqrt{g} and g_{ij} , are for the background static coordinate system, and thus do not evolve during the variational process.

With the help of Eqs. (5.9) and (5.10), the variational principle in Eq. (5.6) can be written explicitly in terms of the displacement,

$$\delta W = - \int F_i \xi^i \sqrt{g} dr du dv, \quad (5.11)$$

with $i \in (r, u, v)$, \sqrt{g} the Jacobian, and the covariant force components given by the following:

$$F_i = \epsilon_{ijk} \sqrt{g} J^j B^k - \frac{\partial p}{\partial x^i}, \quad (5.12)$$

where x^i is a shorthand for the (r, u, v) coordinates. The resistivity η will be discussed in Sec. 5.1.4.

5.1.2 Fourier representation and boundary conditions

In SIESTA, the spectral representation of the surfaces is given by

$$R = \sum_{n=-n_{max}}^{n_{max}} \sum_{m=0}^{m_{max}} R_{m,n}(r) \cos(mu + nv), \quad (5.13)$$

$$Z = \sum_{n=-n_{max}}^{n_{max}} \sum_{m=0}^{m_{max}} Z_{m,n}(r) \sin(mu + nv). \quad (5.14)$$

Here m spans only non-negative integers up to a maximum specified mode number $0 \leq m \leq m_{max}$, and n spans both positive and negative integers $-n_{max} \leq n \leq n_{max}$ for a specified value of n_{max} . Care has to be taken in comparing mode numbers between SIESTA and VMEC since SIESTA uses trig arguments of $mu + nv$ while VMEC uses $mu - nv$. The relationship between mode numbers for the two codes is $n_{SIESTA} = -n_{VMEC}$. n_{VMEC} corresponds to the

physical toroidal mode number n that is generally used, and $n = n_{VMEC}$ will be used when discussing SIESTA Alfvén simulation results in Chapter 6. Currently, SIESTA is restricted to stellarator-symmetric fields. Each quantity has a definite even or odd parity in stellarator symmetry, similar to the above representation for R and Z . With stellarator symmetry, the pressure, magnetic field, and displacement have the following Fourier expansions:

$$p = \sum_{m,n} p_{m,n}(r) \cos(mu + nv), \quad (5.15)$$

$$B^r = \sum_{m,n} B_{m,n}^r(r) \sin(mu + nv), \quad (5.16)$$

$$B^\beta = \sum_{m,n} B_{m,n}^\beta(r) \cos(mu + nv), \quad (5.17)$$

$$\xi^r = \sum_{m,n} \xi_{m,n}^r(r) \cos(mu + nv), \quad (5.18)$$

$$\xi^\beta = \sum_{m,n} \xi_{m,n}^\beta(r) \sin(mu + nv), \quad (5.19)$$

where $\beta \in (u, v)$. In the future, there are plans to remove the stellarator symmetry restriction in SIESTA.

The boundary conditions at the coordinate axis $r = 0$ are given by the following:

$$\frac{\partial \phi}{\partial u} = 0, \quad (5.20)$$

$$\frac{\partial \mathbf{h}}{\partial u} = 0. \quad (5.21)$$

This condition holds for any vector \mathbf{h} and scalar ϕ . The boundary condition is for the coordinate singularity obtained from the static VMEC coordinates, which generally does not coincide with the magnetic axis once SIESTA has perturbed the configuration during the energy minimization process.

5.1.3 Preconditioning with the Hessian

In order to solve for the new displacement at each iteration, SIESTA must solve a linear system. Using the steepest descent algorithm (one of several methods SIESTA can use), the plasma displacement is found at each iteration using a positive-definite preconditioner matrix \mathbf{P} as part

of a Krylov subspace solve. Given a force residual \mathbf{F} at the current iteration, the new perturbed displacement is

$$\xi^i = P^{ij} F_j. \quad (5.22)$$

Plugging this into Eq. (5.11) for the variation gives

$$\delta W = - \int F_i P^{ij} F_j dV \leq 0, \quad (5.23)$$

which is less than or equal to zero since P^{ij} is positive definite. In this form, it is clear that the energy functional is stationary if and only if the MHD force residual is zero.

At each overall nonlinear iteration, SIESTA computes a new MHD displacement according to Eq. (5.22). Within this step, multiple linear iterations of the solution are performed to obtain a proper linear solution. Any positive-definite preconditioner P^{ij} can be used, but an intelligent choice of the preconditioner based on the relevant physics will lead to faster convergence to equilibrium. Before discussing the proper preconditioner that is used, it should be noted that SIESTA has a slightly curious representation of the displacement within the code. For primarily book-keeping reasons, the Jacobian from the volume differential in Eq. (5.11) is multiplied by the MHD displacement and labeled as Γ^i within SIESTA:

$$\Gamma^i = \sqrt{g} \xi^i. \quad (5.24)$$

The magnetic field, pressure, force, and energy are all represented within SIESTA in terms of Γ^i . In terms of this modified plasma displacement, the preconditioned equation to solve for the new perturbation becomes the following:

$$\Gamma^i = P^{ij} F_j. \quad (5.25)$$

To motivate selection of the preconditioner in SIESTA, consider a configuration at iteration n in SIESTA, with an MHD force residual $\mathbf{F}_n = \mathbf{J}_n \times \mathbf{B}_n - \nabla p_n$. One method to determine the plasma displacement Γ^i that will minimize the energy functional is to linearize the MHD equations about the current position and set the total linearized force to zero, which becomes the next iteration $n + 1$:

$$\mathbf{F}_{n+1} = \mathbf{F}_n + \delta \mathbf{J} \times \mathbf{B}_n + \mathbf{J}_n \times \delta \mathbf{B} - \nabla \delta p = 0. \quad (5.26)$$

The linear terms are all functions of the displacement Γ and can be written in terms of a linearized MHD force operator acting on the displacement. This force operator is just the Hessian matrix, given as follows:

$$\mathbf{H}_n = \frac{\partial \mathbf{F}_n}{\partial \Gamma} = -\frac{\partial^2 W}{\partial \Gamma \partial \Gamma}, \quad (5.27)$$

$$\mathbf{H}_n \Gamma = \delta \mathbf{J} \times \mathbf{B}_n + \mathbf{J}_n \times \delta \mathbf{B} - \nabla \delta p. \quad (5.28)$$

With the Hessian operator acting on the displacement, Eq. (5.26) becomes

$$\mathbf{H}_n \Gamma = -\mathbf{F}_n. \quad (5.29)$$

This is just a linear system of equations for the plasma displacement; comparing this to Eq. (5.25), we see that an intelligent choice of the preconditioner is the inverse of the Hessian matrix:

$$\mathbf{P} = -\mathbf{H}_n^{-1}. \quad (5.30)$$

Using this preconditioner for the energy minimization is equivalent to solving the linear system in Eq. (5.29) for the new displacement at each iteration. When the computed force residual \mathbf{F}_{n+1} is not yet below the specified tolerance due to nonlinear terms in Γ^i , the process iterates on itself. After enough iterations, the simulation should converge to an equilibrium once the force residual drops below a specified tolerance.

The Hessian operator is a matrix with block tridiagonal structure arising from the presence of second-order radial derivatives in the MHD force. Each block row (column) corresponds to a radial flux surface. Within each block, the indices span the directional (r, u, v) components as well as the included Fourier mode numbers m and n . Spectral coupling in the equations leads to blocks which are densely populated. SIESTA can be run in serial to invert the Hessian matrix at each iteration, but is much faster when run in parallel. BCYCLIC is a parallel cyclic reduction algorithm developed at Oak Ridge National Lab for factoring block tridiagonal matrices, such as the Hessian [60]. While the details of the parallel version of SIESTA are out of the scope of this thesis, information on the scaling with processors can be found in the BCYCLIC paper as well as additional work by Sudip Seal [61]. In the author's experience, most SIESTA simulations with relevant parameters can now be run in parallel in 5 minutes or less (often under a minute).

5.1.4 Opening magnetic islands

The iterative scheme discussed so far employs strictly ideal MHD. If SIESTA only considered ideal perturbations, the frozen flux theorem would not allow the topology to change from the initial VMEC equilibrium, and islands could not form. SIESTA allows for the formation of islands through two processes: non-ideal “island” perturbations and finite resistivity. First, we will discuss the non-ideal perturbations. SIESTA applies an initial non-ideal magnetic perturbation given by

$$\delta\mathbf{B} = \nabla \times \left(A_{\parallel} \hat{\mathbf{b}} \right). \quad (5.31)$$

The perturbation from this parallel vector potential seeds a small amplitude island in the configuration. The parallel component of the vector potential is $A_{\parallel} = -E_{\parallel} \Delta t$, where the non-ideal parallel electric field can be written as $E_{\parallel} = (\mathbf{E} \cdot \mathbf{B})/B$. Within SIESTA, $e = \mathbf{E} \cdot \mathbf{B}$ is chosen such that it causes a negative change in magnetic energy given by

$$\delta W = - \int \mathbf{J} \cdot \mathbf{E} dV = - \int K e \sqrt{g} dr du dv, \quad (5.32)$$

where the parallel current is given by $K = \mathbf{J} \cdot \mathbf{B}/B^2$. Prior to island formation, the localized current sheet K at the resonant surface shields the island from forming.

The simplest choice for the non-ideal electric field e is to set $e \sim K$, which corresponds to adding parallel resistivity. While this would lead to the steepest descent to equilibrium, it also causes resistive changes in the global current and thus modifies the safety factor profile. In order to preserve the q -profile, e is chosen such that the global, non-resonant current profile is preserved but the resonant shielding of parallel current at the rational surface is diminished, leading to the opening of an island. This is done by picking e as follows:

$$e \sim K_{resonant} = \sum_{m,n-resonant} (\sqrt{g}K)_{m,n}(r) \cos(mu + nv). \quad (5.33)$$

In this equation, only the resonant m and n values are included in the summation. Thus the mean $m = 0, n = 0$ component of the current is not included in this expression and will not be diffused (Δ' remains unchanged), leaving the q -profile globally intact. The components in Eq. (5.33) are

resonant at the radial positions $r_{m,n}$ where $m - nq(r_{m,n}) = 0$. As discussed in Sec. 5.1.2, Eq. (5.33) has even parity in $mu + nv$ due to the imposed stellarator symmetry.

In order to open islands, the radial profile of e must contain “tearing parity”. The tearing mode parity for the parallel electric field is even about the resonant radius; this diffuses the δ -function parallel currents. The odd parity is not included in the parallel electric field, which allows the rippling $1/x$ Pfirsch-Schlüter currents to remain in the converged equilibrium. These odd parallel currents are required to balance the curvature-driven perpendicular currents in the continuity equation:

$$\nabla \cdot \mathbf{J} = \mathbf{B} \cdot \nabla K + \nabla_{\perp} \cdot \mathbf{J}_{\perp} = 0. \quad (5.34)$$

The even tearing parity in Eq. (5.33) is imposed in SIESTA through the following version of the parallel current which is symmetrized with respect to $r_{m,n}$:

$$\tilde{K}_{m,n}(r) = \frac{a_{m,n}(r)}{2} \left[(\sqrt{g}K)_{m,n}(|r - r_{m,n}| + r_{m,n}) + (\sqrt{g}K)_{m,n}(-|r - r_{m,n}| + r_{m,n}) \right]. \quad (5.35)$$

In this expression, the parallel current K is evaluated at the symmetrized radius argument. $a_{m,n}(r)$ is a filter function for each m, n that is zero when the arguments of $K_{m,n}$ are outside the allowable range of $0 \leq r \leq 1$ and a constant $a_{m,n}^0 > 0$ when the arguments are within the allowable range. The choice of non-ideal electric field perturbation $e \sim \tilde{K}_{m,n}$ gives a negative-definite resistive change in magnetic energy:

$$\delta W = - \int \sum_{m,n-\text{resonant}} \tilde{K}_{m,n}^2(r) dr < 0. \quad (5.36)$$

The odd-parity rippling component of K integrates to zero. The perturbation strength $a_{m,n}^0$ must be chosen small enough so that the linearization of energy in Eq. (5.32) is valid. In addition, if the perturbation is chosen too large, the simulation will not converge as shown in Table 5.1.

In addition to the non-ideal tearing perturbation, SIESTA also includes finite resistivity to allow islands to form in fewer iterations and converge quickly to a lower energy state. At resonant rational surfaces, the VMEC starting equilibrium contains current sheets required by ideal MHD to prevent island formation. The finite resistivity in SIESTA allows these singular current structures to diffuse

and islands to open. Following each major ideal iteration step n detailed above, SIESTA diffuses the parallel currents through a combination of Faraday’s law and the resistive Ohm’s law:

$$\frac{\partial \mathbf{B}}{\partial t} = -\nabla \times \mathbf{E}, \quad (5.37)$$

$$\mathbf{E} = \eta \mathbf{J}. \quad (5.38)$$

Combining these equations and using vector identities and SIESTA coordinates, one arrives at the equation for the non-ideal perturbed magnetic field components:

$$\delta B^i = \nabla \cdot (\eta \Delta t \mathbf{J} \times \nabla x^i). \quad (5.39)$$

The resistive time-step Δt is determined by CFL stability. In a form of time-splitting, several iterations of this equation are run following every major ideal iteration. However, the resistivity is reduced and eventually turned off when a small value of the force residual is reached. From that moment on, all iterations are purely ideal, and the simulation is able to converge to an ideal MHD equilibrium containing islands. The iterative scheme employed in SIESTA is shown in Fig. 5.1.

In the version of SIESTA used for this work, the magnetic perturbation size is still controlled manually through specifying the magnitude of A_{\parallel} ($a_{m,n}^0$ discussed above). In practice, SIESTA is now quite robust with respect to this user-controlled parameter. For most equilibria that the author has studied, a helical perturbation in the range of 1×10^{-3} to 5×10^{-3} will give approximately the same solution, with an island width of nearly the same size. The reason that this is possible is because of the finite resistivity in SIESTA. The perturbation acts as an initial “guess” for the island, and the resistivity essentially provides a tearing rate for convergence to equilibrium.

A study has been conducted for the MST configuration of interest, in which a sizable $n_0 = 5$ island should be present. A scan in the size of the applied helical perturbation (‘HelPert’ in SIESTA’s variable naming) was performed, while keeping the resistivity at the “standard” numerical resistivity of $\eta = .01$ typically used in these simulations. The equilibrium obtained was studied along with the number of iterations required to obtain convergence. Table 5.1 presents the results including the number of iterations and the details of island formation. A perturbation size of $A_{\parallel} = 1 \times 10^{-3}$ is found to be too small to seed an island; no topology change can be seen. For perturbations in the

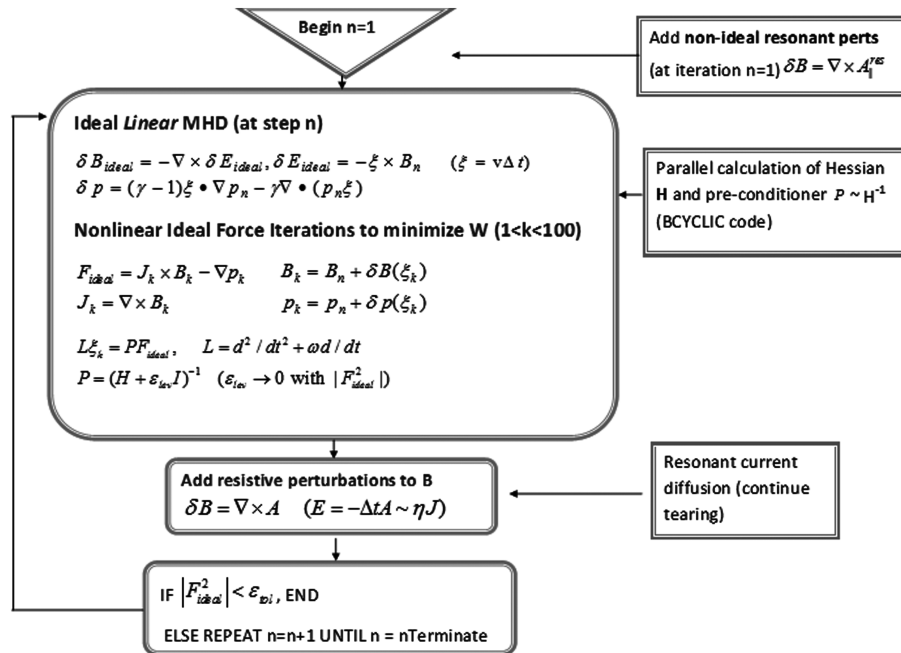


Figure 5.1 Flow chart of iterative scheme used in SIESTA. Figure from Hirshman, Sanchez, Cook, 2011 PoP [55].

HelPert A_{\parallel}	# iterations	Island formed?
1×10^{-3}	6	No
2×10^{-3}	7	Yes
3×10^{-3}	7	Yes
4×10^{-3}	8	Yes
5×10^{-3}	8	Yes
6×10^{-3}	12	Not converged

Table 5.1 Scan of input helical perturbation size A_{\parallel} in SIESTA. If the perturbation is too small, no island is obtained. If the perturbation is too large, the simulation does not converge and the flux surface structure breaks down.

range of $A_{\parallel} = 2 \times 10^{-3}$ to 5×10^{-3} , an equilibrium with an island is obtained in 7 or 8 iterations. Finally, $A_{\parallel} = 6 \times 10^{-3}$ is found to be too large of a perturbation, as the simulation does not converge within 12 iterations and the flux surfaces are broken and stochastic due to the overly large perturbation. These results demonstrate that the combination of non-ideal perturbations with resistivity makes SIESTA relatively robust to the choice in A_{\parallel} , with very similar equilibria obtained for A_{\parallel} in the range of 2×10^{-3} to 5×10^{-3} . The Lundquist number $S = \mu_0 L v_A / \eta$ for an MST SIESTA simulation with $\eta = .01$ is approximately $S \sim 2 \times 10^3$, which is quite low. This small Lundquist number corresponds to a resistivity that is higher than that found experimentally for MST. This high resistivity is always used in SIESTA simulations for convergence purposes; the code does not follow physical timescales during its energy minimization descent. The large value for resistivity helps the SIESTA simulations converge quickly. Recall that the resistivity is turned down to zero as the force residual decreases, so that there is no resistivity once the final ideal MHD equilibrium is obtained.

5.2 Including inertia with the SIESTAfvén code

Once an equilibrium is found with SIESTA, the computed Hessian matrix gives half of the necessary dynamics for computing the normal modes of the system. No inertial term is present during

the energy minimization process; if inertia is included once an equilibrium is found, the proper ideal MHD normal modes of the system can be computed from the Hessian and inertia matrices. A post-processing code called SIESTA_{Alfvén} has been written to find the Alfvén eigenmodes from a SIESTA equilibrium.

5.2.1 MHD eigenmode equations with inertia

In order to use SIESTA as an eigenmode solver, the inertia must be included in the MHD equations. Returning to Eq. (5.29),

$$\mathbf{H}_n \Gamma = -\mathbf{F}_n, \quad (5.29)$$

this is the linearized ideal MHD momentum equation without the inertial term containing the mass density. Including an inertia matrix \mathbf{T} to be defined later in SIESTA coordinates, the ideal MHD momentum equation is

$$-\omega^2 \mathbf{T} \Gamma = \mathbf{F}_n + \mathbf{H}_n \Gamma. \quad (5.40)$$

Once SIESTA converges and an equilibrium is found at iteration N , $F_N \rightarrow 0$, force balance is obtained, and the linearization is about a proper MHD equilibrium. The momentum equation is then linearized about the equilibrium:

$$-\omega^2 \mathbf{T} \Gamma = \mathbf{H}_N \Gamma. \quad (5.41)$$

The Hessian matrix \mathbf{H}_N (\mathbf{H} from this point on) is computed in SIESTA at each iteration and is easily dumped from the code once an equilibrium is found. Obtaining the inertia matrix \mathbf{T} from SIESTA and solving Eq. (5.41) with SIESTA_{Alfvén} will be the topic of this section.

The linearized MHD equation, Eq. (5.41), is a generalized eigenvalue problem for eigenmode $\Gamma = \sqrt{g} \xi$ and eigenfrequency ω^2 . This system contains the full MHD eigenspectrum, with the shear Alfvén modes as a subset. Eq. (5.41) is written explicitly in terms of the desired physical displacement vector ξ :

$$-\omega^2 \mathbf{T} \sqrt{g} \xi = \mathbf{H} \sqrt{g} \xi. \quad (5.42)$$

In SIESTA coordinates, the inertia tensor is given by $T_{ij} = \rho g_{ij} / \sqrt{g}$. Substituting this into the eigenmode equation results in

$$-\omega^2 \rho g_{ij} \xi^j = H_{ij} \sqrt{g} \xi^j. \quad (5.43)$$

Writing the eigenproblem in terms of ξ^j suggests the following forms for the modified Hessian and inertia matrices:

$$\tilde{H}_{ij} = H_{ij} \sqrt{g}, \quad (5.44)$$

$$\tilde{T}_{ij} = \rho g_{ij}. \quad (5.45)$$

In terms of these modified tensors (which actually correspond to the physical Hessian and inertia), the system to be solved with SIESTAfvén is

$$-\omega^2 \tilde{T}_{ij} \xi^j = \tilde{H}_{ij} \xi^j. \quad (5.46)$$

5.2.2 Constructing the inertia matrix

A new module within SIESTA called `inertia.f90` has been written for the purpose of dumping out the necessary information from SIESTA for constructing \tilde{H}_{ij} and \tilde{T}_{ij} . The inertia module is used by the existing hessian module within SIESTA, and the `computeInertia` subroutine from the inertia module is called in `hessian.f90` immediately after the blocks of the Hessian matrix are dumped out. The `computeInertia` subroutine computes the quantities needed for the SIESTAfvén post-processing code and dumps them out to five text files.

First, the lower metric elements $g_{ij} = \mathbf{e}_i \cdot \mathbf{e}_j$ where $i \in [r, u, v]$ are obtained from SIESTA. The six lower metric elements g_{ij} in real space are available in the metrics module. There are only six stored instead of nine because g_{ij} is a symmetric tensor so $g_{uv} = g_{vu}$, $g_{ru} = g_{ur}$, and $g_{rv} = g_{vr}$. The inertia and Hessian matrices, \tilde{T}_{ij} and \tilde{H}_{ij} in Eq. (5.46), must be represented in Fourier m, n space. Since the Hessian matrix H_{ij} already computed in SIESTA is block-tridiagonal in Fourier space, the generalized eigenvalue problem is naturally cast in m, n space. Working in Fourier space allows for more efficient solution of the eigenvalue problem due to the tridiagonal block structure and the solvers available for this type of matrix. The real space g_{ij} components from the metrics module are Fourier transformed to obtain the m, n space components in the `computeInertia` routine. Next,

these Fourier coefficients have to be packed into a metric matrix with two indices (row and column) that each run through radius, (r, u, v) vector components, and toroidal and poloidal harmonics n and m . This is primarily a book-keeping exercise, and involves translating the metrics stored in an m, n array into an m, n, m', n' matrix where m, n are the Fourier components for the row index and m', n' are the Fourier components of the column index. The translation from array to matrix is performed according to $m \rightarrow m - m'$ and $n \rightarrow n - n'$. Additionally, the components must remain bounded such that $0 \leq m, m' \leq m_{max}$ and $-n_{max} \leq n, n' \leq n_{max}$. The g_{ij} matrix is block diagonal in Fourier space since the metrics are local quantities involving no coupling between surfaces. The computed blocks are written out to the text file ‘TBLK.txt’ once SIESTA converges to equilibrium.

Next the Jacobian \sqrt{g} is needed. Similar to the g_{ij} metrics, the Jacobian is stored in SIESTA in real space in the quantities module. In computeInertia, \sqrt{g} is transformed to Fourier space. The Jacobian is a scalar quantity, and thus only contains the radius and m, n components. It operates on all vector components equivalently. The Jacobian is dumped to the ‘JBLK.txt’ file by the inertia module at the end of the SIESTA simulation.

Some additional data from SIESTA needs to be dumped for constructing the shear Alfvén displacement ξ_{surf} from the eigenmode vector components ξ^r , ξ^u , and ξ^v once they are computed by SIESTA_{Alfvén}. This process will be discussed in detail in Sec. 5.2.3. For now, it is important to know that the covariant magnetic field components, ∇p data, metrics in real space, and Fourier mode information from SIESTA need to be written out at the end of the simulation for future post-processing. The real space g_{ij} components from the metrics module are written out to file in ‘siestametrics.txt’. Information on the Fourier representation in SIESTA is contained in the cos/sin components in the islandparams module as well as the orthonorm parameter (for normalizing θ^*) from fourier.f90. This data is written out to the ‘siestafourier.txt’ file. The ∇p components can be obtained in the quantities module. The covariant \mathbf{B} field components must be computed from the contravariant components, which are also available in the quantities module. The contravariant components are stored in real space, and the covariant components are computed in inertia.f90

from the lower metrics and contravariant \mathbf{B} according to

$$B_r = g_{ri} B^i, \quad (5.47)$$

$$B_u = g_{ui} B^i, \quad (5.48)$$

$$B_v = g_{vi} B^i. \quad (5.49)$$

∇p and the B_i components are dumped out to the file ‘siestabfieldpres.txt’.

In addition to all of the new text files that are dumped out in inertia.f90, the hessian module in SIESTA writes the Hessian matrix out to three text files. The main diagonal blocks are written to ‘DBLK.txt’, the upper diagonal blocks are dumped out in ‘UBLK.txt’, and the lower diagonal blocks are dumped in ‘LBLK.txt’.

With all of these text files written out at the end of a SIESTA simulation, the next step is to run the siestapost program that was written to construct \tilde{H}_{ij} and \tilde{T}_{ij} from all of the dumped data. \tilde{H}_{ij} is computed in a very straightforward manner. Recall from Eq. (5.45) that $\tilde{H}_{ij} = H_{ij} \sqrt{g}$. Since the Jacobian \sqrt{g} has been dumped in ‘JBLK.txt’ in matrix form and the SIESTA Hessian H_{ij} is dumped in matrix block form, the desired Hessian \tilde{H}_{ij} is computed block by block by performing matrix multiplication on the blocks of H_{ij} and \sqrt{g} . This modified Hessian still retains the block-tridiagonal structure of the original and is written to the file ‘amatrix.dat’ by siestapost to be read in by the eigenvalue solver.

To compute $\tilde{T}_{ij} = \rho g_{ij}$, the g_{ij} components in Fourier space are read in from ‘TBLK.txt’. SIESTA never explicitly calculates the plasma mass density ρ (recall there is no inertia in SIESTA), so instead it is specified. The siestapost code reads in the density from the same ‘plasma.dat’ file used by STELLGAP and AE3D. Wherever possible, SIESTA lfvén makes use of modular components of AE3D post-processing routines so that simple comparisons can be made between the two codes. A namelist of user-specified parameters for the density profile is read. The ion to proton mass ratio m_i/m_p for the plasma species is obtained in this manner, and the ion density profile is input through several modeling options including a polynomial fit, a constant profile, and several other profile-shaping options. The radial density profile ρ is constructed from this namelist data in siestapost and multiplied by the metric elements g_{ij} to obtain the inertia tensor \tilde{T}_{ij} . Since the

ion mass density ρ is a scalar, the multiplication is simple, with $\rho(j_s)$ multiplying every Fourier component of the g_{ij} block on surface j_s . \tilde{T}_{ij} is a block diagonal matrix, just like T_{ij} is.

Several other normalization factors are included in the computation of \tilde{T}_{ij} . A factor of $(2\pi)^2$ is included in the inertia matrix to change the eigenvalue from ω^2 in rad/s to f^2 in Hz. A factor of $(10^3)^2$ is also included to scale the eigenvalues in kHz. With the normalization factors, $\tilde{T}_{ij} = \rho g_{ij}$ is written out to ‘bmatrix.dat’. Finally, siestapost writes out a ‘jdqz.dat’ file for use by the JDQZ eigenvalue solver, to be discussed in the next in Sec. 5.2.3. This file contains information about the dimensions of the Hessian and inertia matrices, including the number of block rows and the size of the blocks. It contains an array of included Fourier mode numbers m and n , as well as an array of the radial surface locations from SIESTA. The surfaces must be specified according to SIESTA’s uniform grid in $r = \sqrt{s}$.

At this point, we now have an eigenvalue problem for the physical displacements ξ^i and their frequencies in kHz, f :

$$\tilde{H}_{ij}\xi^j = -f^2\tilde{T}_{ij}\xi^j. \quad (5.50)$$

Writing out the individual components of the matrices and vectors explicitly gives the following:

$$\tilde{H}_{ij}^{mn\rho,m'n'\rho'}\xi_{m'n'\rho'}^j = -f^2\tilde{T}_{ij}^{mn\rho,m'n'\rho'}\xi_{m'n'\rho'}^j, \quad (5.51)$$

where m, m' are poloidal mode numbers, n, n' are toroidal mode numbers, and ρ, ρ' are radial indices. The displacement ξ^j is a column vector, and the $mn\rho$ before the comma in the superscript of the two matrices is the row indexing while the $m'n'\rho'$ after the comma is the column indexing.

5.2.3 Solving for the MHD eigenmodes

In order to solve this generalized eigenvalue problem, a targeted eigenvalue solver called JDQZ is used. The LAPACK routine dggev was initially used, but for problems of this size the dggev serial generalized eigensolver was prohibitively slow. The Hessian and inertia matrices generally contain 100 to 200 flux surfaces and mode ranges around $m_{max} \sim 5$ and $n_{max} \sim 10$. This gives 100+ block rows with block size $3(m_{max} + 1)(2n_{max} + 1) \sim 380$, therefore the system contains

around 38,000 equations. Due to the sheer size of this system, novel approaches have been applied for finding the eigenmodes.

To get around the inefficient solution with LAPACK, SIESTA_{Alfvén} now uses JDQZ, a Jacobi-Davidson algorithm for finding the eigenfunctions near a specified target frequency. By limiting its eigenvalue search to modes near a target eigenvalue, JDQZ can run much more quickly than an eigensolver that finds all the eigenvalues and vectors. The Hessian and inertia matrices \tilde{H}_{ij} and \tilde{T}_{ij} are given to the JDQZ solver from the ‘amatrix.dat’ and ‘bmatrix.dat’ files, respectively. Information about the matrix size is passed in through ‘jdqz.dat’, and the target frequency (in kHz) is specified as a command line argument. Within the JDQZ code, the number of desired eigenmodes and frequencies can be set manually and is usually set to around 40. Once the JDQZ code runs and finds the eigenmodes and frequencies, it writes the ξ^i contravariant components to ‘gammasupsasci.dat’, ‘gammasupuasci.dat’, and ‘gammasupvasci.dat’ (the ‘gamma’ naming convention is retained from an older version of the code, but these are indeed ξ^i and not Γ^i). The eigenfrequencies are written to the ‘egvalues.dat’ text file.

5.2.4 Constructing the shear Alfvén displacement

Now we have the capability to compute the spectrum of MHD eigenmodes and frequencies, with the desired shear Alfvén modes as a subset. However, the current representation of the eigenmodes as ξ^r , ξ^u , and ξ^v is not the most useful representation for studying the Alfvén displacements. Recall from Chapter 2 that for shear Alfvén modes, the displacement is dominated by a binormal surface component, given by

$$\xi_{surf} = \boldsymbol{\xi} \cdot (\mathbf{B} \times \nabla\Phi^*) / |\nabla\Phi^*|^2, \quad (5.52)$$

where Φ^* is the helical flux that labels magnetic surfaces in the presence of an island. The problem with trying to compute this displacement from our ξ^i eigenvectors in SIESTA coordinates is that there is no explicit Φ^* coordinate that defines the flux surfaces in SIESTA. Recall that the (r, u, v) coordinates come from the initial VMEC equilibrium without an island. At this starting point, the flux surfaces lie on surfaces of constant r , so ∇r plays the role of $\nabla\Phi^*$. However, as soon as

the islands begin to form through perturbations and resistivity as the simulation evolves, the flux surfaces change but the coordinate system remains fixed. As an obvious example, take the region local to an island; ∇r , the radial direction from the closed nested flux surface initial equilibrium, is now not perpendicular to the helical island flux surfaces at all. In fact, in some places it is parallel.

The solution to all of this lies in the pressure. In the initial VMEC equilibrium, the pressure contours lie on surfaces of constant r and can be specified as radial profiles. Once an equilibrium with islands is obtained in SIESTA, the pressure is no longer a function of r , but is now a function of r , u , and v . Since the equilibrium is in ideal MHD force balance, $\mathbf{J} \times \mathbf{B} = \nabla p$, the flux surfaces are still surfaces of constant pressure in a SIESTA equilibrium with an island. The perpendicular to the flux surfaces can be identified with ∇p , which plays the role of $\nabla \Phi^*$. Using the pressure, the shear Alfvén displacement in a SIESTA equilibrium is

$$\xi_{surf} = \boldsymbol{\xi} \cdot \frac{(\mathbf{B} \times \nabla p)}{|\mathbf{B} \times \nabla p|}. \quad (5.53)$$

No problems from a uniform pressure have been encountered thus far, as $\nabla p \neq 0$ inside an island in a SIESTA equilibrium. A contravariant representation for the eigenmode displacements was obtained using JDQZ, $\boldsymbol{\xi} = \xi^r \mathbf{e}_r + \xi^u \mathbf{e}_u + \xi^v \mathbf{e}_v$ for each mode. A code has been written for computing ξ_{surf} from ξ^r , ξ^u , and ξ^v . The code, called `xsurfdisp`, is run after the JDQZ solver has been used to find the eigenmodes and frequencies. It reads in the ξ^i components in Fourier space from ‘`gammasupsasci.dat`’, ‘`gammasupuasci.dat`’, and ‘`gammasupvasci.dat`’. The magnetic field and pressure gradient in real space are read in from ‘`siestabfieldpres.txt`’. Both vectors are in a covariant representation, $\mathbf{B} = B_r \nabla r + B_u \nabla u + B_v \nabla v$ and $\nabla p = \partial p / \partial r \nabla r + \partial p / \partial u \nabla u + \partial p / \partial v \nabla v$.

In order to compute the $\mathbf{B} \times \nabla p$ vector, the ∇p and \mathbf{B} components are combined as follows:

$$(\mathbf{B} \times \nabla p)^k = \epsilon^{ijk} \frac{B_i}{\sqrt{g}} \frac{\partial p}{\partial x^j}. \quad (5.54)$$

Here ϵ^{ijk} is the Levi-Civita symbol. The magnitude of the binormal vector is then computed in the normal manner, with $|\mathbf{B} \times \nabla p| = \sqrt{g_{ij} (\mathbf{B} \times \nabla p)^i (\mathbf{B} \times \nabla p)^j}$. The lower metric elements g_{ij} in real space are read in from ‘`siestametrics.txt`’. After normalizing the $\mathbf{B} \times \nabla p$ vector as $\mathbf{f} = \mathbf{B} \times \nabla p / |\mathbf{B} \times \nabla p|$, \mathbf{f} is a true binormal.

code	STELLGAP	AE3D	SIESTAlfvén
equilibrium	VMEC	VMEC	SIESTA
computes continua	Y	Y	N
computes AEs	N	Y	Y
compressibility	N	N	Y
allows islands	N	N	Y

Table 5.2 Comparison of the features of the STELLGAP, AE3D and SIESTAlfvén codes.

Next, the m, n components of ξ^i from JDQZ are inverse-Fourier transformed back to real space. The surface displacement component is computed in real space through the dot product between ξ and \mathbf{f} : $\xi_{surf} = g_{ij}\xi^i f^j$. Finally, the surface displacement is transformed back to Fourier space, and the Fourier components of ξ_{surf} are written to the file ‘xisurfasci.dat’. Now the actual binormal shear Alfvén surface component of the eigenmodes have been obtained.

The displacement components ξ^r, ξ^u, ξ^v , as well as the surface component ξ_{surf} have been written to file in the same manner as is done in AE3D, and thus can be studied using the same post-processing plotting routines developed for that code. An extension has been written for the xplotegn routine written by Don Spong for analyzing modes from AE3D. With the new extension, the SIESTAlfvén-computed AEs can be plotted and the user has the ability to specify the desired component at the command line. Both the ξ^i components from the ‘gammasupxasci.dat’ files and the ξ_{surf} component from ‘xisurfasci.dat’ can be visualized in this manner. The normal component has also been computed according to $\xi_{\perp} = \xi \cdot \nabla p / |\nabla p|$. For the shear Alfvén modes analyzed in Chapter 6, this perpendicular component has been found to be about an order of magnitude smaller than ξ_{surf} .

A comparison of the features in the STELLGAP, AE3D, and SIESTAlfvén codes is shown in Table 5.2. SIESTAlfvén is most closely related to the AE3D code; both are used to compute the discrete Alfvén eigenmodes. Because of this, SIESTAlfvén is benchmarked with AE3D.

5.3 Benchmarking SIESTA_{Alfvén} against AE3D for a TAE case

In order to benchmark SIESTA_{Alfvén} with the AE3D code, a circular RFP test case with a $q = 3/2$ surface is used. Two Alfvén waves couple together at the $3/2$ rational surface to form the toroidicity-induced Alfvén eigenmode (TAE) gap mode. Recall that an m, n mode couples to an $m + 1, n$ mode at the radius where $q = (m + 1/2)/n$. Thus the $q = 3/2$ surface will couple the $m_1 = 1$ and $m_2 = 2$ components of an $n = 1$ TAE mode. The STELLGAP code was used initially to identify the TAE gap frequency range. The computed continua contain an $m_1 = 1, m_2 = 2$ -coupled TAE gap from 10 – 20 kHz. The frequencies are low because this test case comes from an MST configuration with a q -profile that is scaled up to cross the $3/2$ surface in the core.

In this test case, no perturbation is used in SIESTA so no island is present in the resulting equilibrium. Because AE3D contains only incompressible dynamics $\nabla \cdot \xi = 0$ [5], while SIESTA includes finite compressibility and retains Alfvén-acoustic wave coupling [55], care has to be taken when comparing the two codes. In an effort to remedy this, the ratio of specific heats γ in SIESTA has been increased from the standard value of $5/3$ to 10. This large value of γ is used to approximate incompressibility in SIESTA.

AE3D and SIESTA_{Alfvén} were both run on this equilibrium to compute the discrete TAE. The TAEs computed with AE3D and SIESTA_{Alfvén} agree quite well. The computed eigenfrequencies agree to within 4%, with AE3D at 15.8 kHz and SIESTA_{Alfvén} at 16.4 kHz. As shown in Fig. 5.2, the TAE mode structures found with both codes are reasonably similar. Both are localized around the $r = \sqrt{s} = 0.1$ surface, where the gap is located. Both consist of a coupling between the $m_1 = 1, n = 1$ and $m_2 = 2, n = 1$ modes. The magnitude of the components, and not the sign, should be compared between the two simulations. The differences in the computed modes may be because AE3D computes in VMEC $s = \psi$ poloidal flux space while SIESTA_{Alfvén} computes in SIESTA $r = \sqrt{s}$ space. The uniform radial mesh in r in SIESTA affords more resolution close to the axis where this particular mode resides, while the uniform mesh in s in AE3D gives less resolution in the core.

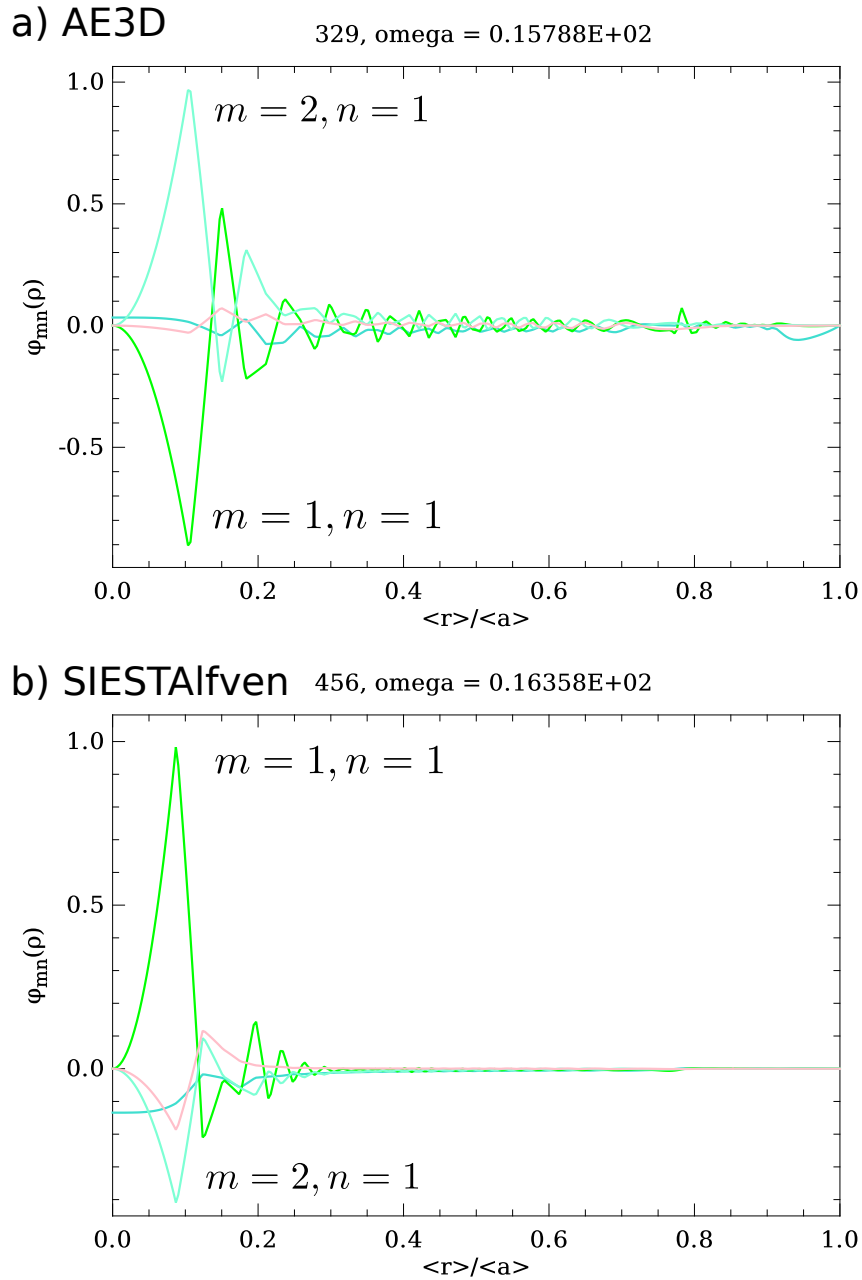


Figure 5.2 Toroidicity-induced Alfvén Eigenmode test case computed using a) AE3D and b) SIESTAIfven. The mode is comprised of a coupling between the $m = 1, n = 1$ and $m = 2, n = 1$ Fourier components. The mode is localized near the $q = 3/2$ surface, as expected for this TAE. The frequency of the mode is computed as 15.8 kHz with AE3D and 16.4 kHz with SIESTAIfven.

5.4 Summary

The SIESTA equilibrium code for resolving configurations containing magnetic islands has been described. A new post-processing code called SIESTAAlfvén has been introduced that constructs an inertia matrix along with the Hessian matrix obtained from a converged SIESTA equilibrium. These matrices form a generalized MHD eigenvalue problem given by $-\omega^2 \tilde{T}_{ij} \xi^j = \tilde{H}_{ij} \xi^j$ that SIESTAAlfvén solves using JDQZ for the MHD mode displacements ξ^j and eigenfrequencies ω^2 for the configuration. These eigenmodes are analyzed to find the shear Alfvén modes. The SIESTAAlfvén code has been benchmarked against AE3D for a TAE test case, and reasonable agreement was found.

Chapter 6

Identification of the Island-induced Alfvén Eigenmode (IAE)

The continuum theory presented in Chapter 3 suggests that the $n = 4$ Alfvén bursts observed in MST neutral beam-driven plasmas may be localized to the core of the $n_0 = 5$ island present in the core; these modes may arise from an island-induced helical coupling. Simulations using the VMEC and STELLGAP/AE3D codes in Chapter 4 found a mode existing in the helical core consistent with the predictions from theory. The mode frequency lies in the helicity-induced gap as expected. These computational results lend credence to the idea that the MST modes are IAEs, but a simulation containing a true island and separatrix are still needed to confirm that the island-coupled mode is real.

In this chapter, the SIESTA_{Alfvén} code introduced in Chapter 5 is used to investigate the existence of an Island-induced Alfvén Eigenmode (IAE) in MST. SIESTA simulation results for MST are presented. The configuration contains a sizable core $n_0 = 5$ island is found in the equilibrium as expected from experiment. Using the SIESTA_{Alfvén} solver, an $n = 4$ IAE is identified in this configuration, confirming that the Alfvénic activity on MST is indeed caused from an island coupling. The characterization of this new class of Alfvén mode is detailed. Additional $n = -1$ activity observed on MST is also discussed, along with several possible explanations for the mode. A new mode called the Island-induced Global Alfvén Eigenmode (IGAE) is identified and proposed to explain the observations.

6.1 MST SIESTA equilibrium

The non-reversed MST configuration with an island from experiment has been reproduced using the SIESTA code. Beginning with an axisymmetric VMEC equilibrium for the case with $I_p = 300$ kA and $B_\zeta = 0$ on edge, SIESTA is run with a non-ideal magnetic perturbation of $A_\parallel = 3 \times 10^{-3}$ Tm and standard resistivity of $\eta = 0.01$. The simulation converges to an equilibrium with a negligible force residual ($< 10^{-26}$) and a sizable $m_0 = 1$, $n_0 = 5$ island present in the plasma core. 201 flux surfaces are used for this computation.

The pressure contours from the converged SIESTA equilibrium are shown in Fig. 6.1. The surfaces of constant pressure are plotting in real R, Z space. Near the original magnetic axis, a large island is present with poloidal mode number $m_0 = 1$. The island width is about 15 cm and has a bean-shaped appearance, consistent with reconstructions from experiment. If more pressure surfaces are included in the plot, the original circular magnetic axis can also be seen, but the high number of surfaces makes an overly busy figure that is difficult to see. Fig. 6.2 displays the Poincaré puncture plots for the SIESTA magnetic field \mathbf{B} through a surface of constant poloidal angle, θ . The punctures are plotted in $\zeta, r = \sqrt{s}$ space. In this plane, the toroidal mode number $n_0 = 5$ is clearly visible.

6.2 The Island-induced Alfvén Eigenmode (IAE)

SIESTA_{Alfvén} is now used to investigate the MHD modes present in MST. The SIESTA equilibrium is used to initialize the SIESTA_{Alfvén} eigenmode computations. Next, the siestapost routine in SIESTA_{Alfvén} constructs the matrices needed for the MHD eigenmode problem, Eq. (5.50):

$$\tilde{H}_{ij}\xi^j = -f^2\tilde{T}_{ij}\xi^j. \quad (5.50)$$

Along with the data from SIESTA, an ion density profile must be specified in order to compute $\tilde{T}_{ij} = \rho g_{ij}$. In the ‘plasma.dat’ file the ion to proton mass ratio is set to $m_i/m_p = 2$ for deuterium plasmas of interest to match MST experiment. The ionprofile=3 option in ‘plasma.dat’ is used,

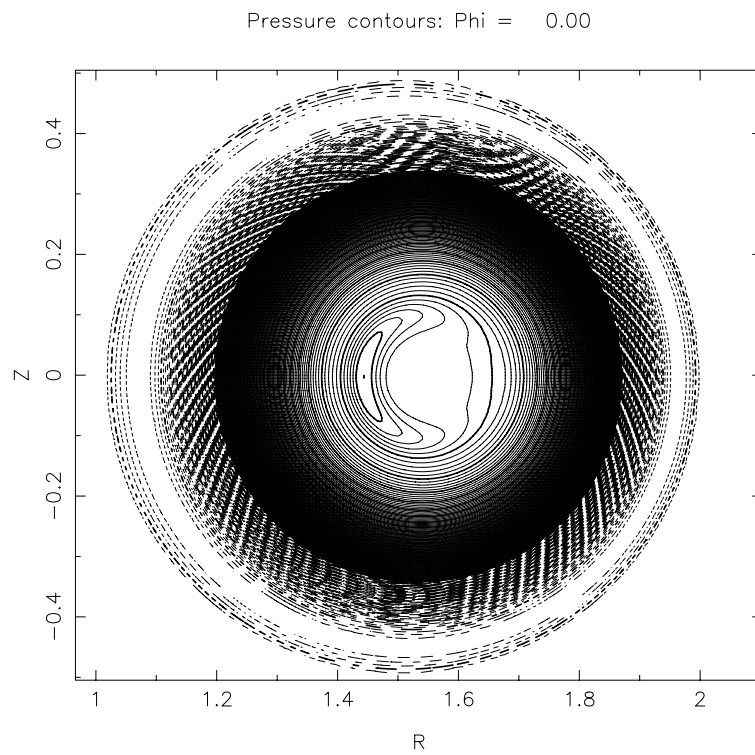


Figure 6.1 Contours of constant pressure in a poloidal plane from an MST SIESTA equilibrium. The $m_0 = 1$ character of the island is clearly visible. The circular axis is still present, and can be seen if more surfaces are included in the plot.

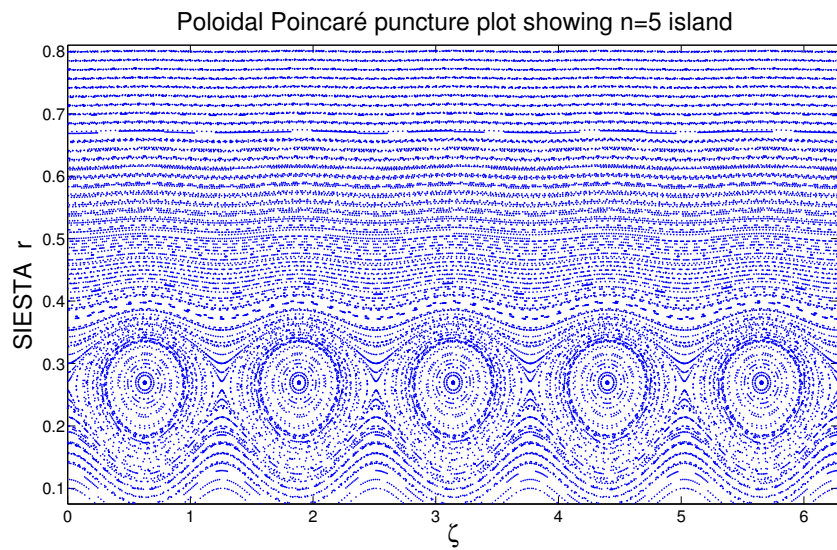


Figure 6.2 Poincaré puncture plot from the SIESTA B field intersecting a toroidal plane at constant θ . Punctures are shown for $r = \sqrt{s}$ vs. ζ . The $n_0 = 5$ component of the island can be seen clearly.

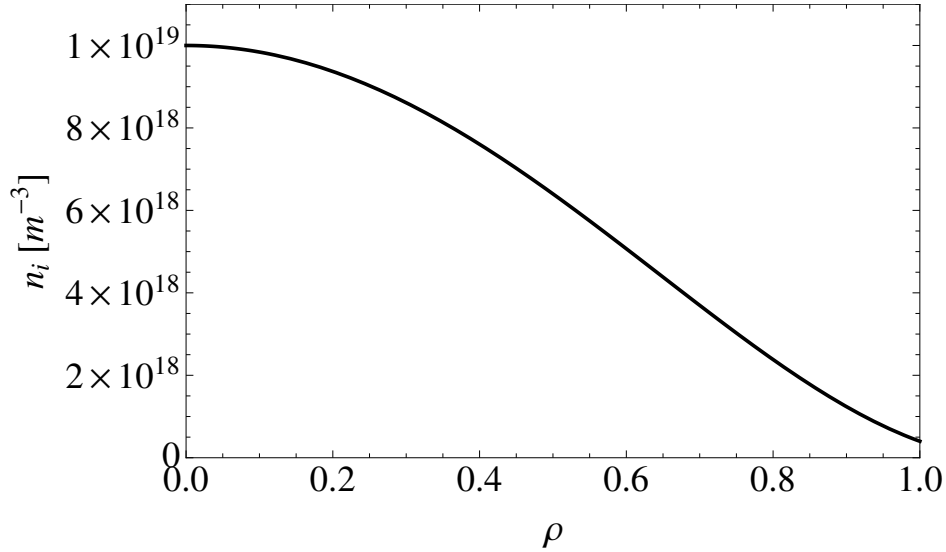


Figure 6.3 Ion density profile for MST from the equation $n_i = n_0 (1 - a\rho^b)^c$, plotted vs. normalized poloidal flux. This profile is used for the SIESTAlfvén simulation.

which specifies an ion density profile in the form

$$n_i = n_0 (1 - a\rho^b)^c, \quad (6.1)$$

where n_0 , a , b , and c are all specified by the user. Here ρ is the normalized poloidal flux (s from VMEC). The physically relevant parameters from experiment were obtained from Jon Koller. The density on axis is $n_0 = 1 \times 10^{19}/m^3$ and $a = 0.8$, $b = 2$, and $c = 2$. The resulting profile from these parameters is presented in Fig. 6.3. The profile has an integrated average density of $\langle n_i \rangle = 0.7 \times 10^{19}/m^3$ matching experiment. From this density profile and the Jacobian \sqrt{g} , SIESTAlfvén constructs the matrices \tilde{H}_{ij} and \tilde{T}_{ij} .

6.2.1 Discovery of the IAE with SIESTAlfvén

Next, the generalized eigenvalue problem from Eq. (5.50) is solved using JDQZ in SIESTAlfvén. The eigenmode solutions are then analyzed, as they contain both discrete modes and SIESTA's approximations to continuum modes. The continuum modes tend to be nearly singular, but because the SIESTA flux surfaces are not surfaces of constant r a radial singularity in the SIESTA radius r does not correspond cleanly to a mode restricted to a single magnetic surface. This is a numerical

issue stemming from the fact that our coordinate system from VMEC are not magnetic flux coordinates in SIESTA. Because of this, SIESTA_{Alfvén} cannot currently be used to solve for the continuum modes as STELLGAP does. After examining the solutions, a discrete mode was discovered at 145 kHz. In the plasma core, the \mathbf{B} field is largely in the v direction. Globally, s remains the normal to the original flux surfaces, so s is not a valid normal coordinate for the perturbed flux surfaces in the vicinity of the island. Because of this, the shear Alfvén displacement is mainly in the poloidal u direction. The contravariant u component of the mode ξ^u is presented in Fig. 6.4. It is found that $\xi^u \gg \xi^s, \xi^v$, as expected. The actual shear Alfvén surface component ξ_{surf} is computed as a post-processing step to the JDQZ solve by SIESTA_{Alfvén}. Recall from Sec. 5.2 that this component is given by $\xi_{surf} = \boldsymbol{\xi} \cdot (\mathbf{B} \times \nabla p) / |\mathbf{B} \times \nabla p|$. The IAE surface displacement is plotted in Fig. 6.5. This component is valid even local to the island and illustrates the proper computed structure of the mode. The mode is dominated by two peaks of $n = 4$ and $n = -1$ toroidal harmonics localized to the core of the magnetic island, which extends from about $r = 0.1$ to $r = 0.4$. This mode is the first identification of an island-induced Alfvén eigenmode, named here the IAE. The 145 kHz frequency found is consistent with the 140 – 160 kHz observed on MST for the relevant Alfvén speed, $v_A = 1.75 \times 10^6 m/s$. It is also very close to the 149 kHz frequency found with AE3D in Sec. 4.3.2.

6.2.2 Mode structure of the IAE

The double-peak character present in the IAE structure is consistent with the coupling between mode numbers expected for gap modes (in this case $\delta n = 5$) [14]. This is the same type of helical coupling present in the helicity-induced Alfvén eigenmode (HAE) in Fig. 4.6. Fig. 6.6 shows a cartoon of the helical/island coupling relevant to the IAE. Recall that the HAE found with VMEC/AE3D in Chapter 4 for an $n_0 = 5$ SHAx state was dominated by $n = 4$ and $n = -1$ harmonics, corresponding to $\delta n = 5$. This $\delta n = 5$ helical coupling is also present in the IAE mode computed with SIESTA_{Alfvén}. The IAE was discovered in an island with $n_0 = 5$ field periods. The island-induced Alfvén eigenmode has the same coupling as an HAE and arises due to the island's

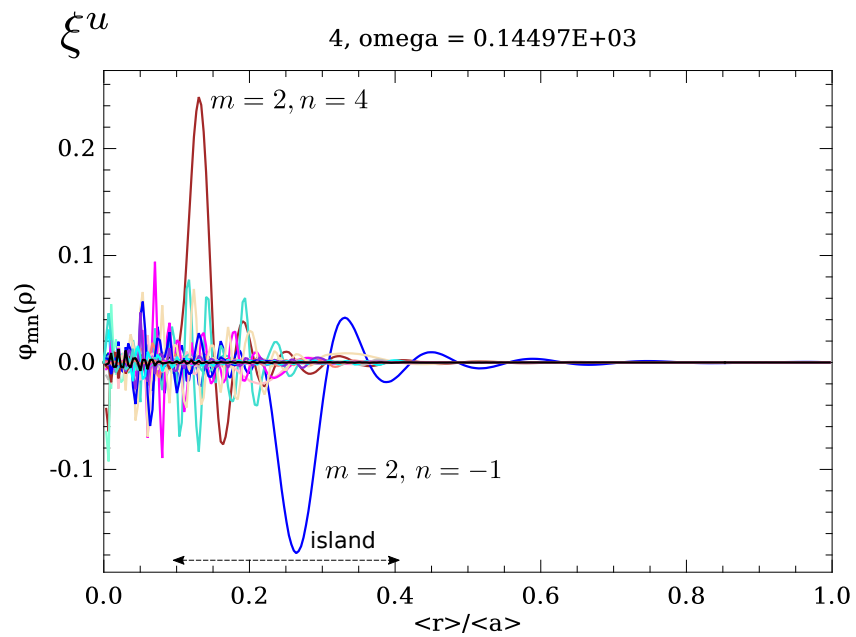


Figure 6.4 Island-induced Alfvén Eigenmode (IAE) in MST computed with the SIESTAAlfvén code. The Fourier mode components of the contravariant u (poloidal) component of the displacement are plotted vs. $\sqrt{\psi}$. The IAE is localized within the magnetic island. The frequency of the mode is 145 kHz, in agreement with 140 – 160 kHz from experiment.

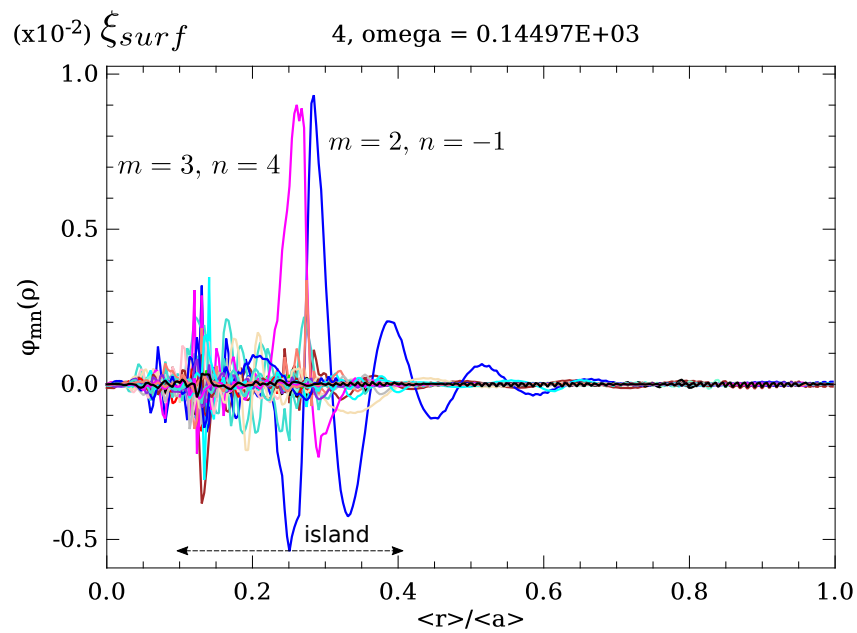


Figure 6.5 Island-induced Alfvén Eigenmode (IAE) in MST computed with the SIESTAAlfvén code. The Fourier mode components of the proper shear Alfvén surface displacement are plotted vs. $r = \sqrt{s}$. The mode is dominated by an island-induced helical coupling between the $n = 4$ and $n = -1$ Fourier components and is localized within the magnetic island. The frequency of the mode is 145 kHz, in agreement with 140 – 160 kHz from experiment.

helical behavior. However the IAE is localized to the core of a magnetic island, while an HAE is found in the bulk plasma of a stellarator or an RFP in a SHAx state.

The poloidal Fourier harmonic m is the mode number with respect to VMEC θ . Recall that SIESTA represents fields in terms of a static set of VMEC coordinates, $r = \sqrt{s}$, $u = \theta$, and $v = \zeta$; for example the pressure is represented as

$$p = \sum_{m,n} p_{m,n}(r) \cos(mu + nv). \quad (6.2)$$

Once a magnetic island forms, u is no longer a “poloidal”-like angle on surfaces in and near the island. A flux surface in the island extends through a range of both r and u , and the island is localized to a small range of poloidal angle u . Because of this, m is not a good number for surfaces inside the island. For a mode localized to the core of an island, as the IAE in Fig. 6.5 is, the poloidal mode number m is not very meaningful since an infinite number of poloidal harmonics in the Fourier transform would be necessary to properly capture the mode. This explains the high amount of mode content present in the eigenmode. The Fourier components in the IAE with lower amplitudes are almost entirely made up of the other m values for $n = 4$ and $n = -1$. This significant m mode content does not decrease with more flux surfaces and is present in simulations containing 100 to 300 surfaces. Instead of m , the proper mode number inside the magnetic island is j_{in} as discussed in Chapters 2 and 3. Unfortunately this quantum number from theory is not available from the VMEC coordinates in SIESTA, or the measurements from experiment for that matter. The n value from SIESTA is referenced with respect to a toroidal transit around the device and is a useful, physical mode number.

6.3 Unexplained $n = -1$ activity on MST

The two main Fourier components of the SIESTA-alfvén-computed IAE are the $n = 4$ and $n = -1$. The Alfvénic burst observations from MST discussed thus far have all been $n = 4$. It turns out that $n = -1$ activity has also been observed on MST. Fig. 6.7 from Lin [54] shows the temporal evolution of $n = 5$, $n = 4$, and $n = -1$ beam-driven instabilities on MST measured through poloidal magnetic field fluctuations. Generally an $n = 5$ energetic particle mode (EPM)

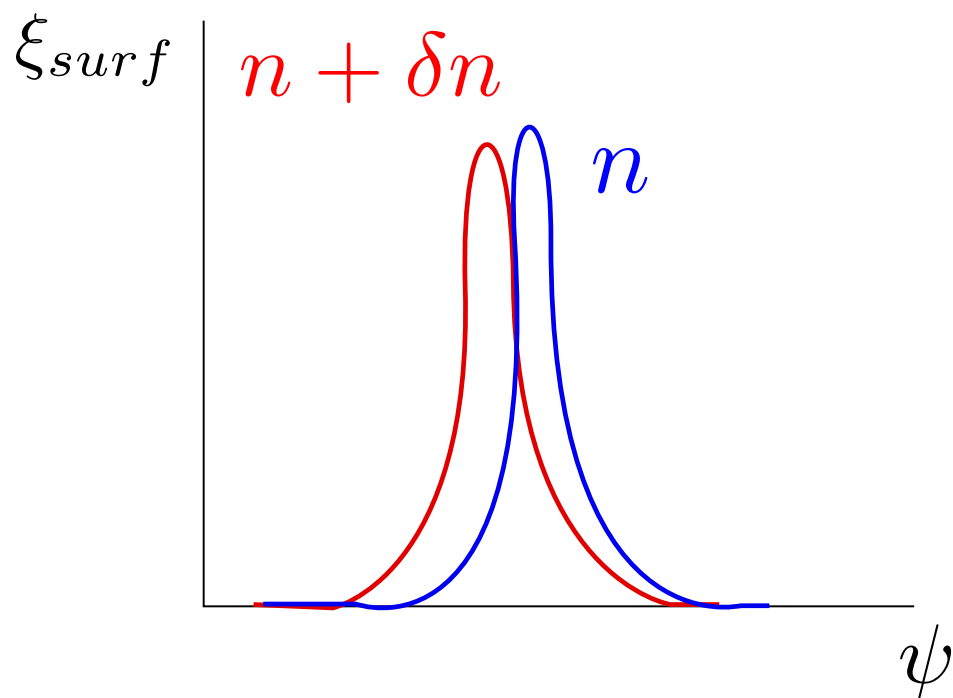


Figure 6.6 Cartoon showing the n and $n + \delta n$ toroidal harmonics coupled together to produce the Island-induced Alfvén Eigenmode (IAE). The mode is localized in the core of the magnetic island.

is excited first, followed by a brief transition through an $n = -1$ mode at a low-amplitude to the $n = 4$ Alfvén eigenmode that has been discussed in detail throughout this thesis. The $n = -1$ mode is observed at a smaller amplitude than the $n = 4$ AE and a much smaller amplitude than the $n = 5$ EPM, making it more difficult to characterize. Additionally, the $n = -1$ mode is observed through density fluctuations at a radial location that is slightly outboard from the location of the $n = 4$ AE. Fig. 6.8 shows temporal evolution and radial resolution of density fluctuation data for the $n = 5$, $n = -1$, and $n = 4$ modes; the transition from $n = 5$ to $n = -1$ to $n = 4$ is clearly visible in these plots. The $n = 5$ EPM is predominantly located on the inboard side, while the $n = 4$ AE is localized to the outboard side, with the $n = -1$ mode located further outboard.

The $n = -1$ mode is still incompletely characterized from experiment at the time of this writing; ongoing experiments are being performed on MST to further identify this mode. There are two main questions regarding the mode that remain unresolved. First, the type of mode needs to be identified. It is unclear whether the $n = -1$ mode is an Alfvén Eigenmode, an EPM, or something else. In order to determine this, experimental scalings of the mode frequency with the NBI velocity and the Alfvén speed are needed. If it is determined that the $n = -1$ mode is an AE, the second question is whether it is a unique instability or part of an already-identified mode. In order to answer this question, the frequency of the mode needs to be carefully measured experimentally. If the frequency matches the frequency of another instability, it may be a component of that same mode. If it has a different frequency, it is probably something distinct. Early observations have identified that the $n = -1$ mode oscillates at $f = 65$ kHz [54], but more thorough investigations are currently underway on MST. The reason it can be difficult to measure the frequency is because of the mode's small amplitude and fleeting nature.

Assuming for now that the $n = -1$ mode is an AE (this should be proven or disproven in the near future through more refined measurements), there are three potential candidates for the type of Alfvén eigenmode. The $n = -1$ AE could be a Fourier component of the same IAE that was already detailed in this chapter. It could be a beta-induced Alfvén eigenmode (BAE) living below the BAE accumulation point frequency. Finally, it could be a new type of island-induced global

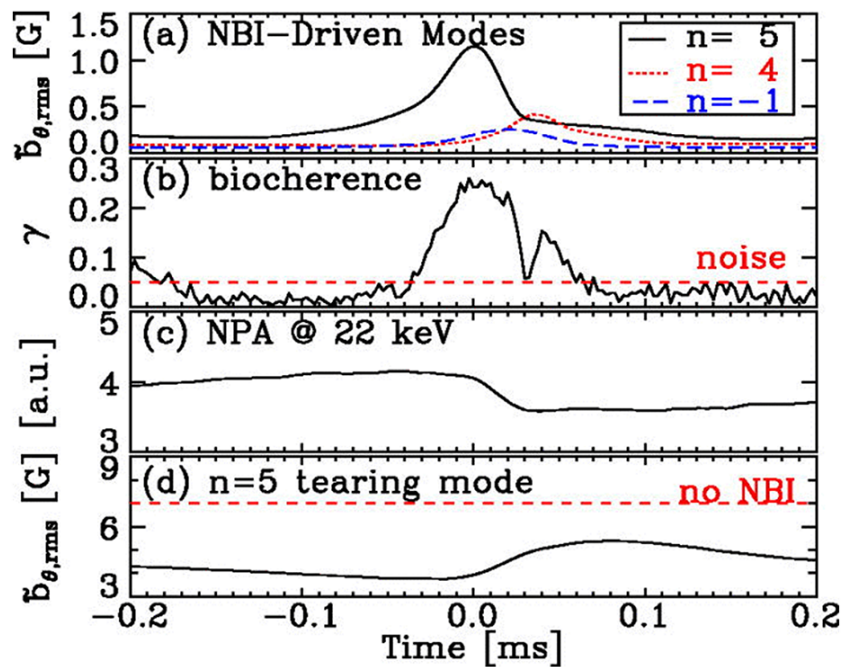


Figure 6.7 Temporal evolution of $n = 5$, $n = 4$, and $n = -1$ NBI-driven modes in MST. The modes are measured through edge poloidal magnetic field fluctuations. The $n = 5$ EPM peaks first, followed by a quick transition through the $n = -1$ to the $n = 4$ AE. Figure from Lin et al., 2013 PoP [54].

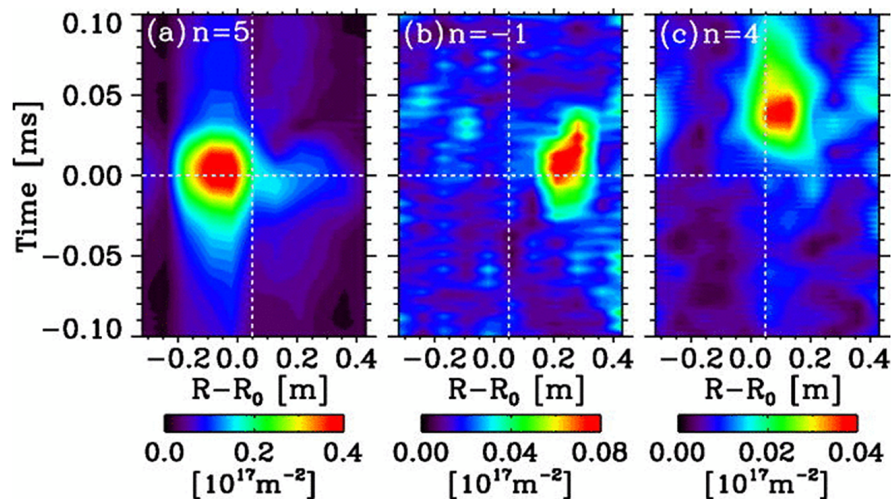


Figure 6.8 Temporal vs. spatial density fluctuation activity on MST. The first plot contains the $n = 5$ EPM, the second the $n = -1$ mode, and the third the $n = 4$ AE. Figure from Lin et al., 2013 PoP [54].

Alfvén eigenmode with a frequency below the lowest continuum branch in the core of the island. Each of these possibilities will now be examined.

6.3.1 $n = -1$ mode as a Fourier component of the IAE

The $n = -1$ mode could be a Fourier component of the island-induced Alfvén eigenmode (IAE) discussed in Sec. 6.2. The IAE computed with SIESTA shown in Fig. 6.5 is comprised of dominant $n = 4$ and $n = -1$ Fourier harmonics from the island's $\delta n = 5$ coupling. The $n = 4$ component of the mode has been observed in experiment in the range of 140 – 160 kHz, which agrees with the computed 145 kHz. The $n = -1$ mode observed on MST could be the other dominant Fourier component of the IAE. If this was the case, the $n = -1$ should be observed around 140 – 160 kHz, along with the $n = 4$ mode since they would be part of the same instability. While still inconclusive, current measurements of the mode at about 65 kHz point to a different explanation. In addition, the $n = -1$ mode also occurs at a slightly different time and radial location from the $n = 4$ activity, further hinting at a different, independent character for this mode.

6.3.2 $n = -1$ mode as an island-upshifted BAE

The $n = -1$ mode could be an Island-upshifted Beta-induced Alfvén Eigenmode, or IBAE. BAE modes are extremum modes that lie below the lowest minimum of the continuum frequencies. Though it is still a shear Alfvén mode, the BAE requires acoustic coupling through the slow-sound approximation $\gamma p / \rho \omega^2 R_0^2 \ll 1$ in order to retain the compressional response of the fluid to transverse Alfvén waves [33]. The effects of a magnetic island on the BAE continuum accumulation point frequency, ω_{BAE} were detailed in Chapter 2 and again in Chapter 3 for MST, EAST, and FTU parameters. The BAE frequency is the minimum frequency of the continuum that occurs at the rational surface (in the absence of an island) when the geodesic curvature from the torus and finite beta effects are included. Recall that the island moves the BAE minimum continuum frequency to the separatrix and upshifts the frequency according to Eq. (3.12) from Chapter 3:

$$f_{sep} = \sqrt{f_{BAE}^2 + \frac{(\epsilon k_{\parallel} v_A)^2}{8}}. \quad (3.12)$$

If the $n = -1$ mode observed in MST experiment lies below the minimum frequency ω_{sep} , it would be consistent with an upshifted IBAE. Experimentally the $n = -1$ mode is found at 65 kHz. Using MST parameters, the minimum frequency at the separatrix from Eq. (3.12) was calculated in Chapter 3 to be $f_{sep} = 25.7$ kHz with only a small upshift from the magnetic island. This minimum continuum frequency is considerably lower than the observed 65 kHz, making the $n = -1$ activity incompatible as an IBAE. This is consistent with expectations for MST, which has weak geodesic curvature κ_s making finite beta effects less important.

In addition to the $n = -1$ activity occurring at a frequency above the island-upshifted BAE gap, the observations are also qualitatively different from the BAE activity in the presence of islands observed on the EAST, FTU, and TEXTOR tokamaks discussed in Chapter 3 [6, 47, 8]. On these tokamaks, BAEs are always observed in pairs with opposite toroidal mode numbers (for example $n = 1$ and $n = -1$), which form standing waves within the island and are believed to receive their energy from nonlinear coupling to the tearing mode. In contrast, the $n = -1$ bursts on MST have not been observed with any counter-propagating $n = 1$ activity. Additionally Fig. 6.7 shows that the $n = -1$ mode amplitude actually increases as the $n = 5$ tearing mode amplitude (island) increases. If the $n = -1$ mode on MST drew its energy from the tearing mode as the BAE does in tokamaks, then the tearing amplitude should decrease as the $n = -1$ ramps up. All of this suggests that the $n = -1$ is not a island-upshifted BAE.

6.3.3 $n = -1$ mode as an Island-induced Global Alfvén Eigenmode (IGAE)

The $n = -1$ mode could be a second type of mode resulting from island effects, identified here as the Island-induced Global Alfvén Eigenmode or IGAE. Motivation for this new AE stems from the fact that the IAE identified in this thesis exists in the gap between the $n = -1$ ($j_{in} = 1$) and $n = 4$ ($j_{in} = 2$) continua computed in STELLGAP, which correspond to the lowest two branches in the island from theory. A discrete mode could exist beneath the lowest $n = -1$ ($j_{in} = 1$) continuum frequency branch. The continuum branches all contain an extremum at the O-point in the form of a local frequency maximum; see Figs. 2.2 and 2.3 in Chapter 2. Recall from Eq. (2.10)

in Chapter 2 that the rotational transform inside the island is given by

$$\Omega = \frac{\pi\epsilon}{4K(\kappa^2)}. \quad (2.10)$$

At the O-point ($\kappa = 0$), the shear in the island rotational transform goes to zero, $\lim_{\kappa \rightarrow 0} \partial\Omega/\partial\kappa = 0$. Similar to a reversed-shear Alfvén eigenmode (RSAE) [62], an extremum in the rotational transform profile $\partial\Omega/\partial\kappa = 0$ corresponds to an extremum in the continuum $\partial\omega/\partial\kappa = 0$ at the island O-point. It has long been established that an extremum in the Alfvén continuum frequencies can allow for discrete modes localized near the extremum point [62, 63]. These modes are known as global Alfvén eigenmodes or GAEs, and exist at a frequency below the extremum continuum frequency. Because the radial variation in the frequency spectrum vanishes at the O-point extremum $\partial\omega/\partial\kappa = 0$, an effective potential well exists that traps the Alfvén wave, creating a GAE [14]. The absence of magnetic shear is the “defect” that localizes the mode. The GAE is characterized by a single poloidal and a single toroidal mode number, m and n , without the δm , δn couplings present in gap modes.

With this extremum in the Alfvén continuum as motivation, an AE scan for a GAE was performed using the AE3D code. The frequency extremum of the $n = -1$ branch at the O-point was found with STELLGAP at 110 kHz. Therefore a GAE mode would be expected in the 0 – 110 kHz range if it exists. Running AE3D in the base case of $I_p = 300$ kA discussed in Chapter 4, a discrete mode was found at 76 kHz. As seen in Fig. 6.9, the mode is localized to the helical core of the “island” in this SHAx equilibrium. It is almost entirely composed of an $m = 0$ and $n = -1$ Fourier component, consistent with a GAE. These mode numbers also agree with the STELLGAP continua computed in Chapter 4 in Figs. 4.2 and 4.3; the lowest continuum branch is $m = 0$, $n = -1$. The computed mode frequency of 76 kHz is quite close to the current experimental measurements of 65 kHz for the $n = -1$ mode. In addition, early experimental measurements indicate that this instability has poloidal mode number $m = 0$, in agreement with the computed AE.

All of this points to the identification of the $n = -1$ activity on MST as a separate $m = 0$, $n = -1$ global mode at 65 – 75 kHz named here the Island-induced Global Alfvén Eigenmode or IGAE. A separate $n = -1$ IGAE and $n = 4$ IAE agrees with the experimental findings of $n = -1$ and $n = 4$ activity peaking at different times and radial locations (see Fig. 6.7). Two

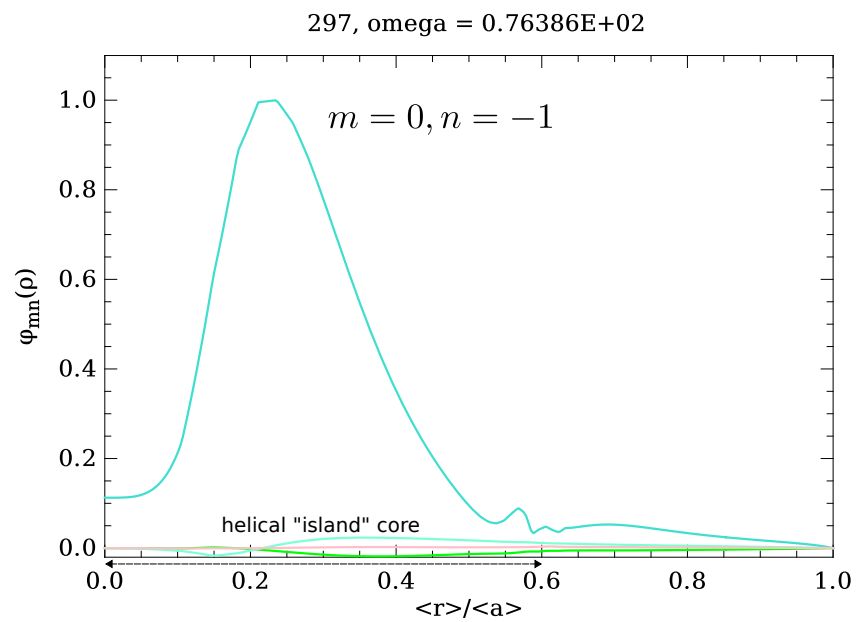


Figure 6.9 Island-induced Global Alfvén Eigenmode (IGAE) computed with AE3D for MST base case with $I_p = 300$ kA. The mode is dominated by a single poloidal and toroidal harmonic, $m = 0$ and $n = -1$, as expected for a GAE. The eigenfrequency computed is 76 kHz, close to the current experimental measurements of 65 kHz for the $n = -1$ instability.

distinct island-induced modes also explains the disparate frequency measurements of 150 kHz for the $n = 4$ activity and 65 kHz for the $n = -1$. Further experimental measurements of the $n = -1$ mode are required to determine satisfactorily whether the instability is indeed an AE and to confirm the mode frequency of 65 kHz. Currently the IGAE looks to be the most plausible explanation for the $n = -1$ burst activity. Further numerical identification of the IGAE can be investigated with the SIESTAAlfvén code and a proper island treatment if warranted in the future based on experimental findings.

The identification of the $n = 4$ IAE and the possible identification of the $n = -1$ IGAE leads to the following physical picture for the NBI-driven activity in MST presented in Fig. 6.7: An $n = 5$ EPM instability is driven by the beam in the core of the $n_0 = 5$ island. The mode is resonant with the island and draws additional energy from the tearing mode, leading to a decrease in tearing mode amplitude. The EPM localized in the island destabilizes a quick succession of Alfvén modes; first the $n = -1$ IGAE at a lower frequency and amplitude and second the $n = 4$ IAE at a higher frequency and amplitude. The EPM transfers its energy into the two AEs and dies off, allowing the tearing mode to rise again.

6.4 Summary

The SIESTAAlfvén code has been used to identify the first true Island-induced Alfvén Eigenmode (IAE) in an MST equilibrium containing an $n_0 = 5$ island. The mode results from a helical coupling of $\delta n = 5$ in the core of the island. The IAE is dominated by $n = 4$ and $n = -1$ toroidal harmonics and was found at a frequency of 145 kHz, consistent with the 140 – 160 kHz $n = 4$ Alfvénic activity observed on MST. The MST observations are now believed to be the first experimental identifications of an IAE. This new type of AE is consistent with the island-induced continuum gap from the theory presented in Chapter 2.

An additional mode, named here the Island-induced Global Alfvén Eigenmode (IGAE) has been found in an MST SHAx equilibrium using AE3D. The mode exists below the minimum $n = -1$ continuum branch and is an $n = -1$ -dominated mode. The IGAE appears to explain the low-frequency $n = -1$ activity that has been observed on MST immediately preceding the $n = 4$

mode. This IGAE has been found at 76 kHz, and the experimental $n = -1$ bursts are observed at 65 kHz. This island-induced mode may be the best candidate for the unexplained bursts, but additional experimental measurements and characterization is needed.

The three new types of island-modified Alfvén eigenmodes presented in this thesis: the Island-induced Alfvén Eigenmode (IAE), the Island-induced Global Alfvén Eigenmode (IGAE), and the Island-upshifted Beta-induced Alfvén Eigenmode (IBAE), are all shown schematically in Fig. 6.10 along with the Alfvén continua. The IAE exists at the highest frequency of the three, in the helical gap between the $j_{in} = 1$ and $j_{in} = 2$ continuum branches. The IGAE exists below the $j_{in} = 1$ branch in the core of the island. Finally, the IBAE exists at the lowest frequency below the continuum accumulation point frequency. The IBAE is the only one of the three not restricted to the interior of the island; it can extend beyond the separatrix without coupling to the continua.

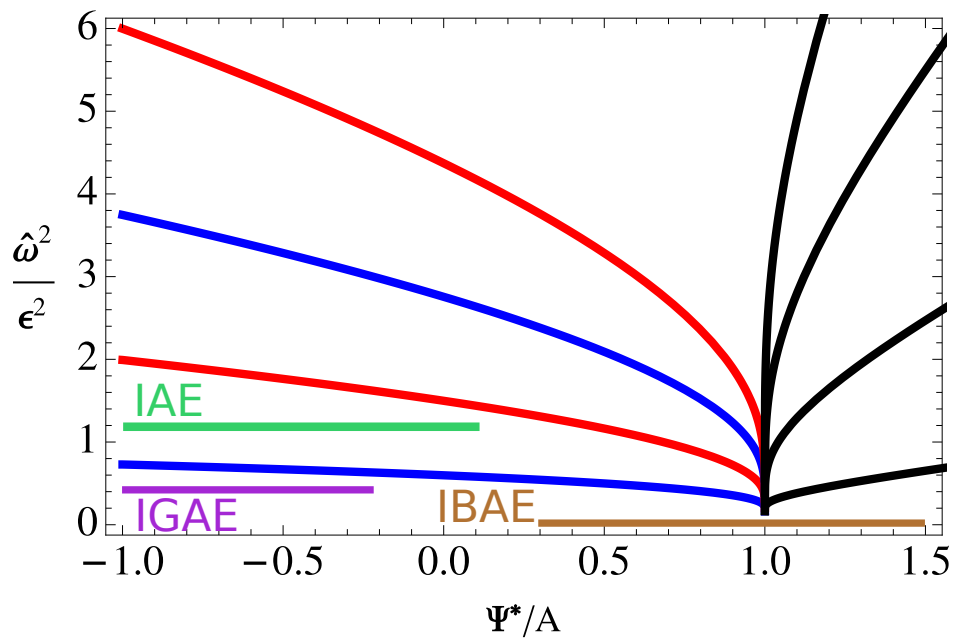


Figure 6.10 Schematic of the radial extent and frequency range of the Island-induced Alfvén Eigenmode (IAE), the Island-induced Global Alfvén Eigenmode (IGAE), and the Island-upshifted Beta-induced Alfvén Eigenmode (IBAE), along with the Alfvén continua in the presence of an island from theory.

Chapter 7

Conclusions and future work

In this dissertation, the shear Alfvén continua and discrete Alfvén eigenmodes in the presence of a magnetic island have been studied both analytically and numerically. A global dispersion relation for the Alfvén continuum valid both inside and outside the island was found analytically for the first time. A new type of Alfvén instability, christened here the Island-induced Alfvén Eigenmode or IAE was shown numerically to exist in the core of an island using the new SIESTAAlfvén code. A previously unexplained Alfvénic instability on the Madison Symmetric Torus (MST) RFP has been identified as the first experimental observation of an IAE.

In Chapter 2, the shear Alfvén continuum was studied analytically in the presence of a magnetic island. A magnetic island coordinate system was employed in the ideal MHD equations, allowing the magnetic field to be represented in straight field-line form throughout the domain, inside and outside the island. The Alfvén continuum wave equation was solved using a WKB expansion in the small parameter $\delta = \Omega/\hat{\omega} \sim \epsilon$, where Ω is the island rotational transform, $\hat{\omega}$ is the normalized eigenfrequency, and $\epsilon = q'_0 w/2$ is the normalized island half-width. Through WKB analysis, the solution for the continuum modes and frequencies was found analytically for the first time for surfaces both inside and outside the island. The continuum frequencies computed can be written in a closed-form dispersion relation, valid on any flux surface:

$$\hat{\omega}^2 = \left[\frac{j\Omega}{2} + \sqrt{\left(\frac{j\Omega}{2}\right)^2 + \frac{q'_0}{2} \left(\Psi^* - \frac{1}{2}\Omega\Phi^*\right)} \right]^2. \quad (2.46)$$

The minimum frequency of the continuous spectrum moves from the resonant, rational surface in the absence of an island to the separatrix when an island is present. Additionally the frequency

is upshifted at the separatrix, resulting in the following new minimum frequency:

$$\omega_{sep}^2 = \omega_{BAE}^2 + (q'_0 w)^2 \omega_A^2 / 32. \quad (3.11)$$

This is the first time this separatrix frequency has been derived analytically. After transforming to the proper coordinates, this is the same frequency upshift found numerically by Biancalani [12]. The analytic solution presented in this thesis also handles the boundary conditions within the magnetic island properly. In Biancalani's shooting method code approach, solutions with odd and even parity were included for all values of j_{in} . Our work here identifies that the solutions are restricted to odd parity for odd j_{in} and even parity for even j_{in} .

In Chapter 3, the shear Alfvén continuum derived in Chapter 2 was used to compute the continua for MST parameters and the $n_0 = 5$ island identified from experiment. Using the equation for the continuum at the O-point of the magnetic island,

$$f = \sqrt{f_{BAE}^2 + \frac{n_0^2 j_{in} (j_{in} + 2)}{4} \epsilon^2 k_{\parallel}^2 v_A^2}, \quad (3.9)$$

the lowest two continuum branches for $j_{in} = 1$ and $j_{in} = 2$ in the core of the island were shown to envelope the observed $n = 4$ Alfvénic bursts in Fig. 3.7. Thus the experimental $n = 4$ Alfvénic activity is consistent with a gap mode located in the core of the island. The continuum theory was also used to explain BAE activity observed during tearing mode activity on the EAST and FTU tokamaks. The island-induced continuum upshift explains the high discrete BAE (or Island-upshifted BAE, IBAE) frequencies observed on EAST.

Previous numerical investigations of the continua using STELLGAP had neglected the core island and failed to identify gaps that could explain the observed AEs. With the theoretical island continua from Chapter 3 sandwiching observations as motivation, a new attempt at STELLGAP and AE3D computations was detailed in Chapter 4. The island was modeled as the $n_0 = 5$ helical core of a Single Helical Axis (SHAx) equilibrium in VMEC, and STELLGAP and AE3D were run using this configuration. The SHAx state retains the essential helical couplings present in the island core, but does not contain a separatrix and both magnetic axes. The computed continua from STELLGAP contain a sizable gap in the "island" core, with frequencies consistent with those

from theory. The gap coupling found is $m = 1, n = 4$ and $m = 0, n = -1$, consistent with the $\delta n = 5$ coupling for the helical core. Using the AE3D code for discrete modes, a helicity-induced Alfvén eigenmode (HAE) was found in the frequency gap. The mode is characterized by strong $m = 1, n = 4$ and $m = 0, n = -1$ components, as expected from the island-induced gap and agreeing with the $m = 1, n = 4$ mode numbers measured experimentally. The 149 kHz frequency also agrees with observations on MST.

In Chapter 5, a new tool to calculate shear Alfvén eigenmodes in the presence of a magnetic island was introduced. The novel SIESTAAlfvén code was built as a post-processing step to the SIESTA equilibrium code, which computes ideal MHD equilibria containing magnetic islands. SIESTAAlfvén computes an inertia matrix \tilde{T}_{ij} along with the Hessian matrix \tilde{H}_{ij} from SIESTA and solves the generalized eigenvalue problem $-\omega^2 \tilde{T}_{ij} \xi^j = \tilde{H}_{ij} \xi^j$. The solutions are the full MHD eigenmodes, including the shear Alfvén modes of interest. The SIESTAAlfvén code was benchmarked against the AE3D code for a TAE test case with no islands, and good agreement was found.

In Chapter 6, an MST configuration with an $n_0 = 5$ island was modeled in SIESTA, and the SIESTAAlfvén code was used to study the MHD modes of the resulting equilibrium. An Island-induced Alfvén Eigenmode (IAE) was found at 145 kHz, consistent with the 140 – 160 kHz from experiment. The IAE is localized to the core of the island, and is dominated by $n = 4$ and $n = -1$ Fourier modes as expected from the $\delta n = 5$ island coupling. The $n = 4$ Alfvénic activity on MST is believed to be the first experimental observation of this new IAE.

Additional, unexplained $n = -1$ activity has been observed on MST at approximately 65 kHz. An $n = -1$ Island-induced Global Alfvén Eigenmode (IGAE) has been discovered with the AE3D code. This mode exists in the core of the island below the lowest continuum branch. The 76 kHz mode is in reasonable agreement with the observed frequency and may explain the $n = -1$ activity observed on MST. Further experimental probing of the $n = -1$ mode is needed in order to determine whether it scales with the Alfvén speed and to confirm the frequency. However based on current experimental measurements, the IGAE appears to be a likely candidate for this instability on MST.

The identification of three different Alfvén eigenmodes modified or created by an island in this thesis leads to an interesting question: Does the whole Alfvén zoo exist in the island? The IAE is caused from the helicity of the island, analogously to an HAE. The IGAE is a global AE restricted to the core of the island and is similar in nature to a GAE or RSAE (reversed-shear). The IBAE is a BAE upshifted by the island. Since the island counterparts of three of the well-known AEs have been identified in this thesis, it may very well be that the “whole zoo is on the island”, and Island-induced TAEs, Island-induced EAEs, and Island-induced MAEs also exist. The island does contain a separatrix, after all, and is in a very real way a stellarator embedded in another topology. It seems reasonable that island versions of the Alfvén eigenmodes present in a stellarator could all exist, possibly with interesting characteristics and couplings due to the larger device in which the island exists.

As the fusion community looks forward to ITER and the future, Alfvén instabilities become even more important. The energetic α -particles produced in ITER (or a fusion reactor) will provide a strong destabilizing drive for AEs. In ITER the α speed will be comparable to the Alfvén speed, $v_A < v_\alpha < 2v_A$ [1], leading to a strong resonance between energetic particles and Alfvén modes. An Island-induced Alfvén Eigenmode (IAE) instability has been shown to exist in MST during neutral beam injection. The stronger energetic particle drive may make this type of instability even more problematic for high temperature, fusion-relevant plasmas containing islands. Because of this, the discovery of the IAE in MST and the description of the IAE in this thesis may serve as a word of caution toward planned islands in experiment. The presence of an IAE instability in an island could compound problems from neoclassical tearing modes evolving during the discharge. Island divertors, such as those in Wendelstein 7-X, and resonant magnetic perturbations (RMPs) for mitigating edge-localized modes (ELMs) in tokamaks both utilize islands to maintain or control confinement. While these concepts may accomplish their intended tasks and may very well prove necessary, they may also open the door to the new types of island-induced Alfvénic instabilities described in this dissertation.

Future work

There are many different research directions that can build on this work on the Alfvén spectrum in the presence of islands. Everything presented in this thesis was based on the ideal MHD model. Because the energetic particle drive is crucial in determining the growth rate of Alfvén modes, the current MHD model is only able to predict the mode frequency, but not the growth rate. A proper kinetic treatment that incorporates finite Larmor radius effects is necessary to determine the growth rate of these instabilities, which could then be compared to experimental measurements on MST. Some work has been done using kinetic theory to determine the growth rate and instability mechanism of an island-modified BAE mode [64]. A similar analysis could in principle be investigated for the IAE found here. Betti and Freidberg have a generalized kinetic analysis for the growth rate of Alfvén eigenmodes [65]. They find that the growth rate is determined by the competing energetic alpha particle drive and the electron and ion Landau damping.

The growth rate problem could also be studied computationally using gyrokinetic or gyro-fluid codes. Most of the current codes, such as the gyrokinetic codes EUTERPE, GENE, GYRO, and GTC [66, 67, 68] and the gyrofluid code TAEFL [69], operate in simplified geometries (some simply flux tubes) and would need modifications to run on the complex three-dimensional geometry of an island embedded in a larger equilibrium. These types of codes could be an invaluable tool for understanding plasma kinetic effects and drives for Alfvén instabilities if adopted to more flexible geometries. Recently Don Spong has added the ability to use a VMEC equilibrium to initialize the Gyrokinetic Toroidal Code (GTC). This is a large first step, since a 3D MHD equilibrium can now be used instead of the simple 2D Grad-Shafranov EFIT equilibria used previously. In the future, if SIESTA equilibria could be used to initialize GTC, the EP-Alfvén wave interactions could be studied numerically in the presence of an island. From this the growth rate of the IAE could be calculated.

Because SIESTA Alfvén includes finite compressibility $\nabla \cdot \xi \neq 0$, it could be interesting to see an analytic theory for the Alfvén continuum with finite plasma wave compressibility. A compressional theory would allow the shear Alfvén wave to couple to the acoustic wave, which can lead to

compressional Alfvén waves (CAWs) and beta-induced Alfvén-acoustic eigenmodes (BAAEs). In these modes, the wave polarization contains an additional ξ_{\parallel} component in addition to the normal shear Alfvén ξ_{\perp} component. The effects of Alfvén-acoustic couplings on the Alfvén continua in an island remains an open question.

The shear Alfvén continuum analysis of Chapter 2 was performed for waves of the same helicity as the magnetic island, that is $l = 0$. The $l \neq 0$ case would further generalize the theory. Secondary resonances are expected for these modes inside the island at surfaces of rational island rotational transform Ω , where $l_0 - j_0\Omega = 0$.

The SIESTAAlfvén code currently is able to compute discrete AEs with a finite radial extent in the plasma. However, it does not resolve the continuum modes to a satisfactory level to compute the shear Alfvén continua as STELLGAP does for VMEC equilibria. One proposed method for accurately obtaining these continuum frequencies is to use the individual blocks from the SIESTA Hessian matrix \tilde{H}_{ij} . The blocks correspond to a single surface, so solving the diagonal blocks one at a time would remove the cross-surface coupling and could provide the appropriate continuum frequencies. The difficulty here is that the surfaces are in terms of the VMEC radial coordinate s , and thus do not correspond to physical magnetic flux surfaces once an island is formed in SIESTA. The coordinate surfaces are drastically different from the flux surfaces inside the magnetic island and in the surrounding region. A reformulation of the Hessian matrix blocks in terms of the flux surfaces obtained from the pressure profile with an island may be one method that could be used to properly compute the Alfvén continuum from SIESTA.

Analytically, there are several other interesting directions that could be pursued. First, this thesis employed analytic theory for the Alfvén continuum, and left the computation of discrete AEs exclusively to numerical simulation using AE3D and SIESTAAlfvén. Direct analysis of global modes using ideal MHD is extremely complicated, but it may be possible to make some analytic progress on the discrete modes through a reduced MHD formulation [21]. Analytic theory analogous to the work of Cheng and Chance for the TAE mode may prove useful [16], albeit the geometry will be much more complicated for the island case of interest than the large aspect-ratio, two-dimensional tokamak equilibrium studied there.

A resistive MHD treatment of the Alfvén spectrum may also be an interesting topic. If the island is allowed to grow or shrink by pulling energy from the Alfvén wave, this may lead to a better understanding of the dynamics of island evolution in the presence of strong particle-drive. The nonlinear interaction and energy transfer between Alfvén instabilities and tearing modes is an interesting topic that is ripe for investigation.

Finally this dissertation investigated IAEs in an island in MST, an RFP. The geometry of an island in a circular RFP is much less complicated and involves less potential couplings than an island in a stellarator or a 3D tokamak with considerable shaping. A helical stellarator containing a helical island with different m_0 and n_0 numbers from the device is a very interesting configuration, and the resulting IAEs and couplings could be quite different in character than the IAE in an RFP studied in this thesis. These could be of practical importance, due to the presence of island divertors on the Wendelstein 7-X stellarator [70]. The SIESTA_{Alfvén} tools described in this thesis could be used to investigate IAEs in stellarators with islands, such as Wendelstein 7-X.

APPENDICES

Appendix A: C, D, E, and F matrix operators

The following are the C , D , E , and F matrix operators from Cheng and Chance's derivation of the Alfvén continuum in a toroidal equilibrium [16]. The operators can be generalized to equilibria containing magnetic islands by replacing the poloidal flux ψ with the helical flux Φ^* :

$$C_{11} = \kappa_\psi, \quad (\text{A.1})$$

$$C_{12} = \omega^2 \rho + p' \kappa_\psi + |\nabla \psi|^2 \mathbf{B} \cdot \nabla (|\nabla \psi|^{-2} \mathbf{B} \cdot \nabla) + (\mathbf{B} \cdot \mathbf{J} - \hat{s} |\nabla \psi|^2) (\hat{s} |\nabla \psi|^2 / B^2) \quad (\text{A.2})$$

$$C_{21} = 0, \quad (\text{A.3})$$

$$C_{22} = -|\nabla \psi|^2 \nabla \cdot (\nabla \psi / |\nabla \psi|^2), \quad (\text{A.4})$$

$$D_{11} = (|\nabla \psi|^2 \hat{s} - \mathbf{B} \cdot \mathbf{J}) (|\nabla \psi|^2 / B^2) \mathbf{B} \cdot \nabla, \quad (\text{A.5})$$

$$D_{12} = \gamma p \kappa_\psi, \quad (\text{A.6})$$

$$D_{21} = |\nabla \psi|^2 \left[\kappa_s - (\mathbf{B} \times \nabla \psi) / B^2 \cdot \nabla \right], \quad (\text{A.7})$$

$$D_{22} = |\nabla \psi|^2 \left[1 + \frac{\gamma p}{\omega^2 \rho} \mathbf{B} \cdot \nabla \left(\frac{\mathbf{B} \cdot \nabla}{B^2} \right) \right], \quad (\text{A.8})$$

$$E_{11} = \frac{\omega^2 \rho |\nabla \psi|^2}{B^2} + \mathbf{B} \cdot \nabla \left(\frac{|\nabla \psi|^2 \mathbf{B} \cdot \nabla}{B^2} \right), \quad (\text{A.9})$$

$$E_{12} = \gamma p \kappa_s, \quad (\text{A.10})$$

$$E_{21} = \kappa_s, \quad (\text{A.11})$$

$$E_{22} = \frac{\gamma p + B^2}{B^2} + \frac{\gamma p}{\omega^2 \rho} \mathbf{B} \cdot \nabla \left(\frac{\mathbf{B} \cdot \nabla}{B^2} \right), \quad (\text{A.12})$$

$$F_{11} = -\kappa_s + (\mathbf{B} \times \nabla \psi) / B^2 \cdot \nabla, \quad (\text{A.13})$$

$$F_{12} = \mathbf{B} \cdot \nabla (|\nabla \psi|^2 / B^2) \hat{s} - [(\mathbf{J} \cdot \mathbf{B}) / B^2] \mathbf{B} \cdot \nabla - p' \kappa_s, \quad (\text{A.14})$$

$$F_{21} = -1 / B^2, \quad (\text{A.15})$$

$$F_{22} = -\kappa_\psi / |\nabla \psi|^2. \quad (\text{A.16})$$

Here $\kappa = (\mathbf{B}/B) \cdot \nabla (\mathbf{B}/B)$, $\kappa_\psi = 2\kappa \cdot \nabla \psi$, and $\kappa_s = 2\kappa \cdot (\mathbf{B} \times \nabla \psi / B^2)$ are the curvature terms. $\hat{s} = (\mathbf{B} \times \nabla \psi / |\nabla \psi|^2) \cdot \nabla \times [(\mathbf{B} \times \nabla \psi) / |\nabla \psi|^2]$ is the negative local magnetic shear.

Appendix B: Island rotational transform inside separatrix

Beginning with the helical flux function Ψ^* from Hegna and Callen's paper [28], defined as

$$\Psi^* = \int (q - q_0) d\psi - A \cos(n_0\alpha) \approx q'_0 \frac{x^2}{2} - A \cos(n_0\alpha), \quad (\text{B.1})$$

the island rotational transform $\Omega(\Psi^*)$ within the island separatrix will be derived. Here $q'_0 = \left. \frac{dq}{d\psi} \right|_{\psi=\psi_0}$ and $x = \psi - \psi_0$. A characterizes the ‘‘amplitude’’ of the magnetic island and $\alpha = \zeta - q_0\theta + \frac{\phi_0}{n_0}$ with $q_0 = \frac{m_0}{n_0}$. The island width in flux space will be used during the derivation as well. This is given by

$$w = 4\sqrt{\left| \frac{A}{q'_0} \right|}. \quad (\text{B.2})$$

The island rotational transform is given by the following expression:

$$\Omega(\Psi^*) = \frac{1}{\oint \left(\frac{n_0 d\alpha}{2\pi} \right) \left[1 / \frac{\partial \Psi^*}{\partial x} \right]}. \quad (\text{B.3})$$

From the approximate helical flux in Equation B.1 one can derive

$$\frac{\partial \Psi^*}{\partial x} = \sqrt{2q'_0(\Psi^* + A \cos(n_0\alpha))}. \quad (\text{B.4})$$

Substituting this into Equation B.3 and setting $a = n_0\alpha$ yields

$$\Omega(\Psi^*) = \frac{1}{\oint \left(\frac{da}{2\pi} \right) \frac{1}{\sqrt{2q'_0(\Psi^* + A \cos a)}}}. \quad (\text{B.5})$$

The closed integral in the denominator is evaluated from a_{min} to a_{max} and back again on a helical flux surface. Since $\frac{\partial \Psi^*}{\partial x}$ switches signs across the rational surface, the closed integral is equal to twice the integral from a_{min} to a_{max} . Using the trig identity $\cos a = 1 - 2 \sin^2 \left(\frac{a}{2} \right)$ in Equation B.5 results in the following equation:

$$\Omega(\Psi^*) = \frac{1}{\int_{a_{min}}^{a_{max}} \left(\frac{da}{\pi} \right) \frac{1}{\sqrt{2q'_0(\Psi^* + A - 2A \sin^2(\frac{a}{2}))}}}. \quad (\text{B.6})$$

Setting $\kappa^2 = \frac{\Psi^* + A}{2A}$, this can be rewritten as

$$\Omega(\Psi^*) = \frac{\pi q'_0 w}{2 \int_{a_{min}}^{a_{max}} \frac{da}{\sqrt{\kappa^2 - \sin^2(\frac{a}{2})}}}. \quad (\text{B.7})$$

It can easily be shown that $a_{min} = -a_{max}$, and since the integral is an even function in a we can double the integral from 0 to a_{max} . Next the substitution $u = \frac{a}{2}$ brings out another factor of 2, resulting in

$$\Omega(\Psi^*) = \frac{\pi q'_0 w}{8 \int_0^{a_{max}/2} \frac{du}{\sqrt{\kappa^2 - \sin^2 u}}}. \quad (\text{B.8})$$

Then one more substitution with $\sin u = \kappa \sin y$ gives the following expression after simplification:

$$\Omega(\Psi^*) = \frac{\pi q'_0 w}{8 \int_0^{\pi/2} \frac{dy}{\sqrt{1 - \kappa^2 \sin^2 y}}}. \quad (\text{B.9})$$

But this is just the complete elliptic integral of the first kind K in terms of κ . Thus the desired expression for the island rotational transform inside the separatrix is given by

$$\Omega(\Psi^*) = \frac{\pi q'_0 w}{8K(\kappa^2)}, \quad (\text{B.10})$$

$$\kappa^2 = \frac{\Psi^* + A}{2A}. \quad (\text{B.11})$$

This can be compared to the corresponding expression for Ω for surfaces outside the separatrix given by Hegna [29]:

$$\Omega(\Psi^*) = \pm \frac{\pi q'_0 w}{4kK(k^2)}, \quad (\text{B.12})$$

$$k^2 = \frac{2A}{\Psi^* + A}. \quad (\text{B.13})$$

Appendix C: Island coordinates

The island coordinates outside the separatrix are given by

$$\Phi^* = \pm \frac{w}{\pi k} E(k^2), \quad (\text{C.1})$$

$$\alpha^* = \frac{\pi}{n_0 K(k^2)} F\left(\frac{n_0 \alpha}{2}, k^2\right), \quad (\text{C.2})$$

where $K(k^2)$ and $E(k^2)$ are the complete elliptic integrals of the first and second kind, respectively, and $F(n_0 \alpha/2, k^2)$ is the incomplete elliptic integral of the first kind.

Inside the separatrix, we have

$$\Phi^* = \frac{2w}{\pi} [E(\kappa^2) + (\kappa^2 - 1)K(\kappa^2)], \quad (\text{C.3})$$

$$\alpha^* = \frac{\pi}{2n_0 K(\kappa^2)} F\left(\sin^{-1}\left[\frac{1}{\kappa} \sin \frac{n_0 \alpha}{2}\right], \kappa^2\right). \quad (\text{C.4})$$

In terms of α^* , x outside and inside the separatrix, respectively, can be written as

$$\hat{x} = \sqrt{\frac{1}{k^2} - sn^2\left[\frac{n_0 K(k^2)}{\pi} \alpha^*, k^2\right]}, \quad (\text{C.5})$$

$$\hat{x} = \kappa cn\left[\frac{2n_0 K(\kappa^2)}{\pi} \alpha^*, \kappa^2\right]. \quad (\text{C.6})$$

Here, sn and cn are the Jacobi elliptic functions.

S_2 from the WKB expansion takes the following form, outside and inside the separatrix:

$$S_2 = \pm \frac{i\epsilon}{4k\Omega} \left[(k^2 - 2) \frac{K(k^2)}{\pi} \alpha^* + 2E\left(am\left[\frac{K(k^2)}{\pi} \alpha^*, k^2\right], k^2\right) \right], \quad (\text{C.7})$$

$$S_2 = \pm \frac{i\epsilon}{8\Omega} \left[-\frac{4K(\kappa^2)}{\pi} \alpha^* + 4E\left(am\left[\frac{2K(\kappa^2)}{\pi} \alpha^*, \kappa^2\right], \kappa^2\right) \right]. \quad (\text{C.8})$$

In these expressions, am is the Jacobi amplitude and $E(\cdot, k^2)$ is the incomplete elliptic integral of the second kind.

Appendix D: Translation to Biancalani's notation

This appendix details the conversion of Biancalani's island coordinate system formulation in [10, 11, 12] to the coordinates and notation used in this thesis. Some trivial relations with Biancalani's variable given on the left and our variable given on the right are

$$\theta_T = \theta, \quad (\text{D.1})$$

$$\zeta_T = \zeta, \quad (\text{D.2})$$

$$q_T = q, \quad (\text{D.3})$$

$$r_T \sim \psi, \quad (\text{D.4})$$

$$r_0 \sim \psi_0. \quad (\text{D.5})$$

In order to compare Biancalani's flux surface label ψ (which will be referred to as ψ_B to avoid confusion) with the helical flux function Ψ^* used here, several other variables need to be translated. The u coordinate from Biancalani works out to be

$$u = n_0\alpha - \phi_0. \quad (\text{D.6})$$

The M constant tearing mode amplitude from Biancalani can be written in terms of the variables from this thesis as

$$M = \frac{q'_0 A}{2} = \frac{(q'_0 w)^2}{32}. \quad (\text{D.7})$$

Finally, the definition for magnetic shear that will be used for this translation is

$$s = \frac{2\psi_0}{q_0} q'_0. \quad (\text{D.8})$$

Using Eqs. D.6, D.7, and D.8, ψ_B and Ψ^* can be related in terms of our notation:

$$\psi_B = \frac{(q - q_0)^2}{2} + \frac{q'_0 A}{2} [\cos(n_0\alpha - \phi_0) + 1], \quad (\text{D.9})$$

$$\Psi^* = \frac{q'_0}{2} (\psi - \psi_0)^2 - A \cos(n_0\alpha). \quad (\text{D.10})$$

It should be noted that while Ψ^* has units of magnetic flux, ψ_B is dimensionless. The safety factor outside the island can be converted to the notation of this thesis through the following expressions

for Biancalani's x (referred to here as x_B to avoid overlap with our x) and e :

$$x_B = \frac{1}{4} \sqrt{\frac{\psi_B}{2q'_0 A}}, \quad (\text{D.11})$$

$$1 - e = \left(\frac{q_0 \gamma n_0 w}{2\psi_0} \right)^2. \quad (\text{D.12})$$

Here $\gamma = \sqrt{1 + \left(\frac{r_0}{R_0 q_0} \right)^2}$. Setting $e = 1$ (approximately correct for typical islands in tokamaks), the safety factor outside the island q_{out} , from Biancalani can be compared to the rotational transform outside the island Ω_{out} , from Chapter 2:

$$q_{out} = \frac{1}{2\pi n_0} \int_0^{2\pi q_0 n_0} \frac{du}{1 - \sqrt{\frac{2}{q_0^2} [\psi_B - 16q'_0 A (\cos u + 1)]}}, \quad (\text{D.13})$$

$$\frac{1}{\Omega_{out}} = \frac{n_0}{2\pi} \oint \frac{d\alpha}{\sqrt{2q'_0 [\Psi^* + A \cos(n_0 \alpha)]}}. \quad (\text{D.14})$$

The simplified formula for q_{in} inside the island given by Biancalani can be compared to the equivalent expression for Ω_{in} derived in Appendix B. Both are written in terms of the complete elliptic integral of the first kind, K , one with argument x_B defined above and one with argument

$$\kappa = \sqrt{\frac{\Psi^* + A}{2A}}:$$

$$q_{in} = \frac{2}{\pi q'_0 w n_0} K(x_B^2), \quad (\text{D.15})$$

$$\frac{1}{\Omega_{in}} = \frac{8}{\pi q'_0 w} K(\kappa^2). \quad (\text{D.16})$$

Appendix E: Boozer-Xform modifications for RFPs

VMEC and the Boozer-Xform code, which performs a transformation from VMEC coordinates to Boozer coordinates, both utilize toroidal flux Φ , as the radial variable. For RFPs containing a reversal surface, toroidal flux does not work as a surface label since $B^\zeta = 0$ on a surface within the plasma. Due to this, toroidal flux is not a single-valued function of the flux surface radius.

Poloidal flux should instead be used for RFPs with a reversal surface (or indeed for all configurations to avoid confusion). VMEC has been modified by S. P. Hirshman in the past to accommodate poloidal flux, and the Boozer-Xform code was modified by the author during the course of the work for this dissertation.

The magnetic field in Boozer coordinates is generally written in terms of the toroidal flux, Φ , as follows:

$$\mathbf{B} = \nabla\Phi \times \nabla\theta + \iota\nabla\zeta \times \nabla\Phi. \quad (\text{E.1})$$

Boozer coordinates also give a particularly simple covariant representation of \mathbf{B} :

$$\mathbf{B} = g\nabla\zeta + I\nabla\theta + \nu\nabla\Phi. \quad (\text{E.2})$$

Using the two representations, it can easily be seen that the Jacobian of the transformation from (Φ, θ, ζ) to cylindrical coordinates is given by

$$\sqrt{g_\Phi} = \frac{g + \iota I}{B^2}. \quad (\text{E.3})$$

The contravariant representation of the field given above can be rewritten in terms of χ , the poloidal flux, using $\iota = \frac{d\chi}{d\Phi}$:

$$\mathbf{B} = \frac{1}{\iota}\nabla\chi \times \nabla\theta + \nabla\zeta \times \nabla\chi. \quad (\text{E.4})$$

The magnetic field still has a nice covariant representation with the new coordinate χ :

$$\mathbf{B} = g\nabla\zeta + I\nabla\theta + \frac{\nu}{\iota}\nabla\chi. \quad (\text{E.5})$$

The Jacobian of the transformation from (χ, θ, ζ) to cylindrical coordinates can again be obtained from the covariant and contravariant representations, resulting in

$$\sqrt{g_\chi} = \frac{g/\iota + I}{B^2}. \quad (\text{E.6})$$

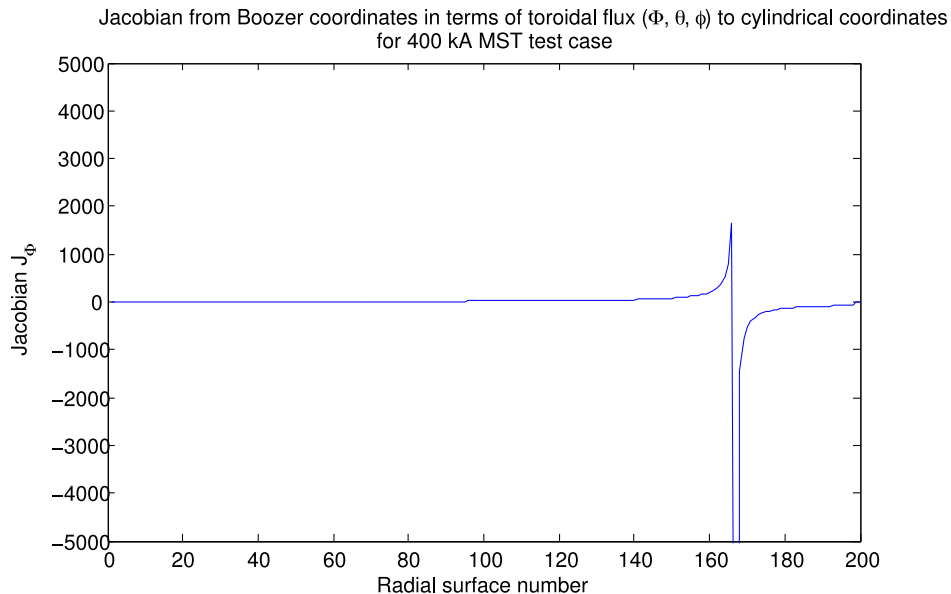


Figure E.1 Toroidal flux Jacobian vs. radius from old Boozer-Xform code. The Jacobian is singular at the reversal surface.

Thus there is a very simple relationship between the Jacobian of Boozer coordinates using poloidal flux χ and the Jacobian of Boozer coordinates using toroidal flux Φ . This relation can be written as

$$\sqrt{g_\chi} = \frac{1}{\iota} \sqrt{g_\Phi}. \quad (\text{E.7})$$

Since $\iota \rightarrow \infty$ at the reversal surface in an RFP, the Jacobian in terms of Φ is singular at the reversal surface, that is $\sqrt{g_\Phi} \rightarrow \infty$. However, the Jacobian of Boozer coordinates in terms of χ , $\sqrt{g_\chi}$ remains analytic across the reversal surface. This behavior can be seen in the output of Boozer-Xform for an MST test-case in Figs. E.1 and E.2. In Fig. E.1, the singular behavior of $\sqrt{g_\Phi}$ at the reversal surface can be seen. In contrast Fig. E.2 displays the Jacobian obtained from the modified version of Boozer-Xform and $\sqrt{g_\chi}$ is clearly analytic throughout the domain.

Combining these modifications to Boozer-Xform with the modifications made to STELLGAP by Don Spong allows STELLGAP to be used for RFPs with a reversal surface. Figs. E.3 and E.4 show STELLGAP simulation results for MST with a reversal surface before and after the fixes, respectively. Notice that the singularity problem at the reversal surface has been resolved with the changes to the codes.

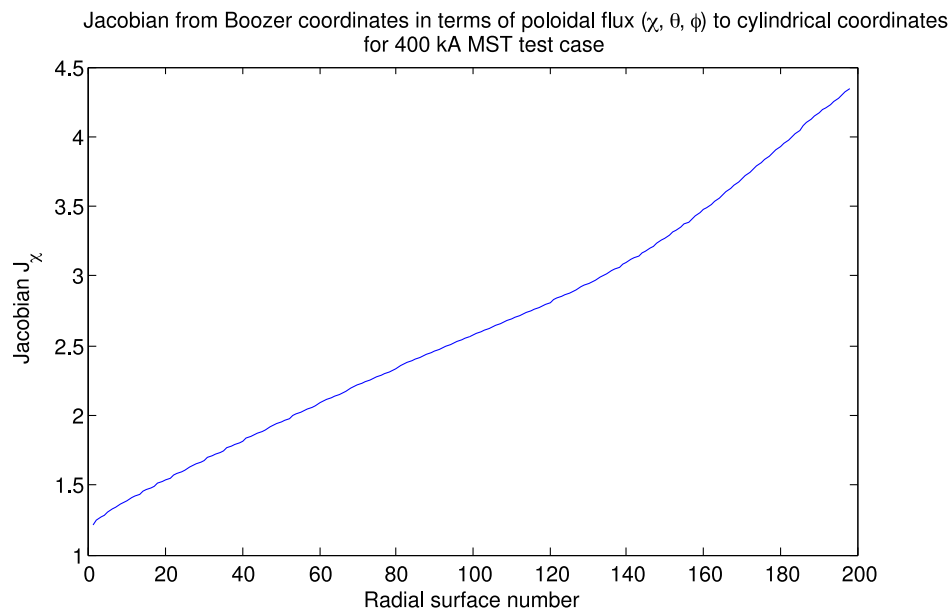
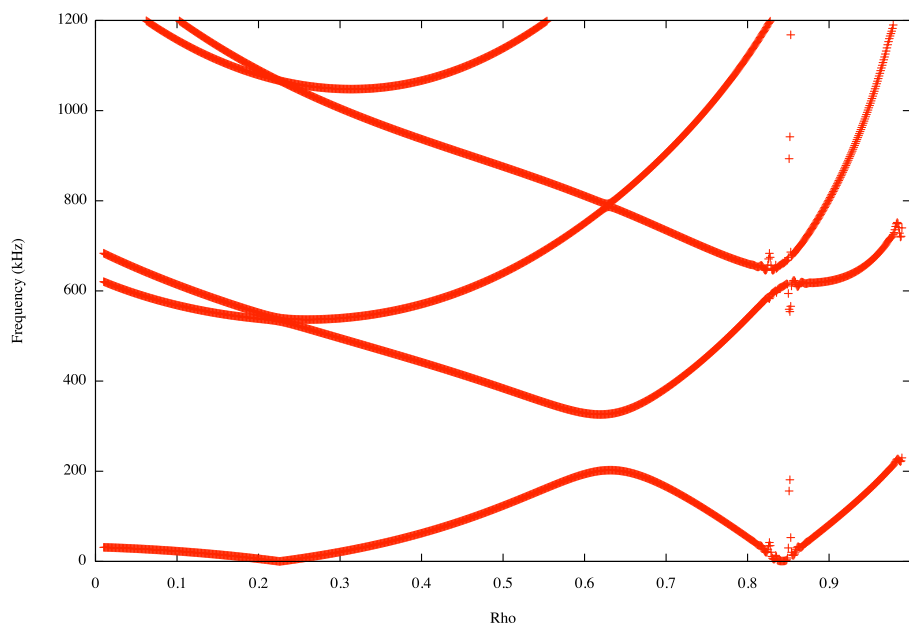
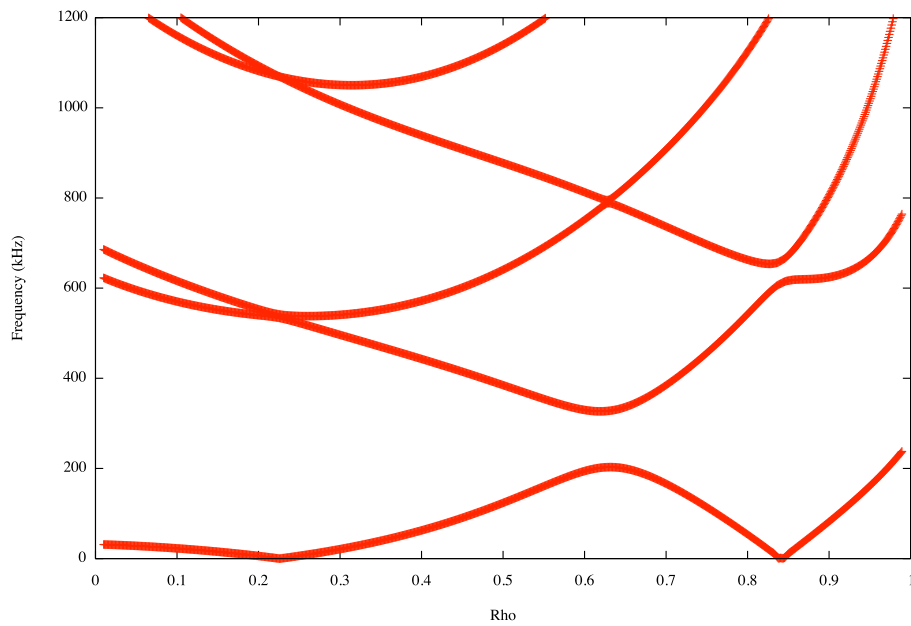


Figure E.2 Poloidal flux Jacobian vs. radius from modified Boozer-Xform code. The Jacobian remains analytic across the reversal surface.



Mon Feb 25 15:22:26 2013

Figure E.3 STELLGAP continuum results for an MST equilibrium with a reversal surface at $\rho = 0.85$ prior to Boozer-Xform and STELLGAP modifications. There is a singularity problem at the reversal surface. Figure from Don Spong.



Mon Feb 25 15:03:54 2013

Figure E.4 STELLGAP continuum results for an MST equilibrium with a reversal surface at $\rho = 0.85$ after Boozer-Xform and STELLGAP modifications have been implemented. There is no longer an issue at the reversal surface. Figure from Don Spong.

BIBLIOGRAPHY

- [1] N. N. Gorelenkov *et al.*, Phys. Plasmas **11**, 2586 (2004).
- [2] F. Zonca and L. Chen, Phys. Plasmas **21** (2014).
- [3] F. Zonca and L. Chen, Phys. Plasmas **21** (2014).
- [4] J. Koliner *et al.*, Phys. Rev. Lett. **109**, 115003 (2012).
- [5] D. A. Spong, E. DAzevedo, and Y. Todo, Phys. Plasmas **17**, 022106 (2010).
- [6] M. Xu *et al.*, Plasma Phys. Control. Fusion **55**, 065002 (2013).
- [7] P. Buratti *et al.*, Nucl. Fusion **45**, 1446 (2005).
- [8] S. V. Annibaldi, F. Zonca, and P. Buratti, Plasma Phys. Control. Fusion **49**, 475 (2007).
- [9] O. Zimmermann *et al.*, Proc. 32nd EPS Conf. Plasma Physics, Tarragona, Spain **29C**, P4.059 (2005).
- [10] A. Biancalani, L. Chen, F. Pegoraro, and F. Zonca, Phys. Plasmas **17**, 122106 (2010).
- [11] A. Biancalani, L. Chen, F. Pegoraro, and F. Zonca, Phys. Rev. Lett. **105**, 1 (2010).
- [12] A. Biancalani, L. Chen, F. Pegoraro, and F. Zonca, Plasma Phys. Control. Fusion **53**, 025009 (2011).
- [13] H. Alfvén, Nature **150**, 405 (1942).
- [14] W. W. Heidbrink, Phys. Plasmas **15**, 1 (2008).
- [15] J. Wesson, *Tokamaks, Fourth Edition* (Oxford, 2011).
- [16] C. Z. Cheng and M. S. Chance, Phys. Fluids **29**, 3695 (1986).
- [17] D. A. D'Ippolito and J. P. Goebloed, Plasma Phys. **22**, 1091 (1980).
- [18] D. A. D'Ippolito and J. P. Goebloed, Plasma Phys. **25**, 537 (1983).

- [19] J. W. Strutt, *Philos. Mag.* **24**, 145 (1887).
- [20] C. Cheng, L. Chen, and M. Chance, *Ann. Phys. (N. Y.)* **161**, 21 (1985).
- [21] R. Izzo, *Phys. Fluids* **26**, 2240 (1983).
- [22] S. E. Kruger, C. C. Hegna, and J. D. Callen, *Phys. Plasmas* **5**, 4169 (1998).
- [23] Y. I. Kolesnichenko, V. V. Lutsenko, H. Wobig, Y. V. Yakovenko, and O. P. Fesenyuk, *Phys. Plasmas* **8**, 491 (2001).
- [24] A. Fasoli and J. Lister, *Nucl. Fusion* **35**, 1485 (1995).
- [25] K. Toi *et al.*, *Nucl. Fusion* **44**, 217 (2004).
- [26] W. W. Heidbrink, E. J. Strait, M. S. Chu, and A. D. Turnbull, *Phys. Rev. Lett.* **71**, 855 (1993).
- [27] K. Wong *et al.*, *Phys. Rev. Lett.* **66**, 1874 (1991).
- [28] C. C. Hegna and J. D. Callen, *Phys. Fluids B Plasma Phys.* **4**, 3031 (1992).
- [29] C. C. Hegna, *Plasma Phys. Control. Fusion* **53**, 024003 (2011).
- [30] P. H. Rutherford, *Phys. Fluids* **16**, 1903 (1973).
- [31] J. R. Cary and R. G. Littlejohn, *Ann. Phys. (N. Y.)* **151**, 1 (1983).
- [32] M. S. Chu, J. M. Greene, L. L. Lao, A. D. Turnbull, and M. S. Chance, *Phys. Fluids B Plasma Phys.* **4**, 3713 (1992).
- [33] A. D. Turnbull *et al.*, *Phys. Fluids B Plasma Phys.* **5**, 2546 (1993).
- [34] C. R. Cook and C. C. Hegna, *Phys. Plasmas* **22**, 042517 (2015).
- [35] R. N. Dexter, D. W. Kerst, T. W. Lovell, S. C. Prager, and J. C. Sprott, *Fusion Technol.* **19**, 131 (1991).
- [36] J. J. Koliner, “Neutral Beam Excitation of Alfvén Continua in the Madison Symmetric Torus Reversed Field Pinch”, PhD thesis, University of Wisconsin (2013).
- [37] J. K. Anderson *et al.*, *Fusion Sci. Technol.* **59**, 27 (2011).
- [38] S. P. Hirshman and J. C. Whitson, *Phys. Fluids* **26**, 3553 (1983).
- [39] S. P. Hirshman and H. K. Meier, *Phys. Fluids* **28**, 1387 (1985).
- [40] D. A. Spong, R. Sanchez, and A. Weller, *Phys. Plasmas* **10**, 3217 (2003).
- [41] D. A. Spong *et al.*, *Contrib. to Plasma Phys.* **50**, 708 (2010).

- [42] D. C. Robinson, Nucl. Fusion **18**, 939 (1978).
- [43] H. D. Stephens, D. J. Den Hartog, C. C. Hegna, and J. A. Reusch, Phys. Plasmas **17**, 1 (2010).
- [44] T. M. Biewer *et al.*, Phys. Rev. Lett. **91**, 045004 (2003).
- [45] P. Franz *et al.*, Phys. Rev. Lett. **92**, 125001 (2004).
- [46] F. Zonca, L. Chen, and R. a. Santoro, Plasma Phys. Control. Fusion **38**, 2011 (1996).
- [47] P. Buratti *et al.*, Nucl. Fusion **45**, 1446 (2005).
- [48] J. D. Hanson *et al.*, Nucl. Fusion **49**, 075031 (2009).
- [49] A. Salat and J. A. Tataronis, Phys. Plasmas **8**, 1200 (2001).
- [50] A. Salat and J. A. Tataronis, Phys. Plasmas **8**, 1207 (2001).
- [51] A. H. Boozer, Phys. Fluids **24**, 1999 (1981).
- [52] A. H. Boozer, Phys. Fluids **25**, 520 (1982).
- [53] N. Nakajima, C. Z. Cheng, and M. Okamoto, Phys. Fluids B Plasma Phys. **4**, 1115 (1992).
- [54] L. Lin *et al.*, Phys. Plasmas **20** (2013).
- [55] S. P. Hirshman, R. Sanchez, and C. R. Cook, Phys. Plasmas **18**, 062504 (2011).
- [56] L. Lao, H. St. John, R. Stambaugh, A. Kellman, and W. Pfeiffer, Nucl. Fusion **25**, 1611 (1985).
- [57] T. Hayashi, T. Sato, H. J. Gardner, and J. D. Meiss, Phys. Plasmas **2**, 752 (1995).
- [58] A. Reiman and H. Greenside, Comput. Phys. Commun. **43**, 157 (1986).
- [59] S. R. Hudson *et al.*, Phys. Plasmas **19**, 112502 (2012).
- [60] S. P. Hirshman, K. S. Perumalla, V. E. Lynch, and R. Sanchez, J. Comput. Phys. **229**, 6392 (2010).
- [61] S. K. Sudip, K. S. Perumalla, and S. P. Hirshman, Concurr. Comput. Pract. Exp. **25**, 2207 (2013).
- [62] S. E. Sharapov *et al.*, Phys. Plasmas **9**, 2027 (2002).
- [63] K. Appert, R. Gruber, F. Troyon, and J. Vaclavik, Plasma Phys. **24**, 1147 (1982).
- [64] V. Marchenko and S. Reznik, Nucl. Fusion **49**, 022002 (2009).

- [65] R. Betti and J. P. Freidberg, *Phys. Fluids B Plasma Phys.* **4**, 1465 (1992).
- [66] A. Mishchenko *et al.*, *Nucl. Fusion* **54**, 104003 (2014).
- [67] I. Holod, W. L. Zhang, Y. Xiao, and Z. Lin, *Phys. Plasmas* **16** (2009).
- [68] I. Holod and Z. Lin, *Phys. Plasmas* **20** (2013).
- [69] D. A. Spong, *Nucl. Fusion* **53**, 053008(11) (2013).
- [70] E. Strumberger, *Nucl. Fusion* **36**, 891 (1996).